Master's thesis

NTNU
Norwegian University of Science and Technology
Faculty of Natural Sciences
Department of Chemical Engineering

Maria Fanebust

Investigation of coalescence through film drainage modeling in chemical- and bioreactors with non-Newtonian continuous media

Master's thesis in Chemical Engineering and Biotechnology
Supervisor: Hugo Atle Jakobsen
Co-supervisor: Suat Canberk Ozan
June 2021

NTNU
Norwegian University of Science and Technology

Maria Fanebust

Investigation of coalescence through film drainage modeling in chemical- and bioreactors with non-Newtonian continuous media

Master's thesis in Chemical Engineering and Biotechnology
Supervisor: Hugo Atle Jakobsen
Co-supervisor: Suat Canberk Ozan
June 2021

Norwegian University of Science and Technology
Faculty of Natural Sciences
Department of Chemical Engineering

NTNU
Norwegian University of
Science and Technology

Abstract

This thesis considers the drainage of a non-Newtonian film entrapped between two fluid particles to model coalescence in chemical- and bioreactors. In the literature, there exist numerous studies that explore coalescence within Newtonian continuous media. However, coalescence in non-Newtonian media is far less researched and not yet fully understood. Thus, to better understand this concept, a film drainage model taking non-Newtonian continuous media into account is built. The interfaces are deformable and allowed to have any degree of tangential mobility. The non-Newtonian continuous phase is classified as a generalized Newtonian fluid obeying the power law. The fluid particles collide gently with a constant approach velocity. The lubrication theory is employed in the thin-film limit to simplify the model equations, and the tangential velocity of the interfaces is determined via the boundary integral method. Through the power index, n, the effect of the non-Newtonian behavior on the film drainage and coalescence time is examined. The non-Newtonian behavior is found to affect the number of emerging rims on the interfaces significantly. However, when the approach velocity is small in which there are no rims, or when the interfaces are fully mobile, the coalescence time for non-Newtonian and Newtonian continuous media appears to be the same. Otherwise, increasing power index leads to increasing coalescence time. Thus, coalescence takes a longer time for shear-thickening fluids than Newtonian fluids, which again takes longer than shear-thinning fluid coalescence. This non-Newtonian behavior effect is amplified with decreasing tangential mobility of the interfaces and increasing relative approach velocity.

Sammendrag

Denne masteroppgaven tar for seg dreneringen av en ikke-Newtonsk film innfanget mellom to fluidpartikler for å modellere koalesens i kjemiske reaktorer og bioreaktorer. I litteraturen finnes det mange studier som utforsker koalesens i Newtonske kontinuerlige medier. Imidlertid er koalesens i ikke-Newtonske medier langt mindre undersøkt og ennå ikke helt forstått. Dermed, for å bedre forstå dette konseptet, bygges en filmdreneringsmodell som tar ikke-Newtonske kontinuerlige medier i betraktning. Grenseflatene er deformerbare og kan ha hvilken som helst grad av tangential mobilitet. Det ikke-Newtonske fluidet er klassifisert som generalisert Newtonsk og overholder potensloven. Fluidpartiklene kolliderer forsiktig med en konstant tilnærmingshastighet. Hydrodynamisk smøringsteori brukes i tynnfilmgrensen for å forenkle modelligningene, og tangentialhastigheten til grenseflatene bestemmes via grenseintegralmetoden. Gjennom potensindeksen, n, undersøkes effekten av den ikke-Newtonske oppførselen på filmdreneringen og koalesenstiden. Den ikke-Newtonske oppførselen påvirker antall synlige render på grenseflatene betydelig. Imidlertid, når tilnærmingshastigheten er liten og det ikke er noen render på grenseflatene, eller når grenseflatene er helt mobile, ser det ut til at koalesenstiden for ikke-Newtonske og Newtonske kontinuerlige medier er den samme. Ellers fører økende potensindeks til økende koalesenstid. Dermed tar koalesens lengre tid for skjærtykkende fluider enn Newtonske fluider, som igjen tar lengre tid enn skjærtynnende koalesens. Denne ikke-Newtonske effekten forsterkes med avtagende tangentiell mobilitet av grenseflatene og økende relativ tilnærmingshastighet.

Preface

This Master's Thesis concludes the five-year Master's program in Chemical Engineering and Biotechnology at the Norwegian University of Science and Technology. It was written at the Department of Chemical Engineering at the Faculty of Natural Sciences during spring 2021 as an extension of the specialization project carried out in the fall of 2020. The appointed supervisors were Professor Hugo Atle Jakobsen and Ph.D. candidate Suat Canberk Ozan.

First, I would like to express my gratitude to Professor Hugo Atle Jakobsen for allowing me to pursue this topic for my Master's Thesis and providing feedback on my work. Then, I would like to thank Ph.D. candidate Suat Canberk Ozan sincerely for your support, advice, and feedback throughout the work. Your impressive knowledge on the topic and excellent pedagogic skills have allowed me to learn a lot this past year truly. Thank you so much for all your time and patience. Moreover, my thanks also go to fellow master student Hauna Fathmadinda Hosen for great discussions throughout the work, both professional and personal. You have made me smile countless times with your never-ending positivity. Finally, I would like to thank my family and friends for their continuous support and encouragement throughout the years.

List of Figures

Nomenclature

$[A]$	Integration matrix used for the boundary integral equation
$\bar{\tau}_d$	Characteristic scale for particle side tangential stress evaluated at the interface
$\bar{h}$	Characteristic scale for film thickness
$\bar{P}$	Characteristic scale for excess pressure
$\bar{r}$	Characteristic scale for film width
$\bar{t}$	Characteristic time scale
$\bar{v_r}$	Characteristic scale for radial component of the continuous phase velocity
$\bar{v_z}$	Characteristic scale for axial component of the continuous phase velocity
Δt	Time step size
$\dot{\gamma}$	Magnitude of the shear rate tensor
$\dot{\gamma}$	Shear rate tensor
ε	Length scale ratio
η	Non-Newtonian viscosity
η_0	Characteristic measure of non-Newtonian viscosity, (in the Cross model: non-Newtonian viscosity limit at low shear rate)
η_∞	Non-Newtonian viscosity limit at high shear rate
$\hat{U}_t$	Tangential velocity of the interface multiplied by λ^*
λ^*	Dispersed to continuous phase viscosity ratio multiplied with ε
λ_c	Coalescence efficiency
$\mathbf{g}$	gravitational acceleration vector
$\mathbf{n}$	Normal vector
$\mathbf{r_s}$	Surface position vector
$\mathbf{t_1}$	Tangential vector
$\mathbf{t_2}$	Tangential vector
$\mathtt{T}_c$	Continuous phase total stress
$\mathtt{T}_d$	Dispersed phase total stress
μ_c	Newtonian continuous phase viscosity
μ_d	Newtonian dispersed phase viscosity
ϕ	Boundary integral method integrand

ρ	Density of continuous phase, (in the boundary integral method: integral variable in radial axis)
σ	Surface tension
τ_d	Particle side tangential stress evaluated at the interface
$\tau_{\theta r}$	θr-component of the viscous stress in the continuous phase
$\tau_{\theta z}$	θz-component of the viscous stress in the continuous phase
$\tau_{\theta\theta}$	$\theta\theta$-component of the viscous stress in the continuous phase
$\tau_{r\theta}$	$r\theta$-component of the viscous stress in the continuous phase
τ_{rr}	rr-component of the viscous stress in the continuous phase
τ_{rz}	rz-component of the viscous stress in the continuous phase
$\tau_{z\theta}$	$z\theta$-component of the viscous stress in the continuous phase
τ_{zr}	zr-component of the viscous stress in the continuous phase
τ_{zz}	zz-component of the viscous stress in the continuous phase
$\mathbf{v}$	Continuous phase velocity vector
θ	Angular coordinate, (in the boundary integral method: Azimuth angle)
$\tilde{\eta}$	Dimensionless non-Newtonian viscosity
$\tilde{\tau}_d$	Dimensionless particle side tangential stress evaluated at the interface
$\tilde{h}$	Dimensionless film thickness
$\tilde{P}$	Dimensionless excess pressure
$\tilde{r}$	Dimensionless radial distance in the film
$\tilde{t}$	Dimensionless time
$\tilde{U}_t$	Dimensionless tangential velocity of the interface
$\tilde{v}_r$	Dimensionless radial component of the continuous phase velocity
$\tilde{v}_z$	Dimensionless axial component of the continuous phase velocity
$\tilde{V}_{app}$	Dimensionless relative approach velocity of the fluid particles
$\tilde{z}$	Dimensionless axial distance in the film
γ	Shear tensor
τ	Viscous stress tensor
τ_c	Continuous phase viscous stress tensor
A	Matrix which contains weights defined from the thinning, pressure and boundary integral equations , (Hamaker constant with dimension)
$A11$	Matrix block which contains film thickness weights for the thinning equation
$A12$	Matrix block which contains pressure weights for the thinning equation

$A13$ Matrix block which contains tangential velocity weights for the thinning equation

$A21$ Matrix block which contains film thickness weights for the pressure equation

$A22$ Matrix block which contains pressure weights for the pressure equation

$A23$ Matrix block which contains tangential velocity weights for the pressure equation

$A31$ Matrix block which contains film thickness weights for the boundary integral equation

$A32$ Matrix block which contains pressure weights for the boundary integral equation

$A33$ Matrix block which contains tangential velocity weights for the boundary integral equation

A^* Dimensionless Hamaker constant

$C_1, C_2, C_3, C_4, C_5, C_6$ Integration constants

D Derivative matrix

G shear elasticity

H Mean curvature

h Thickness of the thin film

h_0 Minimum initial film thickness

h_{k+1} Film thickness at step $k+1$

h_{k-1} Film thickness at step $k-1$

h_k Film thickness at step k

I Identity matrix

k Time step number

m Flow consistency index

N Number of grid points minus one

n Power index

P Excess pressure in the film

P_c Continuous phase pressure

P_d Dispersed phase pressure

$P_{c,0}$ Continuous phase pressure, perfectly spherical fluid particle

$P_{d,0}$ Dispersed phase pressure, perfectly spherical fluid particle

$P_{ex,c}$ Excess pressure, continuous phase

$P_{ex,d}$ Excess pressure, dispersed phase

P_{k+1} Pressure at step $k+1$

P_k Pressure at step k

r Radial distance in the film

R_1, R_2 Fluid particle radii

r_∞ A large radial distance

R_p Equivalent particle radius

RHS Vector with known values

$RHS1$ Vector with known values for the thinning equation

$RHS2$ Vector with known values for the pressure equation

$RHS3$ Vector with known values for the boundary integral equation

t Time

t_c Coalescence time

$t_{contact}$ Contact time

$t_{drainage}$ Drainage time

U_n Normal velocity of the interface

U_t Tangential velocity of the interface

$U_{t,k+1}$ Tangential velocity at step $k+1$

V_1, V_2 Approach velocities of the particles

v_r radial component of the continuous phase velocity

v_z axial component of the continuous phase velocity

V_{app} Relative approach velocity of the fluid particles

z Axial distance in the film

Contents

1 Introduction

The coalescence of fluid particles plays a vital role within a wide range of industrial fields where dispersed flows regularly occur, such as cosmetics, pharmaceuticals, food, and petrochemical industries. Chemical- and bioreactors are frequently employed in these industries. For dispersed flow in these types of reactors, the continuous phase can often be described as Newtonian, which for instance, applies to water, alcohol, and gasoline. However, non-Newtonian fluids, e.g., soap solutions, polymer solutions, biofluids, or crude oil, are also commonly encountered. These fluids exhibit rheological complexities, i.e., complex flow characteristics, possibly affecting the interaction between the fluid particles and mass and heat transfer in a reactor, thereby influencing the coalescence process and the efficiency and performance of the reactor significantly. However, the detailed influence of the complex flow properties of fluids on coalescence is not yet fully understood. Hence, to gain insight into this aspect, the single event of coalescence between two fluid particles in a non-Newtonian medium will be investigated. However, this first requires an understanding of the field of rheology.

1.1 Rheology

Rheology is a branch of physics that deals with the deformation and flow of materials (Schowalter 1978). The term originates from the Greek words *rheo* meaning "flow" and *logia*, which translates to "study of." Professor E.C. Bingham of Lafayette College in Indiana formally introduced the term rheology in 1929, which coincided with the formation of the American Society of Rheology (Doraiswamy 2002). The main objective in rheology is to establish constitutive relations between stimuli applied on a material and the materials' responses to stimuli. These relations are commonly employed within industries such as food, polymer, and pharmaceutical. Throughout the 20^{th} century, these industries have grown exponentially, which has increased the popularity of the rheology field considerably.

Strictly speaking, rheology is concerned with describing the flow behaviors of all types of matters. However, rheologists are mainly interested in deformable materials (unlike perfectly rigid solids as studied in Newton's Principia) that exhibit some degree of resistance to deformation (unlike ideal fluids investigated by Blaise Pascal). Consequently, the two extrema of the scope of the rheology field are generally accepted as Newtonian fluids and Hooke's elastic solids. In the 17^{th} century, the British physicist Robert Hooke developed the concept of perfect elasticity and what is known as "Hooke's law of elasticity." He stated that "the power of any spring is in the same proportion with the tension thereof", which implies a constant proportional relation between the applied force (the stress) and the deformation (the shear). "Hookes law of elasticity" can then be expressed as:

$$\tau = G\gamma, \tag{1}$$

Here, τ is the viscous stress, γ the shear, and G a material-specific proportionality constant called shear elasticity. On the other end of the spectrum, the Newtonian fluids show resistance to deformation, which is "proportional to the velocity which the parts of the liquid are separated from one another" caused by the "lack of slipperiness of the parts of the liquids", as stated in Newton's own words in Principia. From these statements, "Newton's law of viscosity" arose, in which the shear stress and the shear rate are proportionally related through the material-specific constant, viscosity. This law can be written as:

$$\tau = \eta\dot{\gamma} \tag{2}$$

where η is the viscosity and $\dot{\gamma}$ is the shear rate. Newtonian fluids can further be described by a viscosity that is independent of the shear rate. No real fluids fit this definition perfectly, but common fluids like water are often assumed Newtonian to simplify calculations. Most fluids do not follow Newton's law of viscosity, as their viscosity is dependent on the shear rate. These fluids are non-Newtonian and can roughly be categorized as either viscoelastic fluids or generalized Newtonian fluids. The viscoelastic fluids show both elastic and viscous characteristics under deformation and are considered between Newtonian and Hookean matters. On the other hand, generalized Newtonian fluids are only viscous and exhibit no elastic properties. The following constitutive relation can describe this type of fluids:

$$\tau = \eta(\dot{\gamma})\dot{\gamma} \tag{3}$$

where $\dot{\gamma}$ is the magnitude of the shear rate. The non-Newtonian viscosity, $\eta(\dot{\gamma})$ is most commonly estimated by the power law proposed by Ostwald (1925) and de Waele (1923). This model is defined by:

$$\eta(\dot{\gamma}) = m|\dot{\gamma}|^{n-1}, \tag{4}$$

in which m is the flow consistency index, and n is the power index, which both need to be determined experimentally for each fluid. When $n = 1$, the model reduces to fit Newton's law of viscosity. For values of n below 1, the viscosity decreases with increasing shear rate, resulting in the name shear-thinning fluids. In contrast, $n > 1$ yields increasing viscosity with increasing shear rate, and fluids with this property are called shear-thickening. Shear-thinning is the most common type of non-Newtonian behavior in industrial applications, which frequently is observed for dispersions, emulsions, suspensions, and polymer solutions often found in bioreactors. Shear-thickening behavior is far less encountered but may occur in some dispersions and particular suspensions with a high solid particle concentration. For the most part, shear-thickening is an unwanted effect that can cause significant processing issues, but these fluids have some practical applications, such as shock absorbers (Worldwide 2016).

The power law model is the simplest way to estimate the non-Newtonian viscosity and successfully does so for moderate shear rates. However, the viscosity becomes almost constant for low and high shear rates, and the power law model fails to give accurate results. Then more complex models, e.g., the Sisko model, which applies for shear rates in the power law region in addition to higher shear rates, would be a better choice to estimate the viscosity. The Sisko model is defined as (Barnes 2000):

$$\eta = m|\dot{\gamma}|^{1-n} + \eta_\infty|\dot{\gamma}| \tag{5}$$

where η_∞ is the viscosity value at high shear rate. For the entire range of shear rates, the Cross model (Barnes 2000),

$$\frac{\eta - \eta_\infty}{\eta_0 - \eta_\infty} = \frac{1}{1 + m|\dot{\gamma}|^{1-n}} \tag{6}$$

can be employed. Here, η_0 is the viscosity at a low shear rate. However, in this thesis, the shear rates are assumed to be within the range describable by the power law.

1.2 Coalescence

Having examined rheology, it is now necessary to investigate coalescence. A popular coalescence modeling approach is film drainage modeling. Based on the observations of Shinnar & Church (1960), the following steps are suggested:

1. The external flow brings the fluid particles into contact
2. A thin film of the continuous medium is trapped between the particles.
3. The thin film drains until it reaches the value of critical film thickness
4. The film ruptures, and coalescence occurs.

Note that it is required that the particles are in contact for a longer time than the time necessary to drain the film until the critical thickness for coalescence to occur. Once the critical thickness is reached, the film ruptures very quickly, and there is no other option than coalescence. Even though the steps given above are proposed based on observations in systems with Newtonian fluids, it is assumed that they also apply in the same manner when the continuous medium is non-Newtonian.

Coulaloglou (1975) suggested the following statistical formula for estimating the coalescence efficiencey, i.e., the fraction of collisions between the fluid particles that result in coalescence:

$$\lambda_c = exp\left(-\frac{t_{drainage}}{t_{contact}}\right) \tag{7}$$

In this model, the particles are assumed to collide "gently," such that the emerging thin film's radius is much smaller than the particles' radii. Then, the drainage time can be estimated by the use of hydrodynamic modeling of the film drainage. A significant number of film drainage models with varying levels of complexity exist for Newtonian systems in the literature. Chesters (1991) and Liao & Lucas (2010) provide a thorough overview of these models. Due to the film between the fluid particles being relatively thin, the lubrication theory is frequently employed to reduce the complexity of the film drainage models. The simplest drainage models can be solved analytically, but that necessitates entirely rigid spherical fluid particles with no tangential mobility. If the interfaces of the particles are allowed to deform, the experimentally observed dimple formation (Derjaguin & Kussakov 1939) can be modeled. These film drainage models can be classified based on the tangential mobility of the interfaces, which can be considered either immobile, partially mobile, or fully mobile. Immobile interfaces correspond to zero tangential velocity of the interfaces, in which the viscous forces govern the drainage within the film, which yields a parabolic velocity profile. This immobilization of the interfaces may occur as a result of very high dispersed phase viscosity (Bazhlekov et al. 2000) or interfacial tension gradients emerging due to the presence of surfactants, which form Marangoni stresses at the interface and also permits the interface to have viscoelastic or viscous characteristics (Ozan & Jakobsen 2019*b*). When the tangential velocity of the interfaces dominates the film drainage entirely, the velocity profile appears as a plug-flow profile, and the interfaces are regarded as fully mobile. The parabolic component of the velocity profile is negligible in this instance. When both the parabolic and plug-flow components are of significance, the interfaces are partially mobile. The immobilizing factors, i.e., the presence of surfactants and the high dispersed phase viscosity, play a crucial role in estimating the degree of tangential mobility.

Determining the tangential velocity of the interfaces requires the coupling of the dispersed and continuous phase velocity fields. By employing the boundary integral method (Davis et al. 1989), this

coupling can be accomplished through the no-slip condition and the stress balances, without needing the solution of the particles' internal flow. Consequently, the computation costs are significantly reduced. In the literature, the use of this method is well-established. It has been employed in many film drainage studies with Newtonian fluids and mobile interfaces (Yiantsios & Davis 1991, Abid & Chesters 1994, Klaseboer et al. 2000, Bazhlekov et al. 2000, Ozan & Jakobsen 2019*a*, Ozan et al. 2021). Yiantsios & Davis (1991) examined the interaction between two fluid particles with deformable interfaces and revealed that in finite time, coalescence is impossible without attractive van der Waals forces. Also, they found that film rupture occurs by the center of the fluid particles when the van der Waals forces are strong, which they labeled as nose rupture. For weaker van der Waals forces, the capillary forces cause rim formation at the interfaces. The rupture then occurs at the rim instead, i.e., rim rupture. Abid & Chesters (1994) studied the centerline collision of two droplets approaching each other with a constant relative approach velocity in the presence of attractive van der Waals forces. They considered the interfaces to be fully mobile and estimated the critical film thickness as a function of the Hamaker constant. Klaseboer et al. (2000) then examined the film drainage by comparing experimental results with two theoretical models, where the interfaces were considered either fully mobile or immobile. They found that the model with immobile interfaces fits their experimental results best and augured that this might be caused by small amounts of surfactants in the system being responsible for the immobilization of the interfaces. Bazhlekov et al. (2000) built a film drainage model where both the plug flow and parabolic velocity profile contributions were taken into account. The mobility appears in the thinning equation through the dispersed to continuous phase viscosity ratio in their model. Furthermore, they considered either collision of two fluid particles with constant interaction force or constant approach velocity. However, the model does not take the attractive van der Waals forces into account. Ozan & Jakobsen (2019*a*) employ a similar model, in which the coalescence time is estimated as a function of the dispersed to continuous phase viscosity ratio and the relative approach velocity. However, in contrast to Bazhlekov et al. (2000), Ozan & Jakobsen (2019*a*) include the attractive van der Waals forces in their model. For varying approach velocities, they identified three successive film drainage regimes. In the first regime, which is detected for lower approach velocities, the film rupture occurs at the fluid particles' center, and the coalescence time decreases with increasing approach velocity. Eventually, increasing the approach velocity results in the transition to the second drainage regime where dimple formation is observed and the film ruptures at the rim. In this regime, the coalescence time still decreases with increasing approach velocity, but less and less prominently until a minimum is reached. After this point, the coalescence time starts to increase as the approach velocity is increased. Simultaneously, secondary rim structures start to form at the interface, and the last drainage regime is entered. In a more recent study, Ozan et al. (2021) added a force balance to their film drainage model, which allowed the approach velocity to vary with time. Also, due to the added force balance, the particles are allowed to bounce off each other. The force balance includes the buoyancy, the drag, and the added mass forces, in addition to the film's resistance to the drainage. Ozan et al. (2021) revealed that this resistance could slow down the approach velocity significantly and even cause rebounding, i.e., bouncing of the fluid particles instead of coalescence.

In contrast, there are far fewer studies in the literature dedicated to coalescence in non-Newtonian continuous media. Furthermore, most of these studies focus on the varying factors influencing the in-line coalescence of rising bubbles. The experimental observations of Acharya & Ulbrecht (1978) revealed that elasticity of the continuous phase tends to prevent film drainage and thus slow down coalescence. Dekee et al. (1986) conducted experiments in which they examined the impacts of the approach velocity and the bubble wake on the coalescence features within a vertical arrangement with purely shear-thinning and viscoelastic polymer solutions. In several studies, Li and coworkers (Li et al. 1997, Li 1999, Li et al. 2001) focused on the interactions and coalescence between bubbles

rising in non-Newtonian media. They found that the stress created by the passage of bubbles and their relaxation caused by the memory of the fluid are key factors influencing the bubble interactions and coalescence. Lin & Lin (2009) revealed that the acceleration of a trailing bubble to the leading one is caused by the pushing and drag forces. Al-Matroushi & Borhan (2009) reported that the flow disturbances behind the leading bubble and the viscoelastic proprieties of the continuous phase might prevent coalescence. Sun et al. (2017) examined the effects of the bubble size, generation frequency, and liquid property on the minimum in-line bubble coalescence height in carboxymethyl cellulose (CMC) solutions described by the power law. Zhu et al. (2018) looked into the velocity evolution in the in-line coalescence process of two rising bubbles in non-Newtonian fluids through experimental work and also established a theoretical model based on Newton's second law. Even though these studies provide many insights into the overall coalescence nature in columns, they do not precisely control crucial parameters, e.g., the approach velocity. Thus, it is almost impossible to isolate these parameters' effects from others. Studies considering the coalescence of fluid particles growing side-by-side, i.e., parallel coalescence, permit the approach velocity to be precisely controlled. Then, the role of the approach velocity and other parameters such as the rheological characteristics on the coalescence behavior can be examined without the interference of changes and fluctuations in the velocity. To date, there are far fewer studies investigating parallel coalescence in non-Newtonian fluids compared to in-line. However, there exists some experimental work, e.g., Fan et al. (2020), which examined the coalescence dynamics of twin bubbles growing alongside two adjacent nozzles in CMC solutions with varying concentrations. Their experimental setup allowed small bubble pairs to be produced periodically at a given gas volume flow rate controlled accurately by a syringe pump. Fan et al. (2020) found that the coalescence efficiency increases with the CMC concentration. Note that CMC becomes more shear-thinning as the concentration increases (Benchabane & Bekkour 2008).

The specific objective of this thesis is to explore the film drainage behavior and the coalescence time for fluid particles in non-Newtonian continuous media by employing a hydrodynamic film drainage model. During the drainage, the interfaces are allowed to deform and have any degree of tangential mobility. In addition, the non-Newtonian film is described by the power law.

This thesis begins by presenting the physical system and deriving the mathematical models in Section 2. Then the numerical procedure is given in Section 3 and the results in Section 4. Finally, the conclusions are summarized in Section 5.

2 Theory

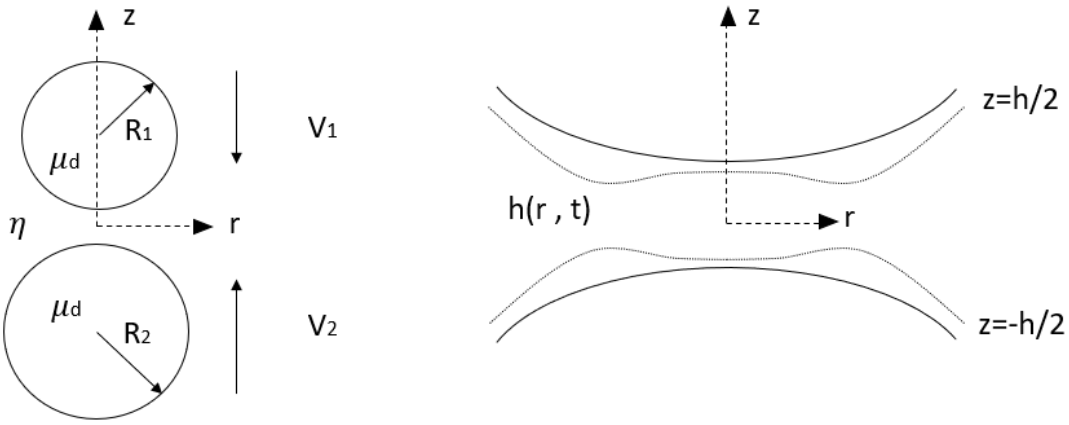

Figure 1: Physical system

The axisymmetrical interactions between two fluid particles in non-Newtonian continuous media are investigated. Figure 1 illustrates the physical configuration in which the particles, which can be either bubbles or droplets, approach each other along their center lines with constant relative approach velocity, $V_{app} = V_2 - V_1$. Here, the particles radii, R_1 and R_2 are allowed to be different. A thin film of the non-Newtonian continuous phase entraps in between the particles, and the viscosity of this phase, η, follows the power law model. The thin film has a thickness h, which is a function of the radial position, r, and the time, t. Eventually, the film starts to drain, and upon reaching a critical thickness, coalescence occurs. In the film, the flow is assumed to be incompressible, the interfaces between the continuous and the dispersed phases are deformable, and the surface tension, σ, is constant. Moreover, the particles are assumed to collide gently, which means that particles' radii are much larger than the radius of the entrapped film. As a result, both particles can be described by the equivalent radius , R_p (Abid & Chesters 1994):

$$\frac{1}{R_p} = \frac{1}{2}\left(\frac{1}{R_1} + \frac{1}{R_2}\right), \tag{8}$$

Note that the derivation of the equivalent radius is given in App. C.1. The collision between unequal-sized particles can now be modeled as the collision of equal-sized particles with a radius R_p. Thus, the system is symmetric around the radial axis in addition to axisymmetric. Hence, it is sufficient only to obtain the solution for one of the four quadrants of the film shown in Fig. 1. Here, the quadrant where $r \geq 0$ and $z \geq 0$, and the interface position is given by $z = h/2$, is chosen.

First, a film drainage model will be derived on the same form as the one employed by Ozan & Jakobsen (2019*a*), which holds for a Newtonian continuous phase. Then, the model will be expanded by including a non-constant viscosity following the power law to account for the non-Newtonian continuous phase.

2.1 Newtonian model

Governing equations, which are valid anywhere in the system, are derived for the bulk phases. These equations show how mass and momentum are conserved throughout the bulk phases. In addition, conditions valid at the interface will be employed as boundary conditions. These conditions relate the variables of the two bulk phases.

2.1.1 Governing equations

The continuity equation and the equation of motion governs the thin film, where the former is defined by:

$$\frac{\partial \rho}{\partial t} + \nabla \cdot (\rho \mathbf{v}) = 0. \tag{9}$$

Here, ρ is density of the continuous phase, t is time and $\mathbf{v}$ is the continuous phase velocity vector. Under the assumption of incompressible flow, the continuity equation simplifies to:

$$\nabla \cdot \mathbf{v} = 0. \tag{10}$$

By applying the definition of the nabla operator (see Eq. A.8 in Appendix A), decomposing the velocity vector in cylindrical coordinates (see Eq. A.9) and also applying the assumption of axisymmetry, the continuity equation can be written as:

$$\left(\mathbf{e}_r \frac{\partial}{\partial r} + \frac{1}{r} \mathbf{e}_\theta \frac{\partial}{\partial \theta} + \mathbf{e}_z \frac{\partial}{\partial z} \right) \cdot (v_r \mathbf{e}_r + v_z \mathbf{e_z}) = 0 \tag{11}$$

Note that assuming axisymmetry results in constant velocity in the θ-direction, and in this work, $v_\theta = 0$ is assumed.

Furthermore, by employing the definition of the dot product between cylindrical unit base vectors (see Eqs. A.1 and A.2), the product rule (see Eq. A.15), and the definition of derivatives of cylindrical unit base vectors (see Eqs A.7), the continuity equation is reduced to:

$$\frac{1}{r} \frac{\partial}{\partial r} (r v_r) + \frac{\partial v_z}{\partial z} = 0 \tag{12}$$

The equation of motion is given by:

$$\frac{\partial}{\partial t} (\rho \mathbf{v}) + \nabla \cdot (\rho \mathbf{v} \mathbf{v}) = -\nabla P - \nabla \cdot \tau + \rho \mathbf{g}. \tag{13}$$

Here, P is pressure, τ is the viscous stress tensor and $\mathbf{g}$ is the gravitational acceleration vector. As with the continuity equation, the assumption of incompressible flow can be employed and the velocity vector can be written in terms of cylindrical unit base vectors. The first term of the equation of motion is therefore expressed as:

$$\frac{\partial}{\partial t} (\rho \mathbf{v}) = \rho \frac{\partial}{\partial t} (v_r \mathbf{e}_r + v_z \mathbf{e_z}) \tag{14}$$

Moreover, the definition of the nabla vector and the dyadic velocity product (see Eq. A.11) can be applied to express the second term in the equation of motion as:

$$\nabla \cdot (\rho \mathbf{v}\mathbf{v}) = \left(\mathbf{e}_r \frac{\partial}{\partial r} + \frac{1}{r} \mathbf{e}_\theta \frac{\partial}{\partial \theta} + \mathbf{e}_z \frac{\partial}{\partial z} \right) \cdot \rho (v_r v_r \mathbf{e}_r \mathbf{e}_r + v_r v_z \mathbf{e}_r \mathbf{e}_z + v_z v_r \mathbf{e}_z \mathbf{e}_r + v_z v_z \mathbf{e}_z \mathbf{e}_z) \tag{15}$$

Notice that Eq. A.11 is simplified due to the assumption: $v_\theta = 0$.

By use of the definition of the dot product between cylindrical unit base vectors and the definitions of unit base vector derivatives, Eq. 15 can be reformulated as:

$$\nabla \cdot (\rho \mathbf{v}\mathbf{v}) = \rho \left[\frac{\partial}{\partial r}(v_r v_r \mathbf{e}_r) + \frac{\partial}{\partial r}(v_r v_z \mathbf{e}_z) + \frac{v_r v_r}{r} \mathbf{e}_r + \frac{v_r v_z}{r} \mathbf{e}_z + \frac{\partial}{\partial z}(v_z v_r \mathbf{e}_r) + \frac{\partial}{\partial z}(v_z v_z \mathbf{e}_z) \right] \tag{16}$$

Equation 16 is further manipulated by applying the product rule and the definition of derivatives of unit base vectors, which results in:

$$\nabla \cdot (\rho \mathbf{v}\mathbf{v}) = \rho \left[\mathbf{e}_r \frac{\partial}{\partial r}(v_r v_r) + \mathbf{e}_z \frac{\partial}{\partial r}(v_r v_z) + \mathbf{e}_r \frac{v_r v_r}{r} + \mathbf{e}_z \frac{v_r v_z}{r} + \mathbf{e}_r \frac{\partial}{\partial z}(v_z v_r) + \mathbf{e}_z \frac{\partial}{\partial z}(v_z v_z) \right] \tag{17}$$

The third term in the equation of motion, the pressure gradient, can be expressed as:

$$-\nabla P = -\mathbf{e}_r \frac{\partial P}{\partial r} - \mathbf{e}_z \frac{\partial P}{\partial z} \tag{18}$$

Notice that the angular pressure gradient term is neglected due to the assumption of axisymmetric flow. This assumptions also affects the stress tensor, τ (Eq. A.13 shows how a tensor is expressed in cylindrical coordinates), in the fourth term of the equation of motion, which can be expressed as:

$$\nabla \cdot \tau = \left(\mathbf{e}_r \frac{\partial}{\partial r} + \frac{1}{r} \mathbf{e}_\theta \frac{\partial}{\partial \theta} + \mathbf{e}_z \frac{\partial}{\partial z} \right) \cdot (\tau_{rr} \mathbf{e}_r \mathbf{e}_r + \tau_{rz} \mathbf{e}_r \mathbf{e}_z + \tau_{\theta\theta} \mathbf{e}_\theta \mathbf{e}_\theta \mathbf{e}_\theta + \tau_{zr} \mathbf{e}_z \mathbf{e}_r + \tau_{zz} \mathbf{e}_z \mathbf{e}_z) \tag{19}$$

Note that due to the assumption of axisymmetry which leads to $\frac{\partial v_r}{\partial \theta} = 0$ and $\frac{\partial v_z}{\partial \theta} = 0$, in addition to the assumption of $v_\theta = 0$, the terms that include : $\tau_{r\theta}$, $\tau_{\theta r}$, $\tau_{\theta z}$ and $\tau_{z\theta}$ vanishes (see Eq. A.14). However, the $\tau_{\theta\theta}$-component is not neglected directly because it has contributions from the radial component of the velocity.

Furthermore, by performing the dot product, applying the product rule and the unit base vector derivatives given in Eq. A.7, the stress tensor term can be rearranged to:

$$\nabla \cdot \tau = \frac{\partial}{\partial r}(\tau_{rr} \mathbf{e}_r) + \frac{\partial}{\partial r}(\tau_{rz} \mathbf{e}_z) + \frac{\tau_{rr}}{r} \mathbf{e}_r - \frac{\tau_{\theta\theta}}{r} \mathbf{e}_r + \frac{\partial}{\partial z}(\tau_{zr} \mathbf{e}_r) + \frac{\partial}{\partial z}(\tau_{zz} \mathbf{e}_z) \tag{20}$$

Equation 20 is manipulated by further use of the product rule and the definition of derivatives of unit base vectors given in the appendix, which results in:

$$\nabla \cdot \tau = \mathbf{e}_r \frac{\partial \tau_{rr}}{\partial r} + \mathbf{e}_z \frac{\partial \tau_{rz}}{\partial r} + \mathbf{e}_r \frac{\tau_{rr}}{r} - \mathbf{e}_r \frac{\tau_{\theta\theta}}{r} + \mathbf{e}_r \frac{\partial \tau_{zr}}{\partial z} + \mathbf{e}_z \frac{\partial \tau_{zz}}{\partial z} \tag{21}$$

The final term in the equation of motion, the gravitation term, is assumed to be negligible compared to the other terms (See App. C.2 for further reasoning).

The equation of motion can now be expressed as:

$$\begin{aligned}&\rho\left[\frac{\partial}{\partial t}(v_r\mathbf{e}_r+v_z\mathbf{e}_z)+\mathbf{e}_r\frac{\partial}{\partial r}(v_rv_r)+\mathbf{e}_z\frac{\partial}{\partial r}(v_rv_z)+\mathbf{e}_r\frac{v_rv_r}{r}+\mathbf{e}_z\frac{v_rv_z}{r}+\mathbf{e}_r\frac{\partial}{\partial z}(v_zv_r)+\mathbf{e}_z\frac{\partial}{\partial z}(v_zv_z)\right]\\&=-\mathbf{e}_r\frac{\partial P}{\partial r}-\mathbf{e}_z\frac{\partial P}{\partial z}-\mathbf{e}_r\frac{\partial\tau_{rr}}{\partial r}-\mathbf{e}_z\frac{\partial\tau_{rz}}{\partial r}-\mathbf{e}_r\frac{\tau_{rr}}{r}+\mathbf{e}_r\frac{\tau_{\theta\theta}}{r}-\mathbf{e}_r\frac{\partial\tau_{zr}}{\partial z}-\mathbf{e}_z\frac{\partial\tau_{zz}}{\partial z}\end{aligned}\tag{22}$$

Thus, the r-component of the equation of motion read:

$$\rho\left[\frac{\partial v_r}{\partial t}+\frac{\partial}{\partial r}(v_rv_r)+\frac{v_rv_r}{r}+\frac{\partial}{\partial z}(v_zv_r)\right]=-\frac{\partial P}{\partial r}-\frac{\partial\tau_{rr}}{\partial r}-\frac{\tau_{rr}}{r}+\frac{\tau_{\theta\theta}}{r}-\frac{\partial\tau_{zr}}{\partial z}\tag{23}$$

By employing the product rule, Eq. 23 can be rearranged to:

$$\rho\left[\frac{\partial v_r}{\partial t}+\frac{1}{r}\frac{\partial}{\partial r}(rv_rv_r)+\frac{\partial}{\partial z}(v_zv_r)\right]=-\frac{\partial P}{\partial r}-\frac{1}{r}\frac{\partial}{\partial r}(r\tau_{rr})+\frac{\tau_{\theta\theta}}{r}-\frac{\partial\tau_{zr}}{\partial z}\tag{24}$$

Furthermore, the z-component of the equation of motion can be written as:

$$\rho\left[\frac{\partial v_z}{\partial t}+\frac{\partial}{\partial r}(v_rv_z)+\frac{v_rv_z}{r}+\frac{\partial}{\partial z}(v_zv_z)\right]=-\frac{\partial P}{\partial z}-\frac{\partial\tau_{rz}}{\partial r}-\frac{\partial\tau_{zz}}{\partial z}\tag{25}$$

As with the radial component, the product rule is applied to write Eq. 25 on the form:

$$\rho\left[\frac{\partial v_z}{\partial t}+\frac{1}{r}\frac{\partial}{\partial r}(rv_rv_z)+\frac{\partial}{\partial z}(v_zv_z)\right]=-\frac{\partial P}{\partial z}-\frac{\partial\tau_{rz}}{\partial r}-\frac{\partial\tau_{zz}}{\partial z}\tag{26}$$

For Newtonian fluids, the components of the viscous stress tensor is defined by:

$$\tau_{rr}=-2\mu_c\frac{\partial v_r}{\partial r},\tag{27}$$

$$\tau_{rz}=\tau_{zr}=-\mu_c\left(\frac{\partial v_z}{\partial r}+\frac{\partial v_r}{\partial z}\right),\tag{28}$$

$$\tau_{\theta\theta}=-2\mu_c\frac{v_r}{r},\tag{29}$$

$$\tau_{zz}=-2\mu_c\frac{\partial v_z}{\partial z},\tag{30}$$

where μ_c is the Newtonian continuous phase viscosity. Introducing Eqs. 27 - 30 into Eq. 24 and 26, yields the following expressions for the r and z components of the equation of motion, respectively:

$$\rho\left[\frac{\partial v_r}{\partial t}+\frac{1}{r}\frac{\partial}{\partial r}(rv_rv_r)+\frac{\partial}{\partial z}(v_zv_r)\right]=-\frac{\partial P}{\partial r}+\frac{1}{r}\frac{\partial}{\partial r}\left(2\mu_c r\frac{\partial v_r}{\partial r}\right)-2\mu_c\frac{v_r}{r^2}+\frac{\partial}{\partial z}\left[\mu_c\left(\frac{\partial v_z}{\partial r}+\frac{\partial v_r}{\partial z}\right)\right] \tag{31}$$

$$\rho\left[\frac{\partial v_z}{\partial t}+\frac{1}{r}\frac{\partial}{\partial r}(rv_rv_z)+\frac{\partial}{\partial z}(v_zv_z)\right]=-\frac{\partial P}{\partial z}+\frac{\partial}{\partial r}\left[\mu_c\left(\frac{\partial v_z}{\partial r}+\frac{\partial v_r}{\partial z}\right)\right]+\frac{\partial}{\partial z}\left(2\mu_c\frac{\partial v_z}{\partial z}\right) \tag{32}$$

2.1.2 Interface conditions

The flows in the continuous and dispersed phases are coupled via a set of boundary conditions valid at the interface: the no-slip condition, the kinematic condition, and the normal and the tangential components of the stress balance. In order to express these conditions explicitly, the unit tangent and normal vectors on the interface must be determined first.

The position vector, $\mathbf{r}$ is defined by:

$$\mathbf{r}=r\mathbf{e}_r(\theta)+z\mathbf{e}_z \tag{33}$$

As the solution only will be recovered for, $r\geq 0$ and $z\geq 0$, the interface position is given by:

$$z=\frac{1}{2}h(r,t) \tag{34}$$

Thus, the position at the interfaces, the surface position vector, $\mathbf{r}_s$, becomes:

$$\mathbf{r}_s=r\mathbf{e}_r(\theta)+\frac{1}{2}h(r,t)\mathbf{e}_z \tag{35}$$

The tangential vector, $\mathbf{t}_1$, is defined by:

$$\mathbf{t}_1=\frac{\frac{\partial \mathbf{r_s}}{\partial r}}{|\frac{\partial \mathbf{r_s}}{\partial r}|} \tag{36}$$

By use of the product rule in addition to the relations for derivatives of the unit base vectors (Eq. A.7), the derivative of the surface position vector with respect to r can be expressed as:

$$\frac{\partial \mathbf{r_s}}{\partial r}=\mathbf{e}_r+\frac{1}{2}\frac{\partial h}{\partial r}\mathbf{e}_z \tag{37}$$

The length of this vector is calculated as:

$$\left|\frac{\partial \mathbf{r_s}}{\partial r}\right|=\sqrt{\left(\mathbf{e}_r+\frac{1}{2}\frac{\partial h}{\partial r}\mathbf{e}_z\right)\cdot\left(\mathbf{e}_r+\frac{1}{2}\frac{\partial h}{\partial r}\mathbf{e}_z\right)} \tag{38}$$

Taking the dot product 38 yields:

$$\left|\frac{\partial \mathbf{r_s}}{\partial r}\right| = \sqrt{1+\frac{1}{4}\left(\frac{\partial h}{\partial r}\right)^2} \tag{39}$$

The tangential vector, $\mathbf{t}_1$ can then be expressed as:

$$\mathbf{t}_1 = \frac{\mathbf{e}_r + \frac{1}{2}\frac{\partial h}{\partial r}\mathbf{e}_z}{\sqrt{1+\frac{1}{4}\left(\frac{\partial h}{\partial r}\right)^2}} \tag{40}$$

Furthermore, the tangential vector, $\mathbf{t}_2$ is defined by:

$$\mathbf{t}_2 = \frac{\frac{\partial \mathbf{r_s}}{\partial \theta}}{|\frac{\partial \mathbf{r_s}}{\partial \theta}|} \tag{41}$$

Taking the derivative of the surface position vector with respect to the angular direction gives:

$$\frac{\partial \mathbf{r_s}}{\partial \theta} = r\frac{\partial \mathbf{e}_r}{\partial \theta} = r\mathbf{e}_\theta \tag{42}$$

The length of this vector then becomes:

$$\left|\frac{\partial \mathbf{r_s}}{\partial \theta}\right| = \sqrt{(r\mathbf{e}_\theta)\cdot(r\mathbf{e}_\theta)} = r \tag{43}$$

Thus, the tangential vector, $\mathbf{t}_2$, can be expressed as:

$$\mathbf{t}_2 = \frac{r\mathbf{e}_\theta}{r} = \mathbf{e}_\theta \tag{44}$$

Moreover, the normal vector, $\mathbf{n}$, is defined by:

$$\mathbf{n} = \mathbf{t}_1 \times \mathbf{t}_2 \tag{45}$$

Inserting the obtained expressions for $\mathbf{t}_1$ and $\mathbf{t}_2$ in Eqs. 40 and 44 into Eq. 45, and calculating the cross product yields:

$$\mathbf{n} = \frac{\mathbf{e}_r + \frac{1}{2}\frac{\partial h}{\partial r}\mathbf{e}_z}{\sqrt{1+\frac{1}{4}\left(\frac{\partial h}{\partial r}\right)^2}} \times \mathbf{e}_\theta = \frac{\mathbf{e}_z - \frac{1}{2}\frac{\partial h}{\partial r}\mathbf{e}_r}{\sqrt{1+\frac{1}{4}\left(\frac{\partial h}{\partial r}\right)^2}} \tag{46}$$

Note that the definition of the cross product of unit base vectors is given in Eq. A.4.

The initial conditions can now be derived. The no-slip condition is defined by:

$$\mathbf{v}\cdot\mathbf{t}_1 = U_t, \tag{47}$$

in which U_t is the tangential velocity of the interface.

Inserting the velocity vector decomposed in cylindrical coordinates (Eq. A.10) and the derived tangential vector from Eq. 40 into Eq. 47 results in:

$$(v_r\mathbf{e}_r + v_z\mathbf{e}_z)\cdot\frac{\mathbf{e}_r + \frac{1}{2}\frac{\partial h}{\partial r}\mathbf{e}_z}{\sqrt{1+\frac{1}{4}\left(\frac{\partial h}{\partial r}\right)^2}} = U_t. \tag{48}$$

Then, by taking dot product, Eq. 48 becomes:

$$\frac{v_r + \frac{1}{2}\frac{\partial h}{\partial r}v_z}{\sqrt{1+\frac{1}{4}\left(\frac{\partial h}{\partial r}\right)^2}} = U_t, \tag{49}$$

Bear in mind that the velocities v_r and v_z should be evaluated at the interface.

The kinematic condition is defined as:

$$\mathbf{v}\cdot\mathbf{n} = U_n. \tag{50}$$

where U_n is the normal velocity of the interface, which can be written in the kinematic condition as (Johns & Narayanan 2007):

$$\mathbf{v}\cdot\mathbf{n} = \frac{1}{2}\frac{\partial h}{\partial t}, \tag{51}$$

This condition appears due to mass balance across the interface, which shows continuity between the normal speed of the interface and the normal component of the film velocity. The name is connected to the definition of kinematics which is a branch of mechanics that describes the motion of points, bodies, and systems of bodies without considering the forces that cause them to move (Whittaker 1904).

By use of the decomposed velocity vector (Eq. A.10) and the derived normal vector in Eq. 46, the kinematic condition can be expressed as:

$$(v_r\mathbf{e}_r + v_z\mathbf{e}_z)\cdot\frac{\mathbf{e}_z - \frac{1}{2}\frac{\partial h}{\partial r}\mathbf{e}_r}{\sqrt{1+\frac{1}{4}\left(\frac{\partial h}{\partial r}\right)^2}} = \frac{1}{2}\frac{\partial h}{\partial t} \tag{52}$$

After employing the definition of the unit base vector dot product, Eq. 52 becomes:

$$\frac{v_z - \frac{1}{2}\frac{\partial h}{\partial r}v_r}{\sqrt{1+\frac{1}{4}\left(\frac{\partial h}{\partial r}\right)^2}} = \frac{1}{2}\frac{\partial h}{\partial t} \tag{53}$$

As for the no-slip condition, here, the velocities are evaluated at the interface.

A stress balance over the interface can be formulated as:

$$(\mathtt{T}_c \cdot \mathbf{n}) - (\mathtt{T}_d \cdot \mathbf{n}) = 2H\sigma\mathbf{n}, \tag{54}$$

where $\mathtt{T}_c$ and $\mathtt{T}_d$ are the total stress tensors in the continuous and dispersed phases, respectively. Moreover, H is the mean curvature, and σ is the surface tension. Normal and tangential components of the stress balance can further be expressed as:

$$(\mathtt{T}_c : \mathbf{nn}) - (\mathtt{T}_d : \mathbf{nn}) = 2H\sigma(\mathbf{n} \cdot \mathbf{n}), \tag{55}$$

and

$$(\mathtt{T}_c : \mathbf{nt}_1) - (\mathtt{T}_d : \mathbf{nt}_1) = 2H\sigma(\mathbf{n} \cdot \mathbf{t_1}) \tag{56}$$

Here, $\mathtt{T}_c$ is given by:

$$\mathtt{T}_c = -P_c(\mathbf{e}_r\mathbf{e}_r + \mathbf{e}_\theta\mathbf{e}_\theta + \mathbf{e}_z\mathbf{e}_z) + \tau_c \tag{57}$$

Moreover, the viscous stress tensor for Newtonian fluid is defined by:

$$\tau_c = -\mu_c\dot{\gamma} = -\mu_c[\nabla\mathbf{v} + (\nabla\mathbf{v})^T], \tag{58}$$

where $\dot{\gamma}$ is the shear rate tensor.

The gradient of the velocity vector is written as:

$$\nabla\mathbf{v} = \mathbf{e}_r\frac{\partial}{\partial r}(v_r\mathbf{e}_r + v_z\mathbf{e}_z) + \frac{1}{r}\mathbf{e}_\theta\frac{\partial}{\partial\theta}(v_r\mathbf{e}_r + v_z\mathbf{e}_z) + \mathbf{e}_z\frac{\partial}{\partial z}(v_r\mathbf{e}_r + v_z\mathbf{e}_z) \tag{59}$$

Equation 59 can be simplified using the product rule and the relations of derivatives of unit base vectors (Eqs. A.7), which yields:

$$\nabla\mathbf{v} = \mathbf{e}_r\mathbf{e}_r\frac{\partial v_r}{\partial r} + \mathbf{e}_r\mathbf{e}_z\frac{\partial v_z}{\partial r} + \frac{v_r}{r}\mathbf{e}_\theta\mathbf{e}_\theta + \mathbf{e}_z\mathbf{e}_r\frac{\partial v_r}{\partial z} + \mathbf{e}_z\mathbf{e}_z\frac{\partial v_z}{\partial z} \tag{60}$$

By interchanging the order of the unit base vectors, the transpose of the gradient of the velocity vector is found as:

$$(\nabla\mathbf{v})^T = \mathbf{e}_r\mathbf{e}_r\frac{\partial v_r}{\partial r} + \mathbf{e}_z\mathbf{e}_r\frac{\partial v_z}{\partial r} + \frac{v_r}{r}\mathbf{e}_\theta\mathbf{e}_\theta + \mathbf{e}_r\mathbf{e}_z\frac{\partial v_r}{\partial z} + \mathbf{e}_z\mathbf{e}_z\frac{\partial v_z}{\partial z} \tag{61}$$

Equations 60 and 61 are then used to express the the shear rate tensor as:

$$\dot{\gamma} = (\nabla\mathbf{v} + (\nabla\mathbf{v})^T) = 2\mathbf{e}_r\mathbf{e}_r\frac{\partial v_r}{\partial r} + (\mathbf{e}_r\mathbf{e}_z + \mathbf{e}_z\mathbf{e}_r)\frac{\partial v_z}{\partial r} + 2\frac{v_r}{r}\mathbf{e}_\theta\mathbf{e}_\theta + (\mathbf{e}_r\mathbf{e}_z + \mathbf{e}_z\mathbf{e}_r)\frac{\partial v_r}{\partial z} + 2\mathbf{e}_z\mathbf{e}_z\frac{\partial v_z}{\partial z} \tag{62}$$

Thus, the viscous stress tensor in Eq. 58 can be rewritten as:

$$\tau_c = -\mu_c \left[2\mathbf{e}_r\mathbf{e}_r \frac{\partial v_r}{\partial r} + (\mathbf{e}_r\mathbf{e}_z + \mathbf{e}_z\mathbf{e}_r)\frac{\partial v_z}{\partial r} + 2\frac{v_r}{r}\mathbf{e}_\theta\mathbf{e}_\theta + (\mathbf{e}_r\mathbf{e}_z + \mathbf{e}_z\mathbf{e}_r)\frac{\partial v_r}{\partial z} + 2\mathbf{e}_z\mathbf{e}_z\frac{\partial v_z}{\partial z} \right] \tag{63}$$

Furthermore, by inserting the obtained expression for the viscous stress tensor into Eq. 57, the first term in the normal stress balance in Eq. 55 becomes:

$$\begin{aligned}(\mathtt{T}_c : \mathbf{nn}) = \Bigg\{ & -P_c(\mathbf{e}_r\mathbf{e}_r + \mathbf{e}_\theta\mathbf{e}_\theta + \mathbf{e}_z\mathbf{e}_z) - \mu_c \left[2\mathbf{e}_r\mathbf{e}_r \frac{\partial v_r}{\partial r} + (\mathbf{e}_r\mathbf{e}_z + \mathbf{e}_z\mathbf{e}_r)\frac{\partial v_z}{\partial r} + 2\frac{v_r}{r}\mathbf{e}_\theta\mathbf{e}_\theta \right. \\ & \left. + (\mathbf{e}_r\mathbf{e}_z + \mathbf{e}_z\mathbf{e}_r)\frac{\partial v_r}{\partial z} + 2\mathbf{e}_z\mathbf{e}_z\frac{\partial v_z}{\partial z} \right] \Bigg\} : \frac{\mathbf{e}_z - \frac{1}{2}\frac{\partial h}{\partial r}\mathbf{e}_r}{\sqrt{1 + \frac{1}{4}\left(\frac{\partial h}{\partial r}\right)^2}} \frac{\mathbf{e}_z - \frac{1}{2}\frac{\partial h}{\partial r}\mathbf{e}_r}{\sqrt{1 + \frac{1}{4}\left(\frac{\partial h}{\partial r}\right)^2}}\end{aligned} \tag{64}$$

Employing the definition of the double dot product of unit base vectors (see Eq. A.6) reduces Eq. 64 to:

$$(\mathtt{T}_c : \mathbf{nn}) = -P_c - \frac{\mu_c}{1 + \frac{1}{4}\left(\frac{\partial h}{\partial r}\right)^2} \left[\frac{1}{2}\frac{\partial v_r}{\partial r}\left(\frac{\partial h}{\partial r}\right)^2 - \frac{\partial v_z}{\partial r}\frac{\partial h}{\partial r} - \frac{\partial v_r}{\partial z}\frac{\partial h}{\partial r} + 2\frac{\partial v_z}{\partial z} \right] \tag{65}$$

In the dispersed phase, the viscous stresses are assumed negligible due to the assumption of gentle collision. Then, the second term in the normal stress balance becomes:

$$(\mathtt{T}_d : \mathbf{nn}) = -P_d \tag{66}$$

The curvature, $2H$, is defined as:

$$2H = \frac{1}{2r}\frac{\partial}{\partial r}\left(r\frac{\partial h}{\partial r} \right) \tag{67}$$

Note that the derivation of the curvature expression is given in App. C.3. By inserting the curvature in the last term of the normal stress balance in Eq. 55 and taking the dot product of the normal vector with itself (which gives 1, as can be seen from the dot product definition in Eq. A.3), the term can be expressed as:

$$2H\sigma(\mathbf{n}\cdot\mathbf{n}) = \frac{1}{2r}\frac{\partial}{\partial r}\left(r\frac{\partial h}{\partial r} \right)\sigma \tag{68}$$

The normal stress balance can now be rewritten as:

$$-P_c - \frac{\mu_c}{1 + \frac{1}{4}\left(\frac{\partial h}{\partial r}\right)^2} \left[\frac{1}{2}\frac{\partial v_r}{\partial r}\left(\frac{\partial h}{\partial r}\right)^2 - \frac{\partial v_z}{\partial r}\frac{\partial h}{\partial r} - \frac{\partial v_r}{\partial z}\frac{\partial h}{\partial r} + 2\frac{\partial v_z}{\partial z} \right] + P_d = \frac{1}{2r}\frac{\partial}{\partial r}\left(r\frac{\partial h}{\partial r} \right)\sigma, \tag{69}$$

The pressure difference across the interface of a perfectly spherical particle is given by:

$$P_{d,0} - P_{c,0} = \frac{2\sigma}{R_p} \tag{70}$$

Furthermore, excess pressure for the continuous phase, $P_{ex,c}$, can be expressed as:

$$P_{ex,c} = P_c - P_{c,0} \tag{71}$$

Because of the gentle collision assumption, the particle-side pressure difference is neglected:

$$P_{ex,d} = P_d - P_{d,0} \approx 0 \tag{72}$$

The excess pressure in the whole system is determined as the difference between the excess pressure in both phases, which gives:

$$P = P_{ex,c} - P_{ex,d} = P_c - P_{c,0}. \tag{73}$$

Subtracting the normal stress balance from the pressure difference across the interface of a perfect sphere results in:

$$P + \frac{\mu_c}{1+\frac{1}{4}\left(\frac{\partial h}{\partial r}\right)^2}\left[\frac{1}{2}\frac{\partial v_r}{\partial r}\left(\frac{\partial h}{\partial r}\right)^2 - \frac{\partial v_z}{\partial r}\frac{\partial h}{\partial r} - \frac{\partial v_r}{\partial z}\frac{\partial h}{\partial r} + 2\frac{\partial v_z}{\partial z}\right] = \frac{2\sigma}{R_p} - \frac{1}{2r}\frac{\partial}{\partial r}\left(r\frac{\partial h}{\partial r}\right)\sigma, \tag{74}$$

The first term in the tangential stress balance in Eq. 56 can be expressed as:

$$\begin{aligned}(\mathtt{T}_c : \mathbf{nt}_1) = \Bigg\{ & -P_c(\mathbf{e}_r\mathbf{e}_r + \mathbf{e}_\theta\mathbf{e}_\theta + \mathbf{e}_z\mathbf{e}_z) - \mu_c\left[2\mathbf{e}_r\mathbf{e}_r\frac{\partial v_r}{\partial r} + (\mathbf{e}_r\mathbf{e}_z + \mathbf{e}_z\mathbf{e}_r)\frac{\partial v_z}{\partial r} + 2\frac{v_r}{r}\mathbf{e}_\theta\mathbf{e}_\theta\right. \\ & \left.+(\mathbf{e}_r\mathbf{e}_z + \mathbf{e}_z\mathbf{e}_r)\frac{\partial v_r}{\partial z} + 2\mathbf{e}_z\mathbf{e}_z\frac{\partial v_z}{\partial z}\right]\Bigg\} : \frac{\mathbf{e}_z - \frac{1}{2}\frac{\partial h}{\partial r}\mathbf{e}_r}{\sqrt{1+\frac{1}{4}\left(\frac{\partial h}{\partial r}\right)^2}}\frac{\mathbf{e}_r + \frac{1}{2}\frac{\partial h}{\partial r}\mathbf{e}_z}{\sqrt{1+\frac{1}{4}\left(\frac{\partial h}{\partial r}\right)^2}}\end{aligned} \tag{75}$$

By performing the double dot product, Eq. 75 is rewritten to:

$$(\mathtt{T}_c : \mathbf{nt_1}) = -\frac{\mu_c}{1+\frac{1}{4}\left(\frac{\partial h}{\partial r}\right)^2}\left\{-\frac{\partial v_r}{\partial r}\frac{\partial h}{\partial r} + \left[1 - \frac{1}{4}\left(\frac{\partial h}{\partial r}\right)^2\right]\left(\frac{\partial v_z}{\partial r} + \frac{\partial v_r}{\partial z}\right) + \frac{\partial v_z}{\partial z}\frac{\partial h}{\partial r}\right\} \tag{76}$$

Moreover, the second term in the tangential stress balance is defined by:

$$(\mathtt{T}_d : \mathbf{nt_1}) = \tau_d \tag{77}$$

Here, τ_d is the particle side tangential stress evaluated at the interface.

The tangential stress balance can now be rewritten to:

$$-\frac{\mu_c}{1+\frac{1}{4}\left(\frac{\partial h}{\partial r}\right)^2}\left\{-\frac{\partial v_r}{\partial r}\frac{\partial h}{\partial r}+\left[1-\frac{1}{4}\left(\frac{\partial h}{\partial r}\right)^2\right]\left(\frac{\partial v_z}{\partial r}+\frac{\partial v_r}{\partial z}\right)+\frac{\partial v_z}{\partial z}\frac{\partial h}{\partial r}\right\}-\tau_d=0 \tag{78}$$

2.1.3 Non-dimensionalization

The given equations can be simplified by reducing them to dimensionless form. A dimensionless variable, $\tilde{x}$, is defined as:

$$\tilde{x}=\frac{x}{\bar{x}}. \tag{79}$$

Here, x is a variable with dimension, and $\bar{x}$ is the characteristic scale with the corresponding dimension.

Expressing the systems variables in this form gives the following transformations:

$$P=\bar{P}\tilde{P}, \quad z=\bar{h}\tilde{z}, \quad h=\bar{h}\tilde{h}, \quad r=\bar{r}\tilde{r}, \quad v_r=\bar{v_r}\tilde{v_r}, \quad v_z=\bar{v_z}\tilde{v_z}, \quad t=\bar{t}\tilde{t}, \quad \tau_d=\bar{\tau_d}\tilde{\tau_d} \tag{80}$$

Note that U_t and V_{app} scales in the same way as v_r and v_z, respectively.

Due to the gentle collision assumption, the lubrication theory is applicable within the thin film. This theory assumes that the length scales in the interface directions are significantly larger than in the normal direction to the interface. Thus, the film thickness and the radial length scales can be related by:

$$\frac{\bar{h}}{\bar{r}}=\varepsilon << 1 \tag{81}$$

Furthermore, the characteristic radial length scale of the thin film, $\bar{r}$, is assumed to be related with the equivalent radius, R_p, via (Ozan & Jakobsen 2019*a*):

$$\bar{r}=\varepsilon R_p \tag{82}$$

Based on Eqs. 81 and 82, expressions for the characteristic scales for the system can be derived by non-dimensionalizing the derived model equations in the following manner:

1. Substitute all variables in the model equations with the expressions provided in Eq. 80
2. Divide by one of the coefficients such that all terms become dimensionless
3. Compare the magnitude of the terms and consider if any of them can be neglected
4. Determine the unknown characteristic scales by balancing the dominant terms
5. Rewrite the model equations in terms of their new dimensionless quantities

First, the continuity equation is non-dimensonalized. This is done by inserting the expressions in Eq. 80 into the continuity equation (Eq.12), which yields:

$$\frac{\bar{v_r}}{\bar{r}}\frac{1}{\tilde{r}}\frac{\partial}{\partial\tilde{r}}(\tilde{r}\tilde{v_r})+\frac{\bar{v_z}}{\bar{h}}\frac{\partial\tilde{v_z}}{\partial\tilde{z}}=0 \tag{83}$$

To conserve the mass, the two terms are assumed to be of similar magnitude and therefore balance each other. Hence, the characteristic scale for the axial velocity can be expressed by:

$$\bar{v_z}=\frac{\bar{h}\bar{v_r}}{\bar{r}} \tag{84}$$

Inserting Eq. 81 then gives:

$$\bar{v_z}=\varepsilon\bar{v_r} \tag{85}$$

Thus, the dimensionless continuity equation can be written as:

$$\frac{1}{\tilde{r}}\frac{\partial}{\partial\tilde{r}}(\tilde{r}\tilde{v_r})+\frac{\partial\tilde{v_z}}{\partial\tilde{z}}=0 \tag{86}$$

To find an expression for the characteristic time scale, $\bar{t}$, the kinematic condition (Eq. 53) is non-dimensionalized. Replacing the variables with the expressions in Eq. 80 and employing the relation in Eq. 81 gives:

$$\frac{\varepsilon\bar{v_r}\tilde{v_z}-\frac{1}{2}\frac{\varepsilon\bar{r}\bar{v_r}}{\bar{r}}\frac{\partial\tilde{h}}{\partial\tilde{r}}\tilde{v_r}}{\sqrt{1+\frac{1}{4}\frac{\varepsilon^2\bar{r}^2}{\bar{r}^2}\left(\frac{\partial h}{\partial r}\right)^2}}=\frac{1}{2}\frac{\varepsilon\bar{r}}{\bar{t}}\frac{\partial\tilde{h}}{\partial\tilde{t}} \tag{87}$$

By comparing the magnitude of the terms in the denominator, here, the second term is assumed negligible because it contains ε^2. Hence, the denominator is simplified to 1, which yields:

$$\bar{v_r}\tilde{v_z}-\frac{\bar{v_r}}{2}\frac{\partial\tilde{h}}{\partial\tilde{r}}\tilde{v_r}=\frac{1}{2}\frac{\bar{r}}{\bar{t}}\frac{\partial\tilde{h}}{\partial\tilde{t}} \tag{88}$$

Dividing by the coefficient in the first term, $\bar{v_r}$, results in:

$$\tilde{v_z}-\frac{1}{2}\frac{\partial\tilde{h}}{\partial\tilde{r}}\tilde{v_r}=\frac{1}{2}\frac{\bar{r}}{\bar{t}\bar{v_r}}\frac{\partial\tilde{h}}{\partial\tilde{t}} \tag{89}$$

Balancing the coefficients gives the following expression for the characteristic time scale:

$$\bar{t}=\frac{\bar{h}}{\varepsilon\bar{v_r}}=\frac{\bar{h}}{\bar{v_z}} \tag{90}$$

Thus, the dimensionless kinematic condition can be rewritten as:

$$\tilde{v_z}-\frac{1}{2}\frac{\partial\tilde{h}}{\partial\tilde{r}}\tilde{v_r}=\frac{1}{2}\frac{\partial\tilde{h}}{\partial\tilde{t}} \tag{91}$$

Moreover, applying the expression in Eq. 80 on the radial component of the equation of motion presented in Eq. 24 gives:

$$\begin{aligned}&\rho\left[\frac{\varepsilon\bar{v_r}^2}{\bar{h}}\frac{\partial\tilde{v_r}}{\partial\tilde{t}}+\frac{\varepsilon\bar{v_r}^2}{\bar{h}}\frac{1}{\tilde{r}}\frac{\partial}{\partial\tilde{r}}(\tilde{r}\tilde{v_r}\tilde{v_r})+\frac{\varepsilon\bar{v_r}^2}{\bar{h}}\frac{\partial}{\partial\tilde{z}}(\tilde{v_z}\tilde{v_r})\right]\\&=-\frac{\bar{P}}{\bar{r}}\frac{\partial\tilde{P}}{\partial\tilde{r}}+\frac{\varepsilon\bar{v_r}}{\bar{h}}\frac{1}{\tilde{r}}\frac{\partial}{\partial\tilde{r}}\left(2\mu_c\tilde{r}\frac{\partial\tilde{v_r}}{\partial\tilde{r}}\right)-2\mu_c\frac{\varepsilon^2\bar{v_r}^2}{\bar{h}^2}\frac{\tilde{v_r}}{\tilde{r}^2}+\frac{1}{\bar{h}}\frac{\partial}{\partial\tilde{z}}\left(\mu_c\left[\frac{\varepsilon^2\bar{v_r}}{\bar{h}}\frac{\partial\tilde{v_z}}{\partial\tilde{r}}+\frac{\bar{v_r}}{\bar{h}}\frac{\partial\tilde{v_r}}{\partial\tilde{z}}\right]\right)\end{aligned}\tag{92}$$

Then, Eq. 92 is divided by the coefficient, $\rho\frac{\varepsilon\bar{v_r}^2}{\bar{h}}$, which yields:

$$\begin{aligned}&\frac{\partial\tilde{v_r}}{\partial\tilde{t}}+\frac{1}{\tilde{r}}\frac{\partial}{\partial\tilde{r}}(\tilde{r}\tilde{v_r}\tilde{v_r})+\frac{\partial}{\partial\tilde{z}}(\tilde{v_z}\tilde{v_r})\\&=-\frac{\bar{P}\bar{h}}{\varepsilon\rho\bar{r}\bar{v_r}^2}\frac{\partial\tilde{P}}{\partial\tilde{r}}+\frac{1}{\rho\bar{v_r}}\frac{1}{\tilde{r}}\frac{\partial}{\partial\tilde{r}}\left(2\mu_c\tilde{r}\frac{\partial\tilde{v_r}}{\partial\tilde{r}}\right)-2\mu_c\frac{\varepsilon}{\rho\bar{h}}\frac{\tilde{v_r}}{\tilde{r}^2}+\frac{1}{\rho}\frac{\partial}{\partial\tilde{z}}\left(\mu_c\left[\frac{\varepsilon}{\bar{h}\bar{v_r}}\frac{\partial\tilde{v_z}}{\partial\tilde{r}}+\frac{1}{\varepsilon\bar{h}\bar{v_r}}\frac{\partial\tilde{v_r}}{\partial\tilde{z}}\right]\right)\end{aligned}\tag{93}$$

By comparing the magnitude of the terms, only the terms which includes ε in the denominator are determined to be significant. Hence, Eq. 93 simplifies to:

$$\frac{\bar{P}\bar{h}}{\varepsilon\rho\bar{r}\bar{v_r}^2}\frac{\partial\tilde{P}}{\partial\tilde{r}}=\frac{1}{\rho}\frac{\partial}{\partial\tilde{z}}\left(\mu_c\,\frac{1}{\varepsilon\bar{h}\bar{v_r}}\frac{\partial\tilde{v_r}}{\partial\tilde{z}}\right)\tag{94}$$

Balancing the coefficients, gives the following characteristic pressure scale:

$$\bar{P}=\frac{\mu_c\bar{r}\bar{v_r}}{\bar{h}^2}=\frac{\mu_c\bar{v_r}}{\varepsilon\bar{h}}\tag{95}$$

Thus, the dimensionless r-component of the equation of motion can be expressed as:

$$\frac{\partial\tilde{P}}{\partial\tilde{r}}=\frac{\partial}{\partial\tilde{z}}\left(\frac{\partial\tilde{v_r}}{\partial\tilde{z}}\right)\tag{96}$$

Furthermore, upon substitution of the variables in Eq. 80, the normal stress balance is written as:

$$\begin{aligned}&\frac{\mu_c\bar{v_r}}{\varepsilon^3R_p}\tilde{P}+\frac{\mu_c}{1+\frac{1}{4}\varepsilon^2\left(\frac{\partial\tilde{h}}{\partial\tilde{r}}\right)^2}\left[\frac{1}{2}\frac{\varepsilon\bar{v_r}}{R_p}\frac{\partial\tilde{v_r}}{\partial\tilde{r}}\left(\frac{\partial\tilde{h}}{\partial\tilde{r}}\right)^2-\frac{\varepsilon\bar{v_r}}{R_p}\frac{\partial\tilde{v_z}}{\partial\tilde{r}}\frac{\partial\tilde{h}}{\partial\tilde{r}}-\frac{\bar{v_r}}{\varepsilon R_p}\frac{\partial\tilde{v_r}}{\partial\tilde{z}}\frac{\partial\tilde{h}}{\partial\tilde{r}}+2\frac{\bar{v_r}}{\varepsilon R_p}\frac{\partial\tilde{v_z}}{\partial\tilde{z}}\right]\\&=\frac{2\sigma}{R_p}-\frac{1}{R_p}\frac{1}{2\tilde{r}}\frac{\partial}{\partial\tilde{r}}\left(\tilde{r}\frac{\partial\tilde{h}}{\partial\tilde{r}}\right)\sigma.\end{aligned}\tag{97}$$

Dividing by $\frac{\sigma}{R_p}$ yields:

$$\begin{aligned}&\frac{\mu_c\bar{v_r}}{\varepsilon^3\sigma}\tilde{P}+\frac{\mu_c}{1+\frac{1}{4}\varepsilon^2\left(\frac{\partial\tilde{h}}{\partial\tilde{r}}\right)^2}\left[\frac{1}{2}\frac{\varepsilon\bar{v_r}}{\sigma}\frac{\partial\tilde{v_r}}{\partial\tilde{r}}\left(\frac{\partial\tilde{h}}{\partial\tilde{r}}\right)^2-\frac{\varepsilon\bar{v_r}}{\sigma}\frac{\partial\tilde{v_z}}{\partial\tilde{r}}\frac{\partial\tilde{h}}{\partial\tilde{r}}-\frac{\bar{v_r}}{\varepsilon\sigma}\frac{\partial\tilde{v_r}}{\partial\tilde{z}}\frac{\partial\tilde{h}}{\partial\tilde{r}}+2\frac{\bar{v_r}}{\varepsilon\sigma}\frac{\partial\tilde{v_z}}{\partial\tilde{z}}\right]\\&=2-\frac{1}{2\tilde{r}}\frac{\partial}{\partial\tilde{r}}\left(\tilde{r}\frac{\partial\tilde{h}}{\partial\tilde{r}}\right)\end{aligned}\tag{98}$$

In comparison with the pressure term, all the viscous terms are here of much smaller magnitude, and are therefore neglected. However, the curvature term on the right-hand side is kept due to the knowledge of a curved interface in the system. Without this term, the interface would be non-deformable, i.e., its shape is conserved throughout the collision. The normal stress balance can then be simplified to:

$$\frac{\mu_c \bar{v_r}}{\varepsilon^3 \sigma} \tilde{P} = 2 - \frac{1}{2\tilde{r}} \frac{\partial}{\partial \tilde{r}} \left(\tilde{r} \frac{\partial \tilde{h}}{\partial \tilde{r}} \right), \tag{99}$$

By balancing the coefficients, the characteristic radial velocity scale is found as:

$$\bar{v_r} = \frac{\varepsilon^3 \sigma}{\mu_c} \tag{100}$$

Inserting the obtained radial velocity scale into the pressure scale in Eq. 95 results in the following expression:

$$\bar{P} = \frac{\varepsilon^2 \sigma}{\bar{h}} \tag{101}$$

The dimensionless normal stress balance is then written as:

$$\tilde{P} = 2 - \frac{1}{2\tilde{r}} \frac{\partial}{\partial \tilde{r}} \left(\tilde{r} \frac{\partial \tilde{h}}{\partial \tilde{r}} \right) \tag{102}$$

By employing the variable transformation in Eq.80, the tangential stress balance is expressed as:

$$- \frac{\mu_c}{1 + \frac{1}{4}\varepsilon^2 \left(\frac{\partial \tilde{h}}{\partial \tilde{r}} \right)^2} \left[\varepsilon \frac{\bar{v_r}}{\bar{r}} \left(- \frac{\partial \tilde{v_r}}{\partial \tilde{r}} \right) \left(\frac{\partial \tilde{h}}{\partial \tilde{r}} \right) + \left[1 - \frac{1}{4}\varepsilon^2 \left(\frac{\partial \tilde{h}}{\partial \tilde{r}} \right)^2 \right] \left(\frac{\varepsilon \bar{v_r}}{\bar{r}} \frac{\partial \tilde{v_z}}{\partial \tilde{r}} + \frac{\bar{v_r}}{\varepsilon \bar{r}} \frac{\partial \tilde{v_r}}{\partial \tilde{z}} \right) + \left(\frac{\varepsilon \bar{v_r}}{\bar{r}} \frac{\partial \tilde{v_z}}{\partial \tilde{z}} \right) \left(\frac{\partial \tilde{h}}{\partial \tilde{r}} \right) \right]$$
$$- \bar{\tau_d} \tilde{\tau_d} = 0 \tag{103}$$

The common denominator is simplified to 1 by use of the difference in magnitude argument. Equation 103 is further divided by the coefficient, $\frac{\varepsilon \mu_c \bar{v_r}}{\bar{r}}$, and can be rearranged to:

$$\frac{\partial \tilde{v_r}}{\partial \tilde{r}} \frac{\partial \tilde{h}}{\partial \tilde{r}} + \left[\frac{1}{4}\varepsilon^2 \left(\frac{\partial \tilde{h}}{\partial \tilde{r}} \right)^2 - 1 \right] \left(\frac{\partial \tilde{v_z}}{\partial \tilde{r}} \frac{1}{\varepsilon^2} \frac{\partial \tilde{v_r}}{\partial \tilde{z}} \right) - \frac{\partial \tilde{v_z}}{\partial \tilde{z}} \frac{\partial \tilde{h}}{\partial \tilde{r}} - \frac{\bar{\tau_d} \bar{r}}{\varepsilon \mu_c \bar{v_r}} \tilde{\tau_d} = 0 \tag{104}$$

By comparing the magnitude of the terms, only the terms with ε in the denominator are considered to be momentous. Thus, the tangential stress balance can be rewritten as:

$$- \mu_c \frac{\bar{v_r}}{\varepsilon \bar{r}} \frac{\partial \tilde{v_r}}{\partial \tilde{z}} - \bar{\tau_d} \tilde{\tau_d} = 0 \tag{105}$$

Balancing the coefficients results in:

$$\bar{\tau}_d = \frac{\mu_c \bar{v}_r}{\varepsilon \bar{r}} \tag{106}$$

Hence, the dimensionless tangential stress balance can be expressed as:

$$-\frac{\partial \tilde{v}_r}{\partial \tilde{z}} = \tilde{\tau}_d \tag{107}$$

By inserting Eq. 81 and 82 into the obtained characteristic scales (Eqs. 85, 90 , 100, 101, 106) they can be rewritten as:

$$\bar{P} = \frac{\sigma}{R_p}, \quad \bar{h} = \varepsilon^2 R_p, \quad \bar{r} = \varepsilon R_p, \quad \bar{v_r} = \frac{\varepsilon^3 \sigma}{\mu_c}, \quad \bar{v_z} = \frac{\varepsilon^4 \sigma}{\mu_c}, \quad \bar{t} = \frac{R_p \mu_c}{\varepsilon^2 \sigma}, \quad \bar{\tau_d} = \frac{\varepsilon \sigma}{R_p} \tag{108}$$

The z-component of the equation of motion is non-dimensionalized by applying the characteristic scales in Eq. 108, which yields:

$$\begin{aligned} &\rho \left[\frac{\varepsilon^6 \sigma^2}{R_p \mu_c^2} \frac{\partial \tilde{v_z}}{\partial \tilde{t}} + \frac{\varepsilon^6 \sigma}{\mu_c R_p} \frac{1}{\tilde{r}} \frac{\partial}{\partial \tilde{r}} (\tilde{r} \tilde{v_r} \tilde{v_z}) + \frac{\varepsilon^3 \sigma}{\mu_c R_p} \frac{\partial}{\partial \tilde{z}} (\tilde{v_z} \tilde{v_z}) \right] \\ &= -\frac{\sigma}{\varepsilon^2 R_p^2} \frac{\partial \tilde{P}}{\partial \tilde{z}} + \frac{\partial}{\partial \tilde{r}} \left[\mu_c \left(\frac{\varepsilon^2 \sigma}{\mu_c R_p^2} \frac{\partial \tilde{v_z}}{\partial \tilde{r}} + \frac{\sigma}{\mu_c R_p^2} \frac{\partial \tilde{v_r}}{\partial \tilde{z}} \right) \right] + \frac{\sigma}{\mu_c R_p^2} \frac{\partial}{\partial \tilde{z}} \left(2 \mu_c \frac{\partial \tilde{v_z}}{\partial \tilde{z}} \right) \end{aligned} \tag{109}$$

Equation 109 is then divided by the pressure term coefficient, which gives:

$$\begin{aligned} &\rho \left[\frac{\varepsilon^8 \sigma R_p}{\mu_c^2} \frac{\partial \tilde{v_z}}{\partial \tilde{t}} + \frac{\varepsilon^8 R_p}{\mu_c} \frac{1}{\tilde{r}} \frac{\partial}{\partial \tilde{r}} (\tilde{r} \tilde{v_r} \tilde{v_z}) + \frac{\varepsilon^5 R_p}{\mu_c} \frac{\partial}{\partial \tilde{z}} (\tilde{v_z} \tilde{v_z}) \right] \\ &= -\frac{\partial \tilde{P}}{\partial \tilde{z}} + \frac{\partial}{\partial \tilde{r}} \left(\varepsilon^4 \frac{\partial \tilde{v_z}}{\partial \tilde{r}} + \varepsilon^2 \frac{\partial \tilde{v_r}}{\partial \tilde{z}} \right) + \varepsilon^2 \frac{\partial}{\partial \tilde{z}} \left(2 \frac{\partial \tilde{v_z}}{\partial \tilde{z}} \right) \end{aligned} \tag{110}$$

As the pressure term is the only term without ε in the nominator, all the other terms are neglected. Thus, the dimensionless z-component of the equation of motion becomes can be reduced to:

$$\frac{\partial \tilde{P}}{\partial \tilde{z}} = 0 \tag{111}$$

Non-dimensionalizing the no-slip condition results in:

$$\frac{\frac{\varepsilon^3 \sigma}{\mu_c} \tilde{v_r} + \frac{1}{2} \frac{\varepsilon^5 \sigma}{\mu_c} \frac{\partial \tilde{h}}{\partial \tilde{r}} \tilde{v_z}}{\sqrt{1 + \frac{1}{4} \varepsilon^2 \left(\frac{\partial \tilde{h}}{\partial \tilde{r}} \right)^2}} = \frac{\varepsilon^3 \sigma}{\mu_c} \tilde{U}_t. \tag{112}$$

As with the kinematic condition, the denominator can be simplified to 1, which gives:

$$\frac{\varepsilon^3 \sigma}{\mu_c} \tilde{v_r} + \frac{1}{2} \frac{\varepsilon^5 \sigma}{\mu_c} \frac{\partial \tilde{h}}{\partial \tilde{r}} \tilde{v_z} = \frac{\varepsilon^3 \sigma}{\mu_c} \tilde{U}_t, \tag{113}$$

Dividing by the velocity coefficient $\frac{\varepsilon^3\sigma}{\mu_c}$, results in:

$$\tilde{v_r} + \frac{1}{2}\varepsilon^2 \frac{\partial \tilde{h}}{\partial \tilde{r}} \tilde{v_z} = \tilde{U_t}, \tag{114}$$

By comparing the magnitude of the terms, the second term is assumed negligible. Thus, the no-slip condition simplifies to:

$$\tilde{v_r} = \tilde{U_t} \tag{115}$$

2.2 Non-Newtonian model

The derived model will now be extended to account for the non-Newtonian continuous phase. As non-Newtonian fluids do not follow Newton's law of viscosity, empirical expressions for the stress tensor are applied where viscosity is considered a function of the magnitude of the shear rate tensor. Note that within this model, the non-Newtonian fluid is described as a generalized Newtonian fluid. Hence, no elasticity is considered; only viscous effects are present. This derivation aims to obtain the thinning equation and the pressure equation, which will be solved numerically with three different solvers. The solvers correspond to the interfaces' different degrees of tangential mobility, which is considered either immobile, partially mobile, or fully mobile.

The stress tensor is defined by:

$$\tau_c = -\eta(\dot{\gamma})\dot{\gamma} = -\eta(\dot{\gamma})(\nabla \mathbf{v} + (\nabla \mathbf{v})^T) \tag{116}$$

Here, $\eta(\dot{\gamma})$ is the non-Newtonian viscosity that is a function of the magnitude of the shear rate tensor. To express this viscosity, the power law model is applied:

$$\eta(\dot{\gamma}) = m\dot{\gamma}^{n-1}, \tag{117}$$

As mentioned in the introduction, m is the flow consistency index, and n is the power index, which corresponds to:

- If $0 < n < 1$: shear-thinning fluid
- If $n = 1$: Newtonian fluid
- If $n > 1$: shear-thickening fluid

Inserting the power law gives the following expression for the stress tensor:

$$\tau_c = -m\dot{\gamma}^{n-1}(\nabla \mathbf{v} + (\nabla \mathbf{v})^T), \tag{118}$$

where the magnitude of the shear rate tensor, $\dot{\gamma}$, is defined by:

$$\dot{\gamma} = \sqrt{\frac{1}{2}\dot{\gamma} : \dot{\gamma}} \tag{119}$$

Furthermore, the double dot product of the shear rate tensor in Eq. 62 with itself can be written as:

$$\dot{\gamma} : \dot{\gamma} = 4\frac{\partial v_r}{\partial r}\frac{\partial v_r}{\partial r} + 2\frac{\partial v_z}{\partial r}\frac{\partial v_z}{\partial r} + 4\frac{\partial v_z}{\partial r}\frac{\partial v_r}{\partial z} + 2\frac{\partial v_r}{\partial z}\frac{\partial v_r}{\partial z} + 4\frac{v_r^2}{r^2} + 4\frac{\partial v_z}{\partial z}\frac{\partial v_z}{\partial z} \tag{120}$$

By inserting the characteristic scales given in Eq. 108, Eq. 120 becomes:

$$\begin{aligned}\dot{\gamma} : \dot{\gamma} = \left(\frac{\sigma}{\mu_c R_p}\right)^2 \Bigg[& 4\varepsilon^4 \frac{\partial \tilde{v_r}}{\partial \tilde{r}}\frac{\partial \tilde{v_r}}{\partial \tilde{r}} + 2\varepsilon^6 \frac{\partial \tilde{v_z}}{\partial \tilde{r}}\frac{\partial \tilde{v_z}}{\partial \tilde{r}} + 4\varepsilon^4 \frac{\partial \tilde{v_z}}{\partial \tilde{r}}\frac{\partial \tilde{v_r}}{\partial \tilde{z}} + 2\varepsilon^2 \frac{\partial \tilde{v_r}}{\partial \tilde{z}}\frac{\partial \tilde{v_r}}{\partial \tilde{z}} + 4\varepsilon^4 \frac{\tilde{v_r}^2}{\tilde{r}^2} \\ & + 4\varepsilon^4 \frac{\partial \tilde{v_z}}{\partial \tilde{z}}\frac{\partial \tilde{v_z}}{\partial \tilde{z}} \Bigg]\end{aligned} \tag{121}$$

Now the magnitudes of the terms can be compared. Here, the fourth term on the right-hand side is determined to be much more significant than all the other terms which therefore are neglected. Hence, the magnitude of the shear rate tensor can be reduced to:

$$\dot{\gamma} = \sqrt{\frac{1}{2}\dot{\gamma} : \dot{\gamma}} \approx \sqrt{\varepsilon^2 \left(\frac{\sigma}{\mu_c R_p}\right)^2 \frac{\partial \tilde{v_r}}{\partial \tilde{z}}\frac{\partial \tilde{v_r}}{\partial \tilde{z}}} = \left|\frac{\varepsilon\sigma}{\mu_c R_p}\frac{\partial \tilde{v_r}}{\partial \tilde{z}}\right| = \left|\frac{\partial v_r}{\partial z}\right| \tag{122}$$

By inserting the obtained expression for the shear rate tensor into the power law in Eq. 117, the power law can be rewritten as:

$$\eta = m\left|\frac{\partial v_r}{\partial z}\right|^{n-1} \tag{123}$$

Furthermore, combining Eqs. 62, 118 and 122, gives the following expression for the viscous stress tensor:

$$\tau_c = -m\left|\frac{\partial v_r}{\partial z}\right|^{n-1}\left[2\mathbf{e}_r\mathbf{e}_r\frac{\partial v_r}{\partial r} + (\mathbf{e}_r\mathbf{e}_z + \mathbf{e}_z\mathbf{e}_r)\frac{\partial v_z}{\partial r} + 2\frac{v_r}{r}\mathbf{e}_\theta\mathbf{e}_\theta + (\mathbf{e}_r\mathbf{e}_z + \mathbf{e}_z\mathbf{e}_r)\frac{\partial v_r}{\partial z} + 2\mathbf{e}_z\mathbf{e}_z\frac{\partial v_z}{\partial z}\right] \tag{124}$$

The obtained power law expression for the non-Newtonian viscosity will be applied later on in the derivation. For now, the viscous stress tensor is employed as:

$$\tau_c = -\eta\left[2\mathbf{e}_r\mathbf{e}_r\frac{\partial v_r}{\partial r} + (\mathbf{e}_r\mathbf{e}_z + \mathbf{e}_z\mathbf{e}_r)\frac{\partial v_z}{\partial r} + 2\frac{v_r}{r}\mathbf{e}_\theta\mathbf{e}_\theta + (\mathbf{e}_r\mathbf{e}_z + \mathbf{e}_z\mathbf{e}_r)\frac{\partial v_r}{\partial z} + 2\mathbf{e}_z\mathbf{e}_z\frac{\partial v_z}{\partial z}\right] \tag{125}$$

Notice that the only difference between the non-Newtonian viscous stress tensor and the Newtonian in Eq. 63 is that the viscosity is non-constant for the non-Newtonian case. Furthermore, the viscous stress tensor only occurs in the equation of motion and the stress balance components. Hence, the other equations remain unchanged. However, as long as the power law is not inserted for η, and the viscosity is not assumed constant and taken outside any derivatives, the form of the equation of motion and the stress balance components should not change. Then, in the r and z-components of the equation of motion for Newtonian fluid (Eqs. 31 and 32), the Newtonian viscosity can simply be replaced with the Non-Newtonian one. This yields:

$$\rho\left[\frac{\partial v_r}{\partial t}+\frac{1}{r}\frac{\partial}{\partial r}(rv_rv_r)+\frac{\partial}{\partial z}(v_zv_r)\right]=-\frac{\partial P}{\partial r}+\frac{1}{r}\frac{\partial}{\partial r}\left(2\eta r\frac{\partial v_r}{\partial r}\right)-2\eta\frac{v_r}{r^2}+\frac{\partial}{\partial z}\left[\eta\left(\frac{\partial v_z}{\partial r}+\frac{\partial v_r}{\partial z}\right)\right] \tag{126}$$

and

$$\rho\left[\frac{\partial v_z}{\partial t}+\frac{1}{r}\frac{\partial}{\partial r}(rv_rv_z)+\frac{\partial}{\partial z}(v_zv_z)\right]=-\frac{\partial P}{\partial z}+\frac{\partial}{\partial r}\left[\eta\left(\frac{\partial v_z}{\partial r}+\frac{\partial v_r}{\partial z}\right)\right]+\frac{\partial}{\partial z}\left(2\eta\frac{\partial v_z}{\partial z}\right) \tag{127}$$

Moreover, by replacing the Newtonian viscosity with the non-Newtonian one in the stress balances presented in Eqs. 74 and 78, these equations can be written as:

$$P+\frac{\eta}{1+\frac{1}{4}\left(\frac{\partial h}{\partial r}\right)^2}\left[\frac{1}{2}\frac{\partial v_r}{\partial r}\left(\frac{\partial h}{\partial r}\right)^2-\frac{\partial v_z}{\partial r}\frac{\partial h}{\partial r}-\frac{\partial v_r}{\partial z}\frac{\partial h}{\partial r}+2\frac{\partial v_z}{\partial z}\right]=\frac{2\sigma}{R_p}-\frac{1}{2r}\frac{\partial}{\partial r}\left(r\frac{\partial h}{\partial r}\right)\sigma, \tag{128}$$

and

$$-\frac{\eta}{1+\frac{1}{4}\left(\frac{\partial h}{\partial r}\right)^2}\left\{-\frac{\partial v_r}{\partial r}\frac{\partial h}{\partial r}+\left[1-\frac{1}{4}\left(\frac{\partial h}{\partial r}\right)^2\right]\left(\frac{\partial v_z}{\partial r}+\frac{\partial v_r}{\partial z}\right)+\frac{\partial v_z}{\partial z}\frac{\partial h}{\partial r}\right\}-\tau_d=0 \tag{129}$$

The non-Newtonian model can be simplified by making the equations dimensionless, as done for the Newtonian model. Characteristic scales is employed on the form:

$$\bar{p}=\frac{\sigma}{R_p},\quad \bar{h}=\varepsilon^2R_p,\quad \bar{r}=\varepsilon R_p,\quad \bar{v_r}=\frac{\varepsilon^3\sigma}{\eta_0},\quad \bar{v_z}=\frac{\varepsilon^4\sigma}{\eta_0},\quad \bar{t}=\frac{R_p\eta_0}{\varepsilon^2\sigma},\quad \bar{\tau_d}=\frac{\varepsilon\sigma}{R_p} \tag{130}$$

Notice that these scales are equivalent to the Newtonian characteristic scales in Eq. 80, except here, the Newtonian viscosity coefficient μ_c is replaced with a constant non-Newtonian coefficient, η_0. The following variable substitution is employed for the non-Newtonian viscosity.

$$\eta=\eta_0\tilde{\eta} \tag{131}$$

The characteristic scale, η_0, can be found by non-dimensionalizing the power law given in Eq. 123, which yields:

$$\eta_0\tilde{\eta}=m\left(\frac{\bar{v_r}}{\bar{h}}\right)^{n-1}\left|\frac{\partial\tilde{v_r}}{\partial\tilde{z}}\right|^{n-1} \tag{132}$$

This gives the following expression for η_0:

$$\eta_0 = m\left(\frac{\bar{v}_r}{\bar{h}}\right)^{n-1} \tag{133}$$

By inserting the characteristic scales for $\bar{v}_r$ and $\bar{h}$, Eq. 133 is rewritten to:

$$\eta_0 = m\left(\frac{\varepsilon\sigma}{\eta_0 R_p}\right)^{n-1} \tag{134}$$

Further rearranging yields:

$$\eta_0 = m^{\frac{1}{n}}\left(\frac{\varepsilon\sigma}{R_p}\right)^{1-\frac{1}{n}} \tag{135}$$

Thus, the dimensionless power law can be written as:

$$\tilde{\eta} = \left|\frac{\partial \tilde{v}_r}{\partial \tilde{z}}\right|^{n-1} \tag{136}$$

Non-dimensionalizing the r-component of the equation of motion in Eq. 126 by use of the characteristic scales given in Eq. 130 yields:

$$\begin{aligned}\rho\frac{\varepsilon^5\sigma^2}{\eta_0^2}\left[\frac{\partial \tilde{v}_r}{\partial \tilde{t}} + \frac{1}{\tilde{r}}\frac{\partial}{\partial \tilde{r}}(\tilde{r}\tilde{v}_r\tilde{v}_r) + \frac{\partial}{\partial \tilde{z}}(\tilde{v}_z\tilde{v}_r)\right] = &-\frac{\sigma}{\varepsilon R_p^2}\frac{\partial \tilde{P}}{\partial \tilde{r}} + \frac{\varepsilon\sigma}{R_p^2}\frac{1}{\tilde{r}}\frac{\partial}{\partial \tilde{r}}\left(2\tilde{\eta}r\frac{\partial \tilde{v}_r}{\partial \tilde{r}}\right) - 2\frac{\varepsilon\sigma}{R_p^2}\tilde{\eta}\frac{\tilde{v}_r}{\tilde{r}^2} \\ &+ \frac{\partial}{\partial \tilde{z}}\left[\tilde{\eta}\left(\frac{\varepsilon\sigma}{R_p^2}\frac{\partial \tilde{v}_z}{\partial \tilde{r}} + \frac{\sigma}{\varepsilon R_p^2}\frac{\partial \tilde{v}_r}{\partial \tilde{z}}\right)\right]\end{aligned} \tag{137}$$

By dividing with the coefficient, $\frac{\sigma}{\varepsilon R_p^2}$, Eq. 137 is made dimensionless:

$$\begin{aligned}\rho\frac{\varepsilon^6\sigma R_p^2}{\eta_0^2}\left[\frac{\partial \tilde{v}_r}{\partial \tilde{t}} + \frac{1}{\tilde{r}}\frac{\partial}{\partial \tilde{r}}(\tilde{r}\tilde{v}_r\tilde{v}_r) + \frac{\partial}{\partial \tilde{z}}(\tilde{v}_z\tilde{v}_r)\right] = &\frac{\partial \tilde{P}}{\partial \tilde{r}} + \varepsilon^2\frac{1}{\tilde{r}}\frac{\partial}{\partial \tilde{r}}\left(2\tilde{\eta}r\frac{\partial \tilde{v}_r}{\partial \tilde{r}}\right) - 2\varepsilon^2\tilde{\eta}\frac{\tilde{v}_r}{\tilde{r}^2} \\ &+ \frac{\partial}{\partial \tilde{z}}\left[\tilde{\eta}\left(\varepsilon\frac{\partial \tilde{v}_z}{\partial \tilde{r}} + \frac{\partial \tilde{v}_r}{\partial \tilde{z}}\right)\right]\end{aligned} \tag{138}$$

Here, it is determined that the terms which include ε in the numerator are much smaller than the others and can therefore be neglected. The non-Newtonian dimensionless radial component of the equation of motion can then be written as:

$$\frac{\partial \tilde{P}}{\partial \tilde{r}} = \frac{\partial}{\partial \tilde{z}}\left(\tilde{\eta}\frac{\partial \tilde{v}_r}{\partial \tilde{z}}\right) \tag{139}$$

Inserting the dimensionless power law from Eq. 136 gives:

$$\frac{\partial \tilde{P}}{\partial \tilde{r}} = \frac{\partial}{\partial \tilde{z}} \left(\left| \frac{\partial \tilde{v}_r}{\partial \tilde{z}} \right|^{n-1} \frac{\partial \tilde{v}_r}{\partial \tilde{z}} \right) \tag{140}$$

Non-dimensionalizing the z-component of the equation of motion yields:

$$\begin{aligned} \rho \frac{\varepsilon^6 \sigma^2}{\eta_0^2 R_p} \left[\frac{\partial \tilde{v}_z}{\partial \tilde{t}} + \frac{1}{\tilde{r}} \frac{\partial}{\partial \tilde{r}} (\tilde{r} \tilde{v}_r \tilde{v}_z) + \frac{\partial}{\partial \tilde{z}} (\tilde{v}_z \tilde{v}_z) \right] = & - \frac{\sigma}{\varepsilon^2 R_p^2} \frac{\partial \tilde{P}}{\partial \tilde{z}} + \frac{\varepsilon^2 \sigma}{R_p^2} \frac{\partial}{\partial \tilde{r}} \left[\tilde{\eta} \left(\frac{\partial \tilde{v}_z}{\partial \tilde{r}} + \frac{\partial \tilde{v}_r}{\partial \tilde{z}} \right) \right] \\ & + \frac{\sigma}{R_p^2} \frac{\partial}{\partial \tilde{z}} \left(2 \tilde{\eta} \frac{\partial \tilde{v}_z}{\partial \tilde{z}} \right) \end{aligned} \tag{141}$$

Eq. 141 is further divided by the coefficient, $\frac{\sigma}{\varepsilon^2 R_p^2}$ to remove the dimensions. This results in:

$$\begin{aligned} \rho \frac{\varepsilon^8 \sigma R_p}{\eta_0^2} \left[\frac{\partial \tilde{v}_z}{\partial \tilde{t}} + \frac{1}{\tilde{r}} \frac{\partial}{\partial \tilde{r}} (\tilde{r} \tilde{v}_r \tilde{v}_z) + \frac{\partial}{\partial \tilde{z}} (\tilde{v}_z \tilde{v}_z) \right] = & - \frac{\partial \tilde{P}}{\partial \tilde{z}} + \varepsilon^4 \frac{\partial}{\partial \tilde{r}} \left[\tilde{\eta} \left(\frac{\partial \tilde{v}_z}{\partial \tilde{r}} + \frac{\partial \tilde{v}_r}{\partial \tilde{z}} \right) \right] \\ & + \varepsilon \frac{\partial}{\partial \tilde{z}} \left(2 \tilde{\eta} \frac{\partial \tilde{v}_z}{\partial \tilde{z}} \right) \end{aligned} \tag{142}$$

The pressure term is determined to be much more significant than the other terms, thus Eq. 142 simplifies to:

$$\frac{\partial \tilde{P}}{\partial \tilde{z}} = 0 \tag{143}$$

Moreover, non-dimensionalizing the normal component of the stress balance results in:

$$\begin{aligned} & \frac{\sigma}{R_p} \tilde{P} + \frac{\tilde{\eta}}{1 + \frac{1}{4} \varepsilon^2 \left(\frac{\partial \tilde{h}}{\partial \tilde{r}} \right)^2} \left[\frac{1}{2} \frac{\varepsilon^3 \sigma}{R_p} \frac{\partial \tilde{v}_r}{\partial \tilde{r}} \left(\frac{\partial \tilde{h}}{\partial \tilde{r}} \right)^2 - \frac{\varepsilon^4 \sigma}{R_p} \frac{\partial \tilde{v}_z}{\partial \tilde{r}} \frac{\partial \tilde{h}}{\partial \tilde{r}} - \frac{\varepsilon^2 \sigma}{R_p} \frac{\partial \tilde{v}_r}{\partial \tilde{z}} \frac{\partial \tilde{h}}{\partial \tilde{r}} + 2 \frac{\varepsilon^2 \sigma}{R_p} \frac{\partial \tilde{v}_z}{\partial \tilde{z}} \right] \\ & = \frac{2\sigma}{R_p} - \frac{1}{R_p} \frac{1}{2\tilde{r}} \frac{\partial}{\partial \tilde{r}} \left(\tilde{r} \frac{\partial \tilde{h}}{\partial \tilde{r}} \right) \sigma, \end{aligned} \tag{144}$$

Equation 144 can further be divided by the coefficient on the right-hand side, $\frac{\sigma}{R_p}$, which yields:

$$\begin{aligned} & \tilde{P} + \frac{\tilde{\eta}}{1 + \frac{1}{4} \varepsilon^2 \left(\frac{\partial \tilde{h}}{\partial \tilde{r}} \right)^2} \left[\frac{1}{2} \varepsilon^3 \frac{\partial \tilde{v}_r}{\partial \tilde{r}} \left(\frac{\partial \tilde{h}}{\partial \tilde{r}} \right)^2 - \varepsilon^4 \frac{\partial \tilde{v}_z}{\partial \tilde{r}} \frac{\partial \tilde{h}}{\partial \tilde{r}} - \varepsilon^2 \frac{\partial \tilde{v}_r}{\partial \tilde{z}} \frac{\partial \tilde{h}}{\partial \tilde{r}} + 2 \varepsilon^2 \frac{\partial \tilde{v}_z}{\partial \tilde{z}} \right] \\ & = 2 - \frac{1}{2\tilde{r}} \frac{\partial}{\partial \tilde{r}} \left(\tilde{r} \frac{\partial \tilde{h}}{\partial \tilde{r}} \right), \end{aligned} \tag{145}$$

Here, the viscous terms are negligible compared to the pressure term and the curvature term. Hence, the dimensionless normal stress balance simplifies to:

$$\tilde{P} = 2 - \frac{1}{2\tilde{r}} \frac{\partial}{\partial \tilde{r}} \left(\tilde{r} \frac{\partial \tilde{h}}{\partial \tilde{r}} \right), \tag{146}$$

Furthermore, non-dimensionalizing the tangential stress balance yields:

$$-\frac{\tilde{\eta}}{1+\frac{1}{4}\varepsilon^2\left(\frac{\partial\tilde{h}}{\partial\tilde{r}}\right)^2}\left\{-\frac{\varepsilon^3\sigma}{R_p}\frac{\partial\tilde{v_r}}{\partial\tilde{r}}\frac{\partial\tilde{h}}{\partial\tilde{r}}+\left[1-\varepsilon^2\frac{1}{4}\left(\frac{\partial\tilde{h}}{\partial\tilde{r}}\right)^2\right]\left(\frac{\varepsilon^3\sigma}{R_p}\frac{\partial\tilde{v_z}}{\partial\tilde{r}}+\frac{\varepsilon\sigma}{R_p}\frac{\partial\tilde{v_r}}{\partial\tilde{z}}\right)+\frac{\varepsilon^3\sigma}{R_p}\frac{\partial\tilde{v_z}}{\partial\tilde{z}}\frac{\partial\tilde{h}}{\partial\tilde{r}}\right\}$$
$$-\frac{\varepsilon\sigma}{R_p}\tilde{\tau}_d=0 \tag{147}$$

Dividing by the particle side tangential stress coefficient, $\frac{\varepsilon\sigma}{R_p}$ gives:

$$-\frac{\tilde{\eta}}{1+\frac{1}{4}\varepsilon^2\left(\frac{\partial\tilde{h}}{\partial\tilde{r}}\right)^2}\left\{-\varepsilon^2\frac{\partial\tilde{v_r}}{\partial\tilde{r}}\frac{\partial\tilde{h}}{\partial\tilde{r}}+\left[1-\varepsilon^2\frac{1}{4}\left(\frac{\partial\tilde{h}}{\partial\tilde{r}}\right)^2\right]\left(\varepsilon^2\frac{\partial\tilde{v_z}}{\partial\tilde{r}}+\frac{\partial\tilde{v_r}}{\partial\tilde{z}}\right)+\varepsilon^2\frac{\partial\tilde{v_z}}{\partial\tilde{z}}\frac{\partial\tilde{h}}{\partial\tilde{r}}\right\} \tag{148}$$
$$-\tilde{\tau}_d=0$$

By comparing the magnitude of all the terms, it is determined that the terms which include ε are negligible compared to the rest. Thus, the tangential dimensionless stress balance simplifies to:

$$-\tilde{\eta}\frac{\partial\tilde{v_r}}{\partial\tilde{z}}=\tilde{\tau}_d \tag{149}$$

Inserting the dimensionless power law expression given in Eq. 136 yields:

$$-\left|\frac{\partial\tilde{v_r}}{\partial\tilde{z}}\right|^{n-1}\frac{\partial\tilde{v_r}}{\partial\tilde{z}}=\tilde{\tau}_d \tag{150}$$

Note that the dimensionless z-component of the equation of motion and the normal stress balance for the non-Newtonian continuous phase are identical to the corresponding equations valid for a Newtonian fluid. However, the dimensionless tangential stress balance and the r-component of the equation of motion are affected by the non-Newtonian viscosity, introducing the absolute value into the equations. As the velocity decreases from the center to the interface, the top half of the thin film where the z-coordinates are positive gives $\frac{\partial\tilde{v_r}}{\partial\tilde{z}}<0$. Correspondingly, the lower half of the thin film where the z-coordinates are negative, is described by $\frac{\partial\tilde{v_r}}{\partial\tilde{z}}>0$. Although we only obtain the solution for $z\geq 0$, both signs will be further investigated to control that the same equations can be solved for the upper and lower part of the film, as given by the assumption of symmetry around the radial axis. For $z\geq 0$, the equation of motion given in Eq. 140 can be expressed as:

$$\frac{\partial\tilde{P}}{\partial\tilde{r}}=\frac{\partial}{\partial\tilde{z}}\left[\left(-\frac{\partial\tilde{v_r}}{\partial\tilde{z}}\right)^{n-1}\frac{\partial\tilde{v_r}}{\partial\tilde{z}}\right]=-\frac{\partial}{\partial\tilde{z}}\left(-\frac{\partial\tilde{v_r}}{\partial\tilde{z}}\right)^n \tag{151}$$

Whereas for $z\leq 0$, Eq. 140 becomes:

$$\frac{\partial\tilde{P}}{\partial\tilde{r}}=\frac{\partial}{\partial\tilde{z}}\left[\left(\frac{\partial\tilde{v_r}}{\partial\tilde{z}}\right)^{n-1}\frac{\partial\tilde{v_r}}{\partial\tilde{z}}\right]=\frac{\partial}{\partial\tilde{z}}\left(\frac{\partial\tilde{v_r}}{\partial\tilde{z}}\right)^n \tag{152}$$

First, we will concentrate on the upper half of of the film, where an expression for $\tilde{v_r}$ can be derived by integrating Eq. 151 with respect to $\tilde{z}$:

$$\left(\frac{\partial \tilde{P}}{\partial \tilde{r}}\right)\tilde{z} = -\left(-\frac{\partial \tilde{v_r}}{\partial \tilde{z}}\right)^n + C_1 \tag{153}$$

Due to the assumption of symmetry around the radial axis, the following boundary condition is applied.

$$\frac{\partial \tilde{v_r}}{\partial \tilde{z}} \mid_{z=0} = 0 \tag{154}$$

This gives: $C_1 = 0$.

Equation 153 is further rearranged to:

$$-\left(-\frac{\partial \tilde{P}}{\partial \tilde{r}}\right)^{1/n} \tilde{z}^{1/n} = \frac{\partial \tilde{v_r}}{\partial \tilde{z}} \tag{155}$$

Integrating with respect to z to gives:

$$-\frac{1}{\frac{1}{n}+1}\left(-\frac{\partial \tilde{P}}{\partial \tilde{r}}\right)^{1/n} \tilde{z}^{\frac{1}{n}+1} + C_2 = \tilde{v_r} \tag{156}$$

Now the no-slip condition (see Eq. 115) can be applied, which gives the following boundary condition.

$$\tilde{v_r} \mid_{\tilde{z}=h/2} = \tilde{U_t}. \tag{157}$$

Hence, $\tilde{v_r}$ is written as:

$$\tilde{v_r} = \tilde{U_t} + \frac{1}{\frac{1}{n}+1}\left(-\frac{\partial \tilde{P}}{\partial \tilde{r}}\right)^{1/n}\left[\left(\frac{h}{2}\right)^{\frac{1}{n}+1} - \tilde{z}^{\frac{1}{n}+1}\right] \tag{158}$$

Moreover, the velocity, $\tilde{v_r}$ is inserted into the dimensionless continuity equation shown in Eq. 86. This yields:

$$\frac{1}{\tilde{r}}\frac{\partial}{\partial \tilde{r}}\left(\tilde{r}\left\{\tilde{U_t} + \frac{1}{\frac{1}{n}+1}\left(-\frac{\partial \tilde{P}}{\partial \tilde{r}}\right)^{1/n}\left[\left(\frac{h}{2}\right)^{\frac{1}{n}+1} - \tilde{z}^{\frac{1}{n}+1}\right]\right\}\right) + \frac{\partial \tilde{v}_z}{\partial \tilde{z}} = 0 \tag{159}$$

By integrating with respect to $\tilde{z}$, an expression for $\tilde{v_z}$ can be obtained on the form:

$$\begin{aligned} v_z = &-\frac{1}{\tilde{r}}(\tilde{r}\tilde{U_t})\tilde{z} - \frac{1}{\tilde{r}}\frac{\partial}{\partial \tilde{r}}\left[\tilde{r}\frac{1}{\frac{1}{n}+1}\left(-\frac{\partial \tilde{P}}{\partial \tilde{r}}\right)^{1/n}\left(\frac{h}{2}\right)^{\frac{1}{n}+1}\right]z \\ &+ \frac{1}{\tilde{r}}\frac{\partial}{\partial \tilde{r}}\left[\tilde{r}\frac{1}{\frac{1}{n}+1}\left(-\frac{\partial \tilde{P}}{\partial \tilde{r}}\right)^{1/n}\right]\frac{1}{\frac{1}{n}+2}\tilde{z}^{\frac{1}{n}+2} + C_3 \end{aligned} \tag{160}$$

Due to symmetry around the radial axis, an additional boundary condition appears:

$$\tilde{v_z}\mid_{z=0}=0. \tag{161}$$

This results in $C_3 = 0$.

Furthermore, the obtained expression for v_r and v_z in Eq. 158 and 160 respectively, can be inserted into the dimensionless kinematic condition given in Eq. 91. This yields:

$$\begin{aligned}\frac{1}{2}\frac{\partial\tilde{h}}{\partial\tilde{t}} =& -\frac{1}{\tilde{r}}\frac{\partial}{\partial\tilde{r}}(\tilde{r}\tilde{U_t})\frac{\tilde{h}}{2}-\frac{1}{\tilde{r}}\frac{\partial}{\partial\tilde{r}}\left[\tilde{r}\frac{1}{\frac{1}{n}+1}\left(-\frac{\partial\tilde{P}}{\partial\tilde{r}}\right)^{1/n}\left(\frac{\tilde{h}}{2}\right)^{\frac{1}{n}+1}\right]\frac{\tilde{h}}{2}\\ &+\frac{1}{\tilde{r}}\frac{\partial}{\partial\tilde{r}}\left[\tilde{r}\frac{1}{\frac{1}{n}+1}\left(-\frac{\partial\tilde{P}}{\partial\tilde{r}}\right)^{1/n}\right]\frac{1}{\frac{1}{n}+2}\left(\frac{\tilde{h}}{2}\right)^{\frac{1}{n}+2}\\ &-\frac{1}{2}\frac{\partial\tilde{h}}{\partial\tilde{r}}\left\{\tilde{U_t}+\frac{1}{\frac{1}{n}+1}\left(-\frac{\partial\tilde{P}}{\partial\tilde{r}}\right)^{1/n}\left[\left(\frac{\tilde{h}}{2}\right)^{\frac{1}{n}+1}-\left(\frac{\tilde{h}}{2}\right)^{\frac{1}{n}+1}\right]\right\}\end{aligned} \tag{162}$$

Note that since the kinematic condition is only valid at the interface, the axial coordinate is taken as $z = h/2$. Moreover, Eq. 162 can be reduced to:

$$\begin{aligned}\frac{1}{2}\frac{\partial\tilde{h}}{\partial\tilde{t}} =& -\frac{1}{\tilde{r}}\frac{\partial}{\partial\tilde{r}}(\tilde{r}\tilde{U_t})\frac{\tilde{h}}{2}-\frac{1}{\tilde{r}}\frac{\partial}{\partial\tilde{r}}\left[\tilde{r}\frac{1}{\frac{1}{n}+1}\left(-\frac{\partial\tilde{P}}{\partial\tilde{r}}\right)^{1/n}\left(\frac{\tilde{h}}{2}\right)^{\frac{1}{n}+1}\right]\frac{\tilde{h}}{2}\\ &+\frac{1}{\tilde{r}}\frac{\partial}{\partial\tilde{r}}\left[\tilde{r}\frac{1}{\frac{1}{n}+1}\left(-\frac{\partial\tilde{P}}{\partial\tilde{r}}\right)^{1/n}\right]\frac{1}{\frac{1}{n}+2}\left(\frac{\tilde{h}}{2}\right)^{\frac{1}{n}+2}-\frac{1}{2}\frac{\partial\tilde{h}}{\partial\tilde{r}}\tilde{U_t}\end{aligned} \tag{163}$$

The same procedure is now repeated for the lower half of the film where the z-coordinates are negative. Integrating Eq. 152 with respect to z yields:

$$\left(\frac{\partial\tilde{P}}{\partial\tilde{r}}\right)\tilde{z}=\left(\frac{\partial\tilde{v_r}}{\partial\tilde{z}}\right)^n+C_4 \tag{164}$$

As mention earlier, the assumption of symmetry around the radial axis gives rise to the following boundary condition:

$$\frac{\partial\tilde{v_r}}{\partial\tilde{z}}\mid_{z=0}=0, \tag{165}$$

which is inserted into Eq. 164. It follows that $C_4 = 0$.

With a little rearranging, Eq. 164 can be rewritten as:

$$\frac{\partial\tilde{v_r}}{\partial\tilde{z}}=\left(\frac{\partial\tilde{P}}{\partial\tilde{r}}\right)^{1/n}\tilde{z}^{1/n} \tag{166}$$

Further integration with respect to $\tilde{z}$ yields:

$$\tilde{v_r} = \frac{1}{\frac{1}{n}+1}\left(\frac{\partial \tilde{P}}{\partial \tilde{r}}\right)^{1/n} \tilde{z}^{\frac{1}{n}+1} + C_5 \tag{167}$$

The no-slip condition is employed as boundary condition:

$$\tilde{v_r}\mid_{\tilde{z}=-h/2} = \tilde{U_t}. \tag{168}$$

which yields the following expression for $\tilde{v_r}$:

$$\tilde{v_r} = \tilde{U_t} - \frac{1}{\frac{1}{n}+1}\left(\frac{\partial \tilde{P}}{\partial \tilde{r}}\right)^{1/n}\left[\tilde{z}^{\frac{1}{n}+1} - \left(-\frac{h}{2}\right)^{\frac{1}{n}+1}\right] \tag{169}$$

This expression can be inserted into the dimensionless continuity equation given in Eq. 86, which results in:

$$\frac{1}{\tilde{r}}\frac{\partial}{\partial \tilde{r}}\left\{\tilde{r}\left(\tilde{U_t} - \frac{1}{\frac{1}{n}+1}\left(\frac{\partial \tilde{P}}{\partial \tilde{r}}\right)^{1/n}\left[\tilde{z}^{\frac{1}{n}+1} - \left(-\frac{h}{2}\right)^{\frac{1}{n}+1}\right]\right)\right\} + \frac{\partial \tilde{v}_z}{\partial \tilde{z}} = 0 \tag{170}$$

By integrating with respect to $\tilde{z}$, the following expression is obtained for $\tilde{v_z}$:

$$\begin{aligned} v_z = &-\frac{1}{\tilde{r}}(\tilde{r}\tilde{U_t})\tilde{z} + \frac{1}{\tilde{r}}\frac{\partial}{\partial \tilde{r}}\left\{\tilde{r}\frac{1}{\frac{1}{n}+1}\left(\frac{\partial \tilde{P}}{\partial \tilde{r}}\right)^{1/n}\left(-\frac{h}{2}\right)^{\frac{1}{n}+1}\right\}\tilde{z} \\ &-\frac{1}{\tilde{r}}\frac{\partial}{\partial \tilde{r}}\left\{\tilde{r}\frac{1}{\frac{1}{n}+1}\left(\frac{\partial \tilde{P}}{\partial \tilde{r}}\right)^{1/n}\right\}\frac{1}{\frac{1}{n}+2}\tilde{z}^{\frac{1}{n}+2} + C_6 \end{aligned} \tag{171}$$

Applying the assumption of symmetry around the radial axis gives the boundary condition:

$$\tilde{v_z}\mid_{z=0} = 0, \tag{172}$$

which results in: $C_6 = 0$.

For the lower half of the film, the interface is described by $z = -h/2$. This means that the terms which include $\tilde{h}$ in the kinematic condition given in Eq. 91 changes sign, which yields:

$$-\frac{1}{2}\frac{\partial \tilde{h}}{\partial \tilde{t}} = \tilde{v}_z + \frac{1}{2}\frac{\partial \tilde{h}}{\partial \tilde{r}}\tilde{v}_r \tag{173}$$

Inserting the obtained expressions for $\tilde{v_r}$ and $\tilde{v_z}$ results in:

$$
\begin{aligned}
-\frac{1}{2}\frac{\partial \tilde{h}}{\partial \tilde{t}} =& \frac{1}{\tilde{r}}(\tilde{r}\tilde{U}_t)\frac{\tilde{h}}{2} - \frac{1}{\tilde{r}}\frac{\partial}{\partial \tilde{r}}\left[\tilde{r}\frac{1}{\frac{1}{n}+1}\left(\frac{\partial \tilde{P}}{\partial \tilde{r}}\right)^{1/n}\left(-\frac{\tilde{h}}{2}\right)^{\frac{1}{n}+1}\right]\frac{\tilde{h}}{2} \\
&- \frac{1}{\tilde{r}}\frac{\partial}{\partial \tilde{r}}\left[\tilde{r}\frac{1}{\frac{1}{n}+1}\left(\frac{\partial \tilde{P}}{\partial \tilde{r}}\right)^{1/n}\right]\frac{1}{\frac{1}{n}+2}\left(-\frac{\tilde{h}}{2}\right)^{\frac{1}{n}+2} \\
&+ \frac{1}{2}\frac{\partial \tilde{h}}{\partial \tilde{r}}\frac{1}{\frac{1}{n}+1}\left(\frac{\partial \tilde{P}}{\partial \tilde{r}}\right)^{1/n}\left[\left(-\frac{\tilde{h}}{2}\right)^{\frac{1}{n}+1} - \left(-\frac{\tilde{h}}{2}\right)^{\frac{1}{n}+1}\right] \\
&+ \frac{1}{2}\frac{\partial \tilde{h}}{\partial \tilde{r}}\left\{\tilde{U}_t - \frac{1}{\frac{1}{n}+1}\left(\frac{\partial \tilde{P}}{\partial \tilde{r}}\right)^{1/n}\left[\left(\frac{\tilde{h}}{2}\right)^{\frac{1}{n}+1} - \left(\frac{\tilde{h}}{2}\right)^{\frac{1}{n}+1}\right]\right\}
\end{aligned}
\tag{174}
$$

which can be reduced to:

$$
\begin{aligned}
-\frac{1}{2}\frac{\partial \tilde{h}}{\partial \tilde{t}} =& \frac{1}{\tilde{r}}(\tilde{r}\tilde{U}_t)\frac{\tilde{h}}{2} - \frac{1}{\tilde{r}}\frac{\partial}{\partial \tilde{r}}\left[\tilde{r}\frac{1}{\frac{1}{n}+1}\left(\frac{\partial \tilde{P}}{\partial \tilde{r}}\right)^{1/n}\left(-\frac{\tilde{h}}{2}\right)^{\frac{1}{n}+1}\right]\frac{\tilde{h}}{2} \\
&- \frac{1}{\tilde{r}}\frac{\partial}{\partial \tilde{r}}\left[\tilde{r}\frac{1}{\frac{1}{n}+1}\left(\frac{\partial \tilde{P}}{\partial \tilde{r}}\right)^{1/n}\right]\frac{1}{\frac{1}{n}+2}\left(-\frac{\tilde{h}}{2}\right)^{\frac{1}{n}+2} + \frac{1}{2}\frac{\partial \tilde{h}}{\partial \tilde{r}}\tilde{U}_t
\end{aligned}
\tag{175}
$$

If the assumption of symmetry around the radial axis holds, it should be possible to express Eqs. 175 and 163 on the same form. For easier comparison of the equations, they are rewritten for the upper and lower half of the film respectively as:

$$
\begin{aligned}
\frac{1}{2}\frac{\partial \tilde{h}}{\partial \tilde{t}} =& -\frac{1}{\tilde{r}}\frac{\partial}{\partial \tilde{r}}(\tilde{r}\tilde{U}_t)\frac{\tilde{h}}{2} - (-1)^{1/n}\frac{1}{\tilde{r}}\frac{\partial}{\partial \tilde{r}}\left[\tilde{r}\frac{1}{\frac{1}{n}+1}\left(\frac{\partial \tilde{P}}{\partial \tilde{r}}\right)^{1/n}\left(\frac{\tilde{h}}{2}\right)^{\frac{1}{n}+1}\right]\frac{\tilde{h}}{2} \\
&+ (-1)^{1/n}\frac{1}{\tilde{r}}\frac{\partial}{\partial \tilde{r}}\left[\tilde{r}\frac{1}{\frac{1}{n}+1}\left(\frac{\partial \tilde{P}}{\partial \tilde{r}}\right)^{1/n}\right]\frac{1}{\frac{1}{n}+2}\left(\frac{\tilde{h}}{2}\right)^{\frac{1}{n}+2} - \frac{1}{2}\frac{\partial \tilde{h}}{\partial \tilde{r}}\tilde{U}_t
\end{aligned}
\tag{176}
$$

and:

$$
\begin{aligned}
-\frac{1}{2}\frac{\partial \tilde{h}}{\partial \tilde{t}} =& \frac{1}{\tilde{r}}\frac{\partial}{\partial \tilde{r}}(\tilde{r}\tilde{U}_t)\frac{\tilde{h}}{2} - (-1)^{\frac{1}{n}+1}\frac{1}{\tilde{r}}\frac{\partial}{\partial \tilde{r}}\left[\tilde{r}\frac{1}{\frac{1}{n}+1}\left(\frac{\partial \tilde{P}}{\partial \tilde{r}}\right)^{1/n}\left(\frac{\tilde{h}}{2}\right)^{\frac{1}{n}+1}\right]\frac{\tilde{h}}{2} \\
&- (-1)^{\frac{1}{n}+2}\frac{1}{\tilde{r}}\frac{\partial}{\partial \tilde{r}}\left[\tilde{r}\frac{1}{\frac{1}{n}+1}\left(\frac{\partial \tilde{P}}{\partial \tilde{r}}\right)^{1/n}\right]\frac{1}{\frac{1}{n}+2}\left(\frac{\tilde{h}}{2}\right)^{\frac{1}{n}+2} + \frac{1}{2}\frac{\partial \tilde{h}}{\partial \tilde{r}}\tilde{U}_t
\end{aligned}
\tag{177}
$$

To make the left hand side of Eqs. 176 and 177 equal, Eq. 177 is multiplied with (-1), which gives:

$$\begin{aligned}\frac{1}{2}\frac{\partial \tilde{h}}{\partial \tilde{t}} =& -\frac{1}{\tilde{r}}\frac{\partial}{\partial \tilde{r}}(\tilde{r}\tilde{U}_t)\frac{\tilde{h}}{2} - (-1)^{\frac{1}{n}+2}\frac{1}{\tilde{r}}\frac{\partial}{\partial \tilde{r}}\left[\tilde{r}\frac{1}{\frac{1}{n}+1}\left(\frac{\partial \tilde{P}}{\partial \tilde{r}}\right)^{1/n}\left(\frac{\tilde{h}}{2}\right)^{\frac{1}{n}+1}\right]\frac{\tilde{h}}{2} \\ &+ (-1)^{\frac{1}{n}+2}\frac{1}{\tilde{r}}\frac{\partial}{\partial \tilde{r}}\left[\tilde{r}\frac{1}{\frac{1}{n}+1}\left(\frac{\partial \tilde{P}}{\partial \tilde{r}}\right)^{1/n}\right]\frac{1}{\frac{1}{n}+2}\left(\frac{\tilde{h}}{2}\right)^{\frac{1}{n}+2} - \frac{1}{2}\frac{\partial \tilde{h}}{\partial \tilde{r}}\tilde{U}_t\end{aligned} \tag{178}$$

The terms in Eqs. 176 and 178 can now be compared by applying the relation: $(-1)^{\frac{1}{n}+2} = (-1)^2(-1)^{\frac{1}{n}} = (-1)^{\frac{1}{n}}$. It is then observed that the kinematic condition can be written in the same form for both the upper and lower half of the film. Thus, the assumption of symmetry around the radial axis holds, and only the equation describing the part of the film with positive z-coordinates is manipulated further.

The last term in Eq. 163 is taken as:

$$-\frac{1}{2}\frac{\partial \tilde{h}}{\partial \tilde{r}}\tilde{U}_t = -\frac{1}{r}\frac{\partial}{\partial \tilde{r}}\left(\frac{\tilde{h}}{2}\right)\tilde{r}\tilde{U}_t \tag{179}$$

Then, by using the product rule (A.15) in reverse, the first and last terms on the right-hand side in Eq. 163 can be combined:

$$-\frac{1}{\tilde{r}}\frac{\partial}{\partial \tilde{r}}(\tilde{r}\tilde{U}_t)\frac{\tilde{h}}{2} - \frac{1}{r}\frac{\partial}{\partial \tilde{r}}\left(\frac{\tilde{h}}{2}\right)\tilde{r}\tilde{U}_t = -\frac{1}{\tilde{r}}\frac{\partial}{\partial \tilde{r}}\left(\tilde{r}\tilde{U}_t\frac{\tilde{h}}{2}\right) \tag{180}$$

For the next part of the derivation, we will focus on manipulating the second and third terms on the right-hand side in Eq. 163. By further use of the product rule (A.15) on these terms, Eq. 163 can be rearranged to:

$$\begin{aligned}\frac{1}{2}\frac{\partial \tilde{h}}{\partial \tilde{t}} =& -\frac{1}{\tilde{r}}\frac{\partial}{\partial \tilde{r}}\left(\tilde{r}\tilde{U}_t\frac{\tilde{h}}{2}\right) - \frac{1}{\tilde{r}}\frac{\partial}{\partial \tilde{r}}\left\{\tilde{r}\frac{1}{\frac{1}{n}+1}\left(-\frac{\partial \tilde{P}}{\partial \tilde{r}}\right)^{1/n}\right\}\left[\left(\frac{\tilde{h}}{2}\right)^{\frac{1}{n}+2} - \frac{1}{\frac{1}{n}+2}\left(\frac{\tilde{h}}{2}\right)^{\frac{1}{n}+2}\right] \\ &- \frac{1}{\tilde{r}}\frac{\partial}{\partial \tilde{r}}\left[\left(\frac{\tilde{h}}{2}\right)^{\frac{1}{n}+1}\right]\tilde{r}\frac{1}{\frac{1}{n}+1}\left(-\frac{\partial \tilde{P}}{\partial \tilde{r}}\right)^{1/n}\left(\frac{\tilde{h}}{2}\right)\end{aligned} \tag{181}$$

Furthermore, the chain rule (Eq. A.16) is employed to express the following relation:

$$\frac{\partial}{\partial \tilde{r}}\left[\left(\frac{\tilde{h}}{2}\right)^{\frac{1}{n}+1}\right] = \left(\frac{1}{n}+1\right)\frac{\partial}{\partial \tilde{r}}\left\{\frac{\tilde{h}}{2}\right\}\left(\frac{\tilde{h}}{2}\right)^{\frac{1}{n}} \tag{182}$$

Hence, Eq. 181 can now be written as:

$$\frac{1}{2}\frac{\partial \tilde{h}}{\partial \tilde{t}} = -\frac{1}{\tilde{r}}\frac{\partial}{\partial \tilde{r}}\left(\tilde{r}\tilde{U}_t\frac{\tilde{h}}{2}\right) - \frac{1}{\tilde{r}}\frac{\partial}{\partial \tilde{r}}\left\{\tilde{r}\frac{1}{\frac{1}{n}+1}\left(-\frac{\partial \tilde{P}}{\partial \tilde{r}}\right)^{1/n}\right\}\left(\frac{\tilde{h}}{2}\right)^{\frac{1}{n}+2}\left[1-\frac{1}{\frac{1}{n}+2}\right] \\ -\frac{1}{\tilde{r}}\left(\frac{1}{n}+1\right)\left(\frac{\tilde{h}}{2}\right)^{\frac{1}{n}}\frac{\partial}{\partial \tilde{r}}\left(\frac{\tilde{h}}{2}\right)\tilde{r}\frac{1}{\frac{1}{n}+1}\left(-\frac{\partial \tilde{P}}{\partial \tilde{r}}\right)^{1/n}\frac{\tilde{h}}{2} \tag{183}$$

Further manipulation yields:

$$\frac{1}{2}\frac{\partial \tilde{h}}{\partial \tilde{t}} = -\frac{1}{\tilde{r}}\frac{\partial}{\partial \tilde{r}}\left(\tilde{r}\tilde{U}_t\frac{\tilde{h}}{2}\right) - \frac{1}{\tilde{r}}\frac{\partial}{\partial \tilde{r}}\left\{\tilde{r}\frac{1}{\frac{1}{n}+1}\left(-\frac{\partial \tilde{P}}{\partial \tilde{r}}\right)^{1/n}\right\}\left(\frac{\tilde{h}}{2}\right)^{\frac{1}{n}+2}\left[\frac{\frac{1}{n}+1}{\frac{1}{n}+2}\right] \\ -\left(\frac{1}{n}+1\right)\frac{1}{\tilde{r}}\left(\frac{\tilde{h}}{2}\right)^{\frac{1}{n}}\frac{\partial}{\partial \tilde{r}}\left(\frac{\tilde{h}}{2}\right)\tilde{r}\frac{1}{\frac{1}{n}+1}\left(-\frac{\partial \tilde{P}}{\partial \tilde{r}}\right)^{1/n}\frac{\tilde{h}}{2}, \tag{184}$$

Here, the second term on the right-hand side can be simplified, which gives:

$$\frac{1}{2}\frac{\partial \tilde{h}}{\partial \tilde{t}} = -\frac{1}{\tilde{r}}\frac{\partial}{\partial \tilde{r}}\left(\tilde{r}\tilde{U}_t\frac{\tilde{h}}{2}\right) - \frac{1}{\tilde{r}}\frac{\partial}{\partial \tilde{r}}\left\{\tilde{r}\left(-\frac{\partial \tilde{P}}{\partial \tilde{r}}\right)^{1/n}\right\}\left(\frac{\tilde{h}}{2}\right)^{\frac{1}{n}+2}\frac{1}{\frac{1}{n}+2} \\ -\frac{1}{\tilde{r}}\tilde{r}\left(-\frac{\partial \tilde{P}}{\partial \tilde{r}}\right)^{1/n}\left(\frac{\tilde{h}}{2}\right)^{\frac{1}{n}+1}\frac{\partial}{\partial \tilde{r}}\left(\frac{\tilde{h}}{2}\right) \tag{185}$$

By applying the chain rule in reverse, the following expression can be recovered:

$$\left(\frac{1}{n}+2\right)\frac{\partial}{\partial \tilde{r}}\left\{\frac{\tilde{h}}{2}\right\}\left(\frac{\tilde{h}}{2}\right)^{\frac{1}{n}+1} = \frac{\partial}{\partial \tilde{r}}\left[\left(\frac{\tilde{h}}{2}\right)^{\frac{1}{n}+2}\right] \tag{186}$$

Thus, Eq. 185 is rewritten as:

$$\frac{1}{2}\frac{\partial \tilde{h}}{\partial \tilde{t}} = -\frac{1}{\tilde{r}}\frac{\partial}{\partial \tilde{r}}\left(\tilde{r}\tilde{U}_t\frac{\tilde{h}}{2}\right) - \frac{1}{\tilde{r}}\frac{\partial}{\partial \tilde{r}}\left\{\tilde{r}\left(-\frac{\partial \tilde{P}}{\partial \tilde{r}}\right)^{1/n}\right\}\left(\frac{\tilde{h}}{2}\right)^{\frac{1}{n}+2}\frac{1}{\frac{1}{n}+2} \\ -\frac{1}{\tilde{r}}\tilde{r}\left(-\frac{\partial \tilde{P}}{\partial \tilde{r}}\right)^{1/n}\frac{\partial}{\partial \tilde{r}}\left[\left(\frac{\tilde{h}}{2}\right)^{\frac{1}{n}+2}\right]\frac{1}{\frac{1}{n}+2} \tag{187}$$

Then, employing the product rule in reverse yields:

$$\frac{1}{2}\frac{\partial \tilde{h}}{\partial \tilde{t}} = -\frac{1}{\tilde{r}}\frac{\partial}{\partial \tilde{r}}\left(\tilde{r}\tilde{U}_t\frac{\tilde{h}}{2}\right) - \frac{1}{\tilde{r}}\frac{\partial}{\partial \tilde{r}}\left\{\tilde{r}\left(-\frac{\partial \tilde{P}}{\partial \tilde{r}}\right)^{1/n}\left(\frac{\tilde{h}}{2}\right)^{\frac{1}{n}+2}\right\}\frac{1}{\frac{1}{n}+2} \tag{188}$$

Multiplying by 2 and further rearranging the second term on the right-hand side gives:

$$\frac{\partial \tilde{h}}{\partial \tilde{t}} = -\frac{1}{\tilde{r}}\frac{\partial}{\partial \tilde{r}}(\tilde{r}\tilde{U}_t\tilde{h}) - \frac{1}{\tilde{r}}\frac{\partial}{\partial \tilde{r}}\left\{\tilde{r}\left(-\frac{\partial \tilde{P}}{\partial \tilde{r}}\right)^{1/n}\tilde{h}^{2n+1}\right\}\frac{\left(\frac{1}{2}\right)^{\frac{1}{n}+2}2}{\frac{1}{n}+2} \tag{189}$$

Finally, further rearranging the second term on the right-hand side yields the thinning equation:

$$\frac{\partial \tilde{h}}{\partial \tilde{t}} = -\frac{1}{\tilde{r}}\frac{\partial}{\partial \tilde{r}}(\tilde{r}\tilde{U}_t\tilde{h}) - \frac{1}{\tilde{r}}\frac{\partial}{\partial \tilde{r}}\left[\tilde{r}\left(-\frac{\partial \tilde{P}}{\partial \tilde{r}}\right)^{1/n}\tilde{h}^{2n+1}\right]\frac{n}{(1+2n)2^{1/n+1}} \tag{190}$$

where on the right-hand side, the first term gives rise to a plug flow velocity profile within the film and the second one a parabolic like velocity profile. The presence of both of these terms indicates partially mobile interfaces. Note that $n = 1$ reduces the thinning equation to fit Newtonian fluid as described by Ozan & Jakobsen (2019*a*). In this case, the thinning equation can be written as:

$$\frac{\partial \tilde{h}}{\partial \tilde{t}} = -\frac{1}{\tilde{r}}\frac{\partial}{\partial \tilde{r}}(\tilde{r}\tilde{U}_t\tilde{h}) + \frac{1}{1\tilde{2}r}\frac{\partial}{\partial \tilde{r}}\left(\tilde{r}\frac{\partial \tilde{P}}{\partial \tilde{r}}\tilde{h}^3\right) \tag{191}$$

The pressure equation is obtained by adding a term to account for the attractive van der Waals forces to the dimensionless normal stress balance presented in Eq. 146. This term is necessary to estimate the film rupture which requires the presence of intermolecular forces. This yields:

$$\tilde{P} = 2 - \frac{1}{2\tilde{r}}\frac{\partial}{\partial \tilde{r}}\left(\tilde{r}\frac{\partial \tilde{h}}{\partial \tilde{r}}\right) + \frac{A^*}{\tilde{h}^3} \tag{192}$$

Here, A^* is the dimensionless Hamaker constant, which is defined as $A^* = \frac{A}{6\pi\varepsilon^6 R_p^2\sigma}$.

Following Davis et al. (1989), the boundary integral of the Stokes flow is applied to compute the tangential mobility of the interface:

$$U_t = \frac{1}{\mu_d}\int_0^{r_\infty} \phi\ \tau_d \,\mathrm{d}\rho, \tag{193}$$

where

$$\phi = \frac{1}{2\pi}\rho\int_0^{\pi}\frac{\cos\theta}{\sqrt{r^2+\rho^2-2r\rho\cos\theta}}\,\mathrm{d}\theta \tag{194}$$

Non-dimensionalizing these equation yields:

$$\frac{\varepsilon^3\sigma}{\eta_0}\tilde{U}_t = \frac{\varepsilon^2\sigma}{\mu_d}\int_0^{r_\infty}\tilde{\phi}\ \tilde{\tau}_d \,\mathrm{d}\tilde{\rho}, \tag{195}$$

and

$$\tilde{\phi} = \frac{1}{2\pi}\tilde{\rho}\int_0^{\pi}\frac{\cos\theta}{\sqrt{\tilde{r}^2+\tilde{\rho}^2-2\tilde{r}\tilde{\rho}\cos\theta}}\,\mathrm{d}\theta \tag{196}$$

An expression for τ_d can be obtained from the tangential stress balance presented in Eq. 150, which for $z \geq 0$ becomes:

$$\left(-\frac{\partial \tilde{v}_r}{\partial \tilde{z}}\right)^n = \tilde{\tau}_d \tag{197}$$

Inserting the obtained expression for the velocity gradient from Eq. 155 evaluated at the interface gives:

$$-\frac{\tilde{h}}{2}\frac{\partial \tilde{P}}{\partial \tilde{r}} = \tilde{\tau}_d \tag{198}$$

Thus, the dimensionless boundary integral equation can be expressed on the following form:

$$\tilde{U}_t = -\frac{1}{2\pi\lambda^*}\int_0^{\tilde{r}_\infty}\int_0^{\pi}\frac{\tilde{h}}{2}\frac{\partial \tilde{P}}{\partial \tilde{r}}\frac{\cos\theta}{\sqrt{\tilde{r}^2+\tilde{\rho}^2-2\tilde{r}\tilde{\rho}\cos\theta}}\,\mathrm{d}\theta\,\mathrm{d}\tilde{\rho} \tag{199}$$

in which λ^* is the dispersed to continuous phase viscosity ratio, defined by: $\lambda^* = \frac{\varepsilon\mu_d}{\eta_0}$

The thinning, pressure and boundary integral equations, i.e., Eqs. 190, 192 and 199, are solved simultaneously with the following boundary and initial conditions:

$$\frac{\partial \tilde{h}}{\partial \tilde{r}}\Big|_{\tilde{r}=0} = 0, \qquad \frac{\partial \tilde{P}}{\partial \tilde{r}}\Big|_{\tilde{r}=0} = 0, \qquad \tilde{U}_t\Big|_{\tilde{r}=0} = 0 \tag{200}$$

$$\frac{\partial \tilde{h}}{\partial \tilde{t}}\Big|_{\tilde{r}_\infty} = -\tilde{V}_{app}, \qquad \tilde{p}|_{\tilde{r}_\infty} = 0 \tag{201}$$

$$\tilde{h} = \tilde{h}_{00} + \tilde{r}^2 \tag{202}$$

Here, the boundary conditions presented in Eq. 200 are employed due to the assumption of axisymmetry within the film. Moreover, due to the assumption of a gentle collision, it is presumed that the shape of the interface and the approach velocity are unaffected by the collision at a large enough radial distance, $\tilde{r}_\infty$. Thus, the boundary conditions in Eq. 201 appear. Furthermore, the initial thickness in Eq. 202 resembles the distance between two spherical fluid particles.

2.2.1 Immobile interfaces

When λ^* is large, i.e., the interfaces are immobile, it can be observed from the boundary integral equation in Eq. 199, that the tangential velocity of the interfaces is insignificant. Thus the boundary integral equation is omitted in this case. Also, the thinning equation reduces to:

$$\frac{\partial \tilde{h}}{\partial \tilde{t}} = -\frac{1}{\tilde{r}}\frac{\partial}{\partial \tilde{r}}\left[\tilde{r}\left(-\frac{\partial \tilde{P}}{\partial \tilde{r}}\right)^{1/n}\tilde{h}^{2n+1}\right]\frac{n}{(1+2n)2^{1/n+1}} \tag{203}$$

Hence, for immobile interfaces, the thinning equation in Eq. 203 are solved together with the pressure equation (Eq. 192) with the same boundary and initial conditions as for partially mobile interfaces (except for the tangential velocity condition).

2.2.2 Fully mobile interfaces

As λ^* approaches zero, the interfaces become fully mobile and the thinning equation is dominated by the plug-flow term, which gives:

$$\frac{\partial \tilde{h}}{\partial \tilde{t}} = -\frac{1}{\tilde{r}}\frac{\partial}{\partial \tilde{r}}(\tilde{r}\tilde{U}_t\tilde{h}) \tag{204}$$

When the interfaces are fully mobile, the effect of λ^* on the drainage disappears. Thus, we define a new tangential velocity, $\hat{U}_t$. The boundary integral equation is then written as:

$$\hat{U}_t = \lambda^*\tilde{U}_t = -\frac{1}{2\pi}\int_0^{\tilde{r}_\infty}\int_0^{\pi}\frac{\tilde{h}}{2}\frac{\partial \tilde{P}}{\partial \tilde{r}}\frac{\cos\theta}{\sqrt{\tilde{r}^2+\tilde{\rho}^2-2\tilde{r}\tilde{\rho}\cos\theta}}\,\mathrm{d}\theta\,\mathrm{d}\tilde{\rho} \tag{205}$$

Replacing $\tilde{U}_t$ with $\hat{U}_t$ in the thinning equation in Eq. 205 gives:

$$\frac{\partial \tilde{h}}{\partial \tilde{t}} = -\frac{1}{\tilde{r}}\frac{\partial}{\partial \tilde{r}}\left(\tilde{r}\frac{1}{\lambda^*}\hat{U}_t\tilde{h}\right) \tag{206}$$

A new characteristic time scale, $\bar{t_\lambda}$, can now be defined via:

$$\bar{t} = \lambda^*\bar{t_\lambda} = \lambda^*\frac{R_p\eta_0}{\varepsilon^2\sigma} \tag{207}$$

Writing Eq. 206 in dimensional form and multiplying with λ^* yields:

$$\lambda^*\frac{\bar{h}}{\bar{t}}\frac{\partial \tilde{h}}{\partial \tilde{t}} = -\frac{\bar{h}\bar{v}_r}{\bar{r}}\frac{1}{\tilde{r}}\frac{\partial}{\partial \tilde{r}}(\tilde{r}\hat{U}_t\tilde{h}) \tag{208}$$

Then, the new characteristic time scale in Eq. 207 and the characteristic scales in Eq. 130 are inserted, which gives:

$$\frac{\varepsilon^4\sigma}{\eta_0}\frac{\partial \tilde{h}}{\partial \tilde{t_\lambda}} = -\frac{\varepsilon^4\sigma}{\eta_0}\frac{1}{\tilde{r}}\frac{\partial}{\partial \tilde{r}}(\tilde{r}\hat{U}_t\tilde{h}) \tag{209}$$

Thus, the thinning equation for fully mobile interfaces becomes:

$$\frac{\partial \tilde{h}}{\partial \tilde{t_\lambda}} = -\frac{1}{\tilde{r}}\frac{\partial}{\partial \tilde{r}}(\tilde{r}\hat{U}_t\tilde{h}) \tag{210}$$

As for the case with partially mobile interfaces, here, the thinning equation, pressure equation and the boundary integral equation are solved simultaneously with boundary and initial conditions (Eq.200-202). However, at r_∞ the film thickness boundary condition in Eq. 201 includes the time derivative. Hence, the characteristic time scale transformation given in Eq. 207 is inserted into the dimensional version of this boundary condition:

$$\frac{\bar{h}}{\lambda^*\bar{t}_\lambda}\frac{\partial \tilde{h}}{\partial \tilde{t}_\lambda}\Big|_{\tilde{r}_\infty} = -\bar{v}_z\tilde{V}_{app} \tag{211}$$

Inserting $\bar{h}$, $\bar{t}_\lambda$ and $\bar{v_z}$ in addition to multiplying with λ^* gives:

$$\frac{\varepsilon^4\sigma}{\eta_0}\frac{\partial\tilde{h}}{\partial\tilde{t}_\lambda}\Big|_{\tilde{r}_\infty} = -\lambda^*\frac{\varepsilon^4\sigma}{\eta_0}\tilde{V}_{app} \tag{212}$$

which can be reduced to:

$$\frac{\partial\tilde{h}}{\partial\tilde{t}_\lambda}\Big|_{\tilde{r}_\infty} = -\lambda^*\tilde{V}_{app}, \tag{213}$$

3 Numerical procedure

The thinning, pressure and boundary integral equations (Eqs. 190,192 and 199) are implemented in MATLAB together with the boundary and initial conditions (Eqs. 200, 201 and 202) and solved numerically by use of a spectral method based on Chebyshev polynomials (Guo et al. 2013) for $N+1$ grid points. In order to solve the equations, they are discretized on the following form:

$$\begin{aligned}&\left[\frac{3}{2\Delta t}I\right] h_{k+1} - \frac{h_k}{\Delta t} + \frac{h_{k-1}}{2\Delta t} = -\left[diag(1/r)\right]\ [D]\ \left[diag(r\ h_k)\right]\ U_{t,k+1} \\ &- \frac{n}{(1+2n)2^{1/n+1}}\ [diag(1/r)]\ [D]\ [diag(r)]\ ([-D][P_k])^{1/n-1}\ [h_k^{2n+1}][-D]\ P_{k+1}\end{aligned} \tag{214}$$

$$[I]\ P_{k+1} = 2 - \frac{1}{2}[diag(1/r)]\ [D]\ [diag(r)]\ [D]\ h_{k+1} + \frac{A^*}{h_k^3} \tag{215}$$

and

$$[I]\ U_{t,k+1} = -\frac{1}{\lambda^*}\ [A_{int}]\left[diag\left(\frac{h_k}{2}\right)\right]\ [D]\ P_{k+1} \tag{216}$$

As it is known that all equations are in dimensionless form at this point, the tilde notation is skipped. Here, k is the time step number, and the equations are solved at step $k+1$, i.e., all terms which include $k+1$ are unknown. Terms including k or $k-1$ are known from solutions at previous time steps. Note that the square brackets indicates matrices of size $(N+1)\times(N+1)$, while the variables outside the square brackets, h, P and U, are column arrays of length $N+1$, then, n, A^* and λ^* are here constants. Moreover, Δt is the time step size, and the time discretization employed on the unsteady term in the thinning equation is chosen due to its proven stability (Guo et al. 2013). $[I]$ is the $(N+1)\times(N+1)$ identity matrix, while $[D]$ is the $(N+1)\times(N+1)$ derivative matrix, which is obtained through Chebyshev polynomials that is mapped linearly to fit the domain of $r=0$ to $r=r_\infty$. The matrix $[D]$ takes the derivative with respect to r at each grid point. Furthermore, the *diag* operation represents arrays made into diagonal matrices. To illustrate the necessity of this diagonalization, the two following examples including an unknown array f, is presented:

$$[D]\ r\ f = \frac{\partial r}{\partial r}\ f, \tag{217}$$

Here, the derivative operator does not apply on the unknown array. Whereas,

$$[D]\ [diag(r)]\ f = \frac{\partial}{\partial r}\ (rf), \tag{218}$$

in this case, the derivative operator applies on both the radial array and the unknown array, f. To provide an example of the diagonal matrices employed in this work,

$$diag(r) = \begin{bmatrix} r_{(1)} & 0 & \cdots & 0 \\ 0 & r_{(2)} & \cdots & 0 \\ \vdots & \vdots & \ddots & \vdots \\ 0 & 0 & \cdots & r_{(N+1)} \end{bmatrix} \tag{219}$$

can be expressed.

Note that the matrix $[A_{int}]$ carries out the double integration in the boundary integral equation shown in Eqs. 199 and 205 through the method presented by Ozan & Jakobsen (2019*a*). Their method takes care of the singularity issue that arises when $\theta = 0$ and $r = \rho$. The details of their method are out of scope for this thesis and will therefore not be discussed here.

Gathering the unknown terms in the matrix equations (Eqs. 220, 221 and 222) on the left hand side yields:

$$\begin{aligned}&\left[\frac{3}{2\Delta t}I\right] h_{k+1} + [diag(1/r)]\ [D]\ [diag(r\ h_k)]\ U_{k+1} \\ &+ \frac{n}{(1+2n)2^{1/n+1}}\ [diag(1/r)]\ [D]\ [diag(r)]\ ([-D][P_k])^{1/n-1}\ [h_k^{2n+1}][-D]\ P_{k+1} = \frac{h_k}{\Delta t} - \frac{h_{k-1}}{2\Delta t}\end{aligned} \tag{220}$$

$$[I]\ P_{k+1} + \frac{1}{2}[diag(1/r)]\ [D]\ [diag(r)]\ [D]\ h_{k+1} = 2 + \frac{A^*}{h_k^3} \tag{221}$$

and

$$[I]\ U_{t,k+1} + \frac{1}{\lambda^*}\ [A_{int}]\left[diag\left(\frac{h_k}{2}\right)\right]\ [D]\ P_{k+1} = 0 \tag{222}$$

These equations are then combined to the following matrix equation:

$$AU = RHS \tag{223}$$

where U is a column array consisting of the unknown terms ($N+1$ nodal values of each h_{k+1}, P_{k+1} and $U_{t,k+1}$). A is a matrix with the corresponding weights defined from the discretized thinning, pressure and boundary integral equations. Moreover, RHS is a column array which contains the known values. The matrix A is then further divided into one block per unknown variable per equation, i.e., nine blocks, which is written as:

$$\begin{bmatrix} A11 & A12 & A13 \\ A21 & A22 & A23 \\ A31 & A32 & A33 \end{bmatrix}_{3(N+1)\times 3(N+1)} \begin{bmatrix} h_{k+1} \\ P_{k+1} \\ U_{t,k+1} \end{bmatrix}_{3(N+1)} = \begin{bmatrix} RHS1 \\ RHS2 \\ RHS3 \end{bmatrix}_{3(N+1)} \tag{224}$$

The rows of the A blocks represent the thinning equation, pressure equation, and the boundary integral equation in the order mentioned, while the columns represent the film thickness, excess pressure, and the tangential velocity of the interfaces, respectively. A is then of size $3(N+1)\times 3(N+1)$, while the right-hand side array and the array of unknowns U are of length $3(N+1)$. The discretized thinning equation gives the following weights corresponding to the unknown film thickness, pressure, and tangential velocity, respectively:

$$[A11] = \frac{3}{2\Delta t}I \tag{225}$$

$$[A12] = \frac{n}{(1+2n)2^{1/n+1}} \; [diag(1/r)] \; [D] \; [diag(r)] \; ([-D][P_k])^{1/n-1} \; [h_k^{2n+1}][-D] \tag{226}$$

$$[A13] = [diag(1/r)] \; [D] \; [diag(r \; h_k)] \tag{227}$$

Then, the weights of the unknown terms in the pressure equation can be divided into the following blocks:

$$[A21] = \frac{1}{2}[diag(1/r)] \; [D] \; [diag(r)] \; [D] \tag{228}$$

$$[A22] = [I] \tag{229}$$

$$[A23] = [0] \tag{230}$$

The boundary integral equation results in the weights:

$$[A31] = [0] \tag{231}$$

$$[A32] = \frac{1}{\lambda^*} \; [A_{int}] \left[diag \left(\frac{h_k}{2} \right) \right] \; [D] \tag{232}$$

$$[A33] = [I] \tag{233}$$

Then the right-hand sides of the discretized thinning, pressure and boundary integral equations are expressed as:

$$RHS1 = \frac{h_k}{\Delta t} - \frac{h_{k-1}}{2\Delta t} \tag{234}$$

$$RHS2 = 2 + \frac{A^*}{h_k^3} \tag{235}$$

$$RHS3 = 0 \tag{236}$$

Furthermore, the boundary conditions need to be incorporated in the matrix A and on the right-hand side of the corresponding matrix equation. The boundary condition $\frac{\partial \tilde{h}}{\partial \tilde{r}}|_{\tilde{r}=0} = 0$ gives:

$$A_{(1,i)} = [D_{(1,i)} \;\; 0 \;\; 0 \ldots 0] \tag{237}$$

Note that the index i means all columns. Thus, in row 1 of A, column 1 to $N+1$ is filled with the first row of the derivative matrix, D. Then, the rest of row 1 consists of $2(N+1)$ zeros.

The corresponding right-hand side yields:

$$RHS_{(1)} = 0 \tag{238}$$

The boundary condition $\frac{\partial \tilde{h}}{\partial \tilde{t}}\big|_{\tilde{r}_\infty} = -\tilde{V}_{app}$ can be be implemented as:

$$A_{(N+1,i)} = [0 \;\; 0 \ldots \;\; 1 \;\; 0 \;\; 0 \ldots] \tag{239}$$

Here the row $N+1$ in the matrix A contains a 1 in column $N+1$, which corresponds to the variable h in the the thinning equation in the position r_∞. The rest of this row is filled with zeros. Following the time discretization employed in the thinning equation gives the following right-hand side entry in the position $N+1$:

$$RHS_{(N+1)} = \frac{2\Delta t}{3}\left(-V_{app} + \frac{2h_{k,(N+1)}}{\Delta t} - \frac{h_{k-1,(N+1)}}{2\Delta t}\right) \tag{240}$$

$\frac{\partial \tilde{p}}{\partial \tilde{r}}\big|_{\tilde{r}=0} = 0$ is expressed in A as:

$$A_{(N+2,i)} = [0 \;\; 0 \ldots D_{(1,i)} \;\; 0 \;\; 0 \ldots] \tag{241}$$

which means that row $N+2$ in A is filled with the first row of the derivative matrix in column position $N+2$ to $2(N+1)$, while the rest of the row is filled with zeros. The corresponding right-hand side is expressed as:

$$RHS_{(N+2)} = 0 \tag{242}$$

Then, the boundary condition $\tilde{p}|_{\tilde{r}_\infty} = 0$ gives:

$$A_{(2(N+1),i)} = [0 \;\; 0 \ldots \;\; 1 \;\; 0 \;\; 0 \ldots] \tag{243}$$

where column $2(N+1)$ has the entry 1 in row $2(N+1)$ in the matrix A. The right-hand side gives:

$$RHS_{(2(N+1))} = 0 \tag{244}$$

Finally, $\tilde{U}_t\big|_{\tilde{r}=0} = 0$ is implemented as:

$$A_{(2N+3,i)} = [0 \;\; 0 \ldots \;\; 1 \;\; 0 \;\; 0 \ldots] \tag{245}$$

and

$$RHS_{(2N+3)} = 0 \tag{246}$$

where row $2N+3$ in the matrix A consists of a 1 in the position $2N+3$ and the rest of the row is filled with zeros. The right-hand side array is filled with a zero in position $2N+3$.

The film thins very rapidly at the last stage of interaction due to intermolecular forces. Thus upon reaching a sufficiently small film thickness, i.e., the critical film thickness, the thickness goes to virtually zero extremely fast compared to the rest of the interaction, and there is no other possibility than coalescence. This critical film thickness criterion is set as 0.001 in the MATLAB code given in App. B. The code includes a description of the eight necessary steps to solve the discretized model equations. Although the numerical procedure presented in this chapter describes the partially mobile solver, the immobile and fully mobile solver are built on the same steps. As mentioned in Chapter 2.2.1, the only differences between the partially mobile and the immobile solvers are that the latter does not require the boundary integral equation and solves only the parabolic like contribution to the velocity profile term in the thinning equation as shown in Eq. 203. Then, as mentioned in Chapter 2.2.2, the fully mobile solver only requires the plug-flow contribution term in the thinning equation given in Eq. 210, which makes this solver independent of n. Also, λ^* only appears in the boundary condition at r_∞ given in Eq. 213 where it is multiplied with V_{app}. Therefore, these variables can be combined to one variable $V_{app}\lambda^*$ in this solver. Note that the boundary integral equation should be solved on the form presented in Eq. 205 and the boundary condition in Eq. 213 replaces the film thickness boundary condition in Eq. 201.

4 Results and discussion

4.1 Validation of the solvers

The non-Newtonian immobile solver employed in this work is validated by comparing results obtained with $n = 1$ with Ozan & Jakobsen (2019*a*)'s immobile solver results that apply for Newtonian flow. Figures 2 and 3 depict the film thickness and pressure profiles, respectively. Here, both solvers are run in Matlab with $V_{app} = 1$ and $A^* = 0$. The results for the non-Newtonian solver seem to be in perfect agreement with the ones obtained with the Newtonian solver. Thus, the non-Newtonian immobile solver gives correct results for $n = 1$, and it is assumed that the solver yields accurate results for power index values near 1 as well.

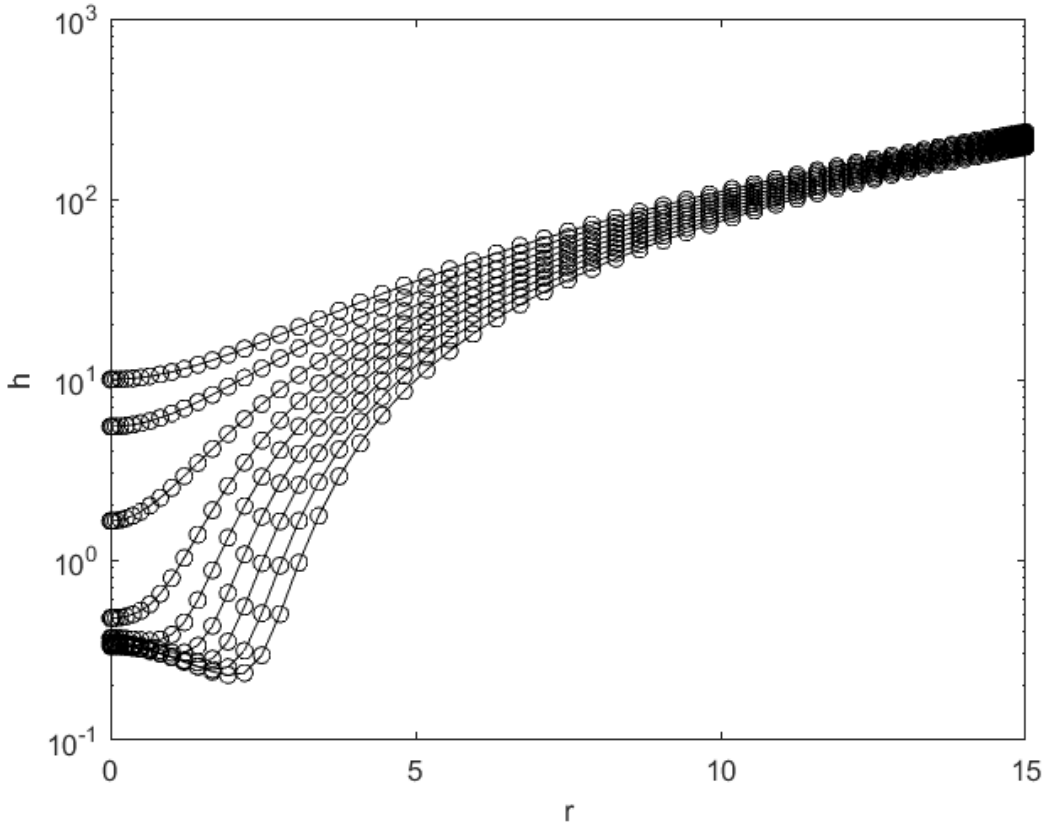

Figure 2: Film thickness as a function, of r for varying time steps. Profiles are obtained for immobile interfaces with $A^* = 0$, $V_{app} = 1$, $h_{00} = 10$ and $r_\infty = 15$. The lines represent the Newtonian solver, while the circles show the solution obtained by the non-Newtonian model with $n = 1$.

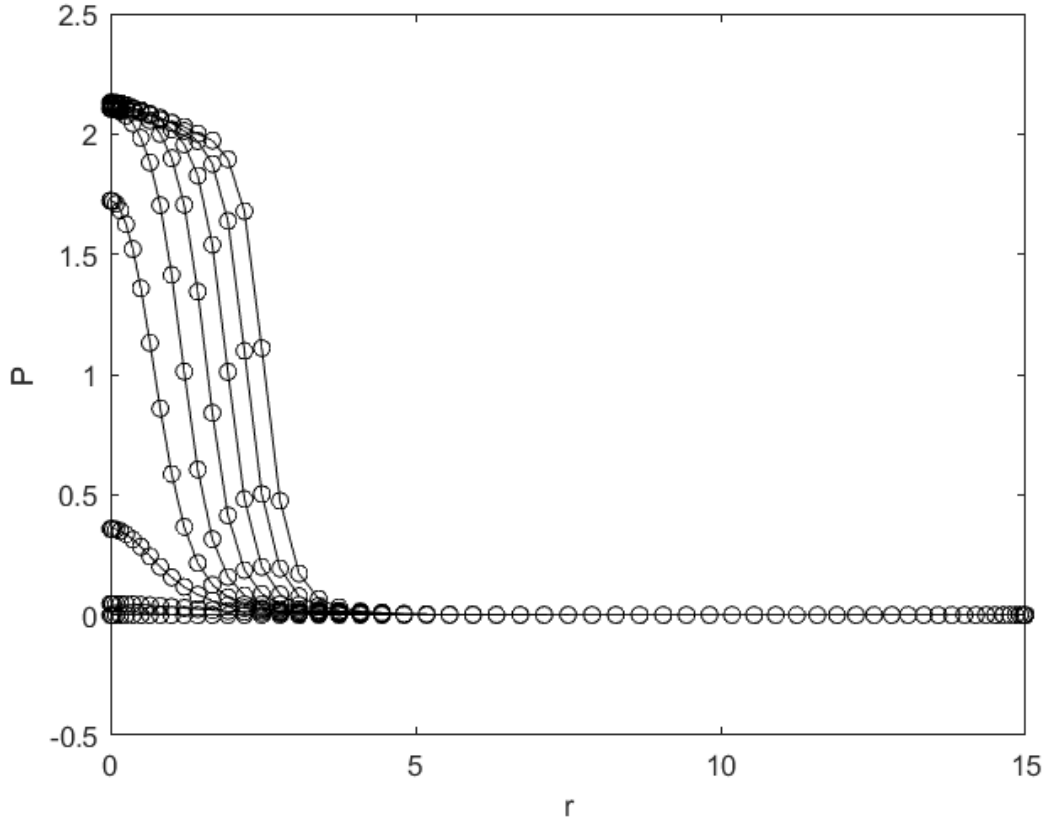

Figure 3: Pressure as a function of r and t. Profiles are obtained for immobile interfaces with $A^* = 0$, $V_{app} = 1$, $h_{00} = 10$ and $r_\infty = 15$. The lines represent the Newtonian solver, while the circles show the solution obtained by the non-Newtonian model with $n = 1$.

Figures 6a, 7b, and 10a in the work of Ozan & Jakobsen (2019*a*) are reproduced to validate the mobile non-Newtonian solvers applied in this work. Figure 4 presents the time development of the film thickness up to $t = 60$, which is obtained using the fully mobile solver. Note that these results correspond to Fig. 6a in the work of Ozan & Jakobsen (2019*a*), and the profiles here seem to match well with their figure. The recreation of Ozan & Jakobsen (2019*a*)'s Fig. 10a is shown in Fig. 5. The curves are here obtained by using the partially mobile solver and seem to fit well with those presented by Ozan & Jakobsen (2019*a*). Figure 6 reveals the reproduction of Ozan & Jakobsen (2019*a*)'s Fig. 7b, where t_c/λ^* is given as a function $\lambda^* V_{app}$ for varying values of λ^*. The same trend as observed in their results is detected here. Thus, both the partially and fully mobile solvers are assumed applicable for power index values near 1.

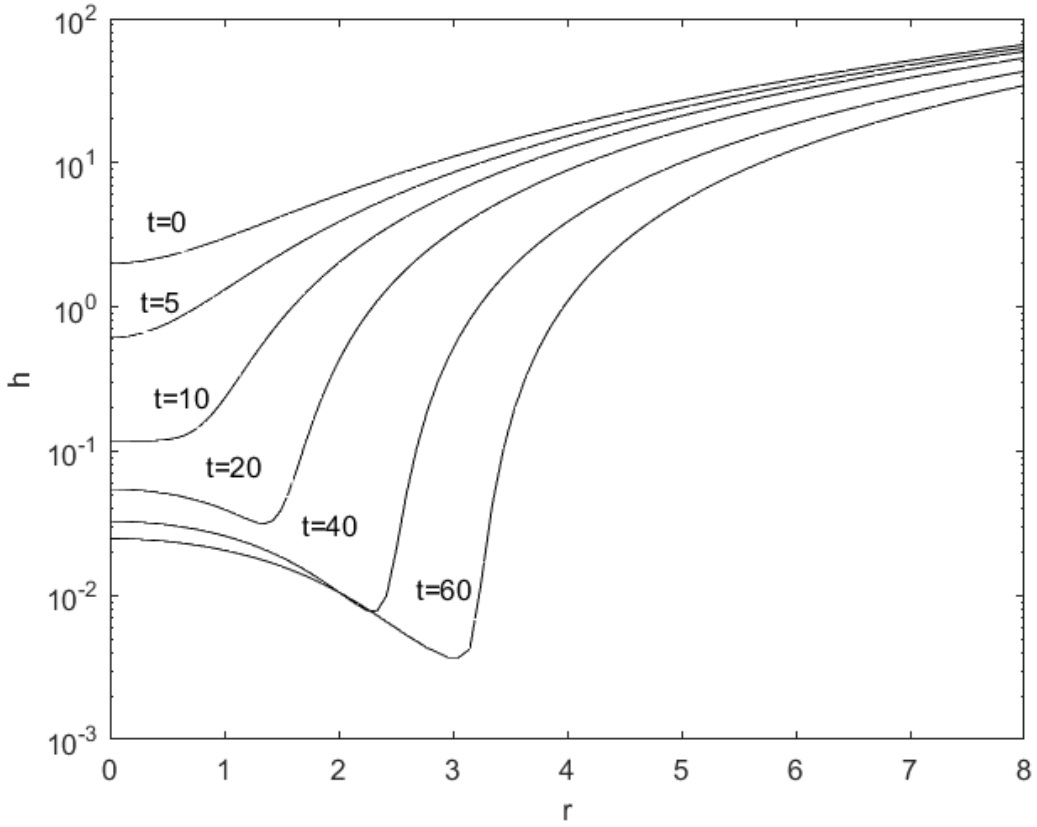

Figure 4: Time evolution of the film thickness for fully mobile interfaces ($\lambda^* = 0$) until $t = 60$ with $V_{app} = 1$, $A^* = 0$, $h_{00} = 2$ and $r_\infty = 30$.

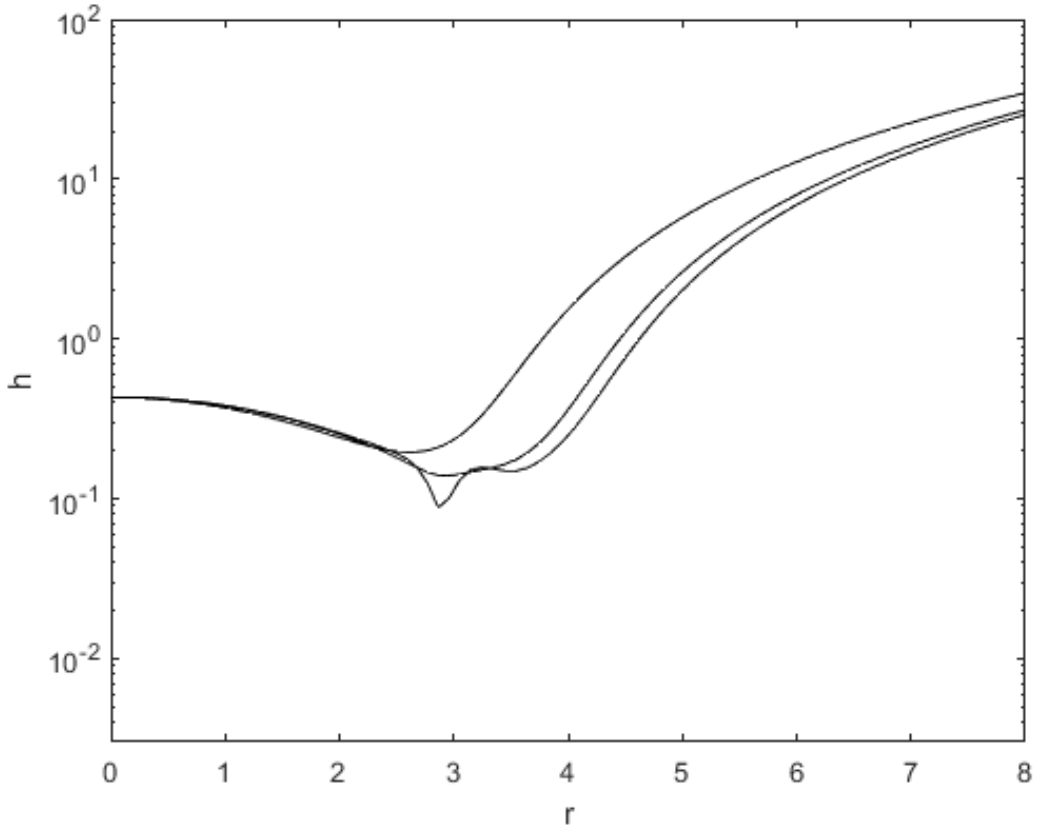

Figure 5: Time evolution of the film thickness for partially mobile interfaces ($\lambda^* = 100$) and Newtonian fluid ($n = 1$) with $V_{app} = 2$, $A^* = 10^{-2}$, $h_{00} = 2$ and $r_\infty = 30$.

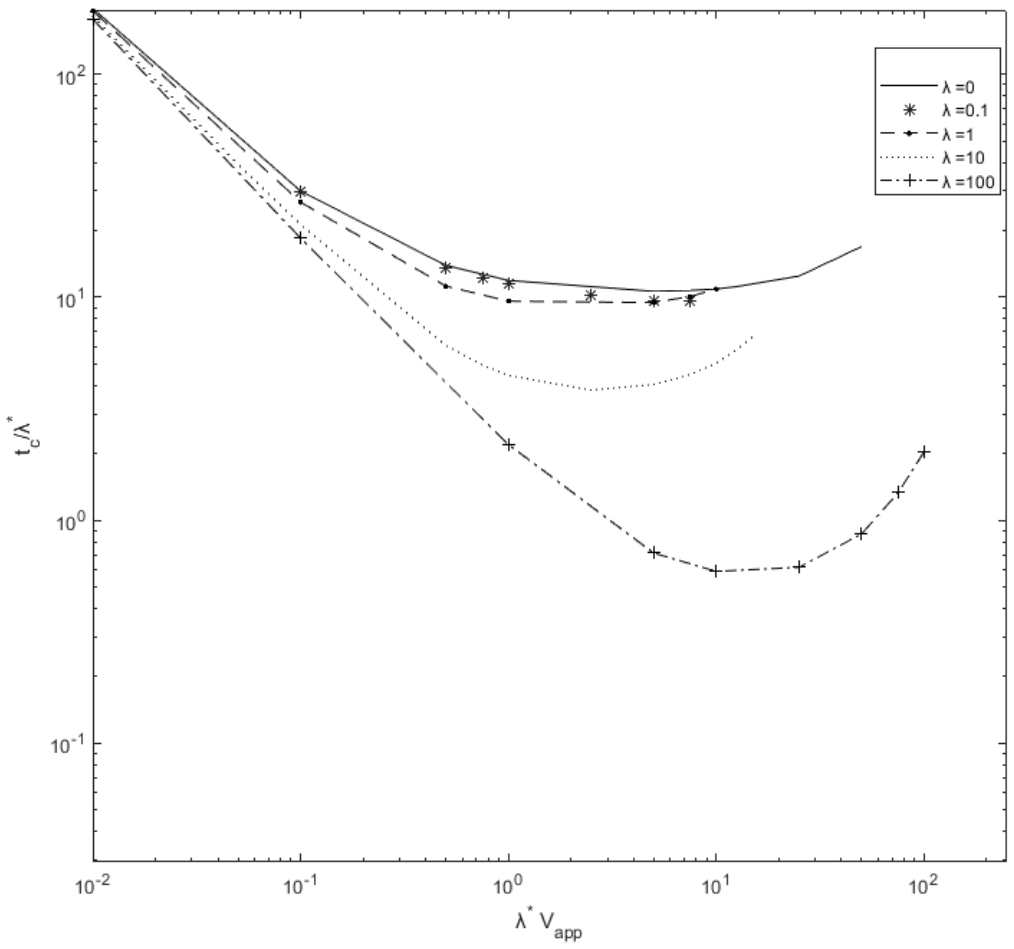

Figure 6: Coalescence time divided by λ^* as a function of $\lambda^* V_{app}$ for varying values of λ^* and mobile interfaces. All results are obtained with $n = 1$, $A^* = 10^{-3}$, $h_{00} = 2$ and $r_\infty = 30$ using the partially mobile solver except for $\lambda^* = 0$, which is obtained by using the fully mobile solver.

Ozan & Jakobsen (2019*a*) detected three different film drainage regimes for a Newtonian fluid. In their Fig. 5, they present the time development of the film thickness profiles for different relative approach velocities and immobile interfaces, where the drainage regime transitions concerning V_{app} can be observed. To further validate the non-Newtonian immobile solver and provide an idea of how the drainage regimes affect the film thickness, this figure is reproduced with $n = 1$ and $A^* = 10^{-4}$. The results are shown in Fig. 7, and it can be observed that they fit well with those obtained by Ozan & Jakobsen (2019*a*).

In Figure 7a), where $V_{app} = 0.003$, the low-velocity drainage regime can be detected. In this regime, film rupture occurs at the center of the fluid particle, i.e., at $r = 0$. This type of rupture is called nose rupture and occurs due to the van der Waals forces becoming significant before the capillary forces can influence the shape of the interface noticeably. In Fig. 7b) where $V_{app} = 0.01$, rupture occurs at the rim instead. A dimple, i.e., a single rim, can be observed at $t = 1069$, which gives the name dimpled drainage regime. In this regime, the capillary number is higher than in the low-velocity regime. Thus,

the capillary forces are more prominent. At $V_{app} = 0.09$, shown in Fig. 7c), an additional rim is visible to the right of the main rim. This secondary rim indicates that a transition has occurred to the final drainage regime, the multiple-rim regime. In addition, it is noticeable that the main rim appears further away from the center than in 7b), which might be caused by the capillary forces becoming even more significant. In Fig. 7d), multiple local minima and maxima can be observed on both sides of the main rim, which occurs even further away from the center than in Fig. 7c). Note that the time step, Δt, is set to 0.01 or smaller in all simulations, and the last profile presented in each plot is the last obtained profile before the film ruptures. Thus, the simulation time at this time step is regarded as the coalescence time, t_c.

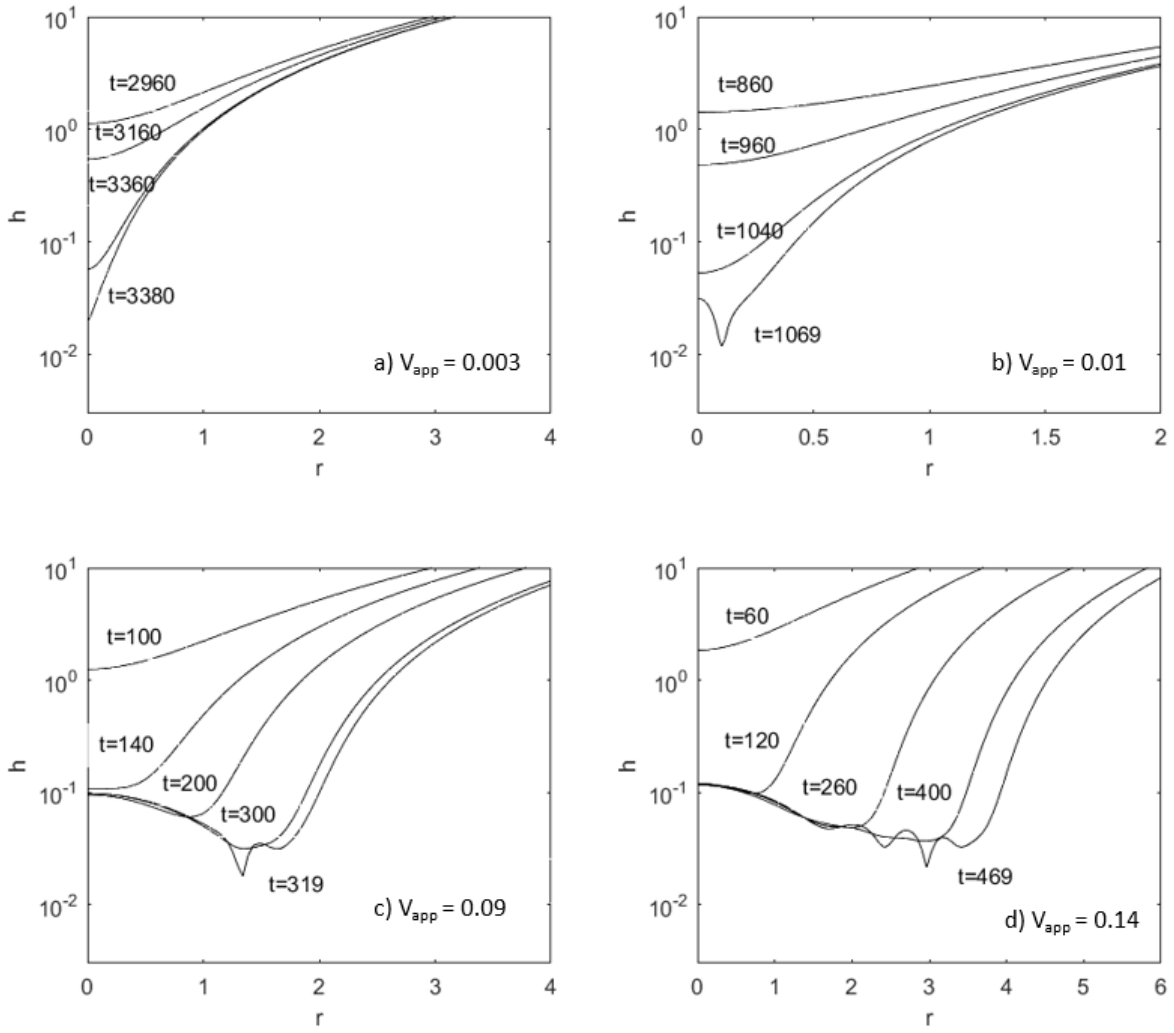

Figure 7: Time development of film thickness as a function of r obtained with immobile interfaces, $n = 1, A^* = 10^{-4}$, $r_\infty = 15$ and $h_{00} = 10$.

4.2 Non-Newtonian film drainage

Figures 8 and 9 present the time development of the film thickness profiles with constant $V_{app} = 0.003$ for varying values of the power index, n, indicating shear-thinning and shear-thickening fluids, respectively. Here, for all eight cases given, nose rupture is detected, and thus the low-velocity regime is identified. Furthermore, the profiles look very close to identical, and the coalescence time is profoundly similar, with only deviance of 0.8% from the smallest value at $t_c = 3377$ to the largest at $t_c = 3405$. Hence, the power index is determined not to be significantly influential here. Note that the results are here obtained with the immobile solver, which also is used to obtain all the upcoming results until Fig. 16.

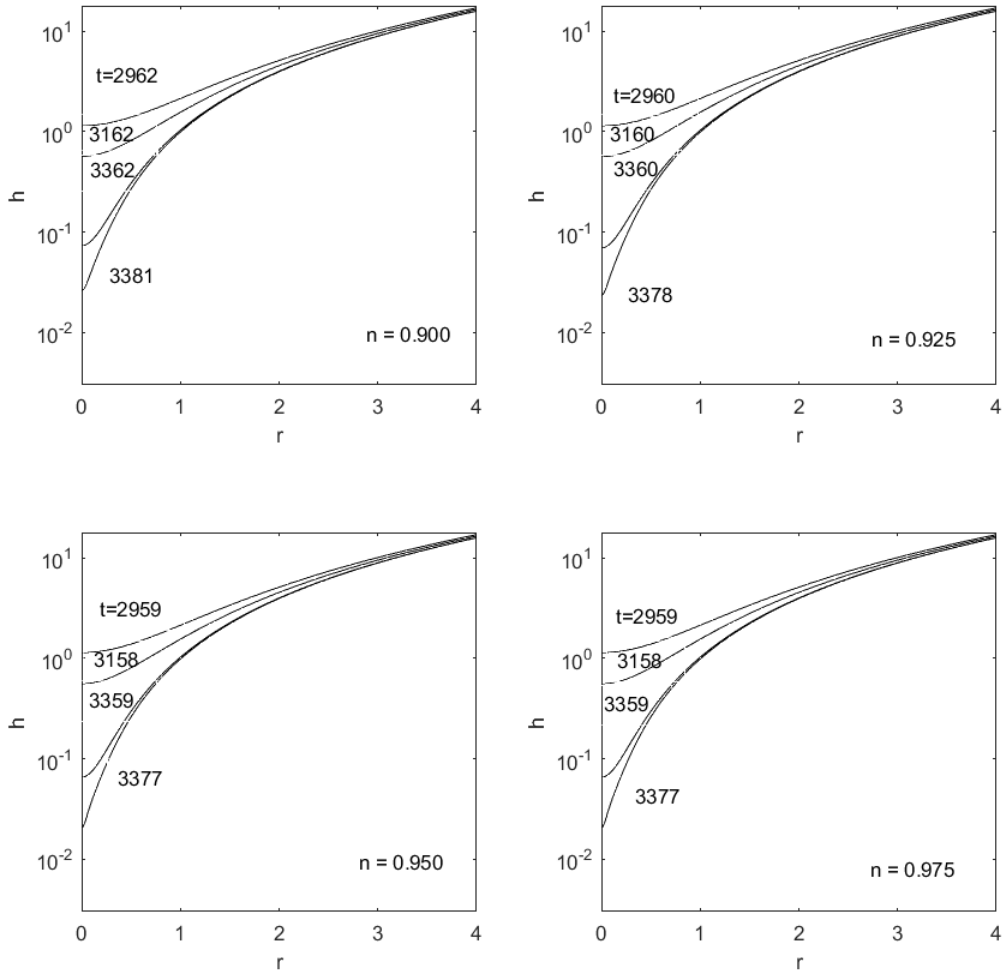

Figure 8: Time evolution of the film thickness for shear-thinning fluids ($n < 1$) and immobile interfaces where $V_{app} = 0.003$, $A^* = 10^{-4}$, $h_{00} = 10$ and $r_\infty = 15$.

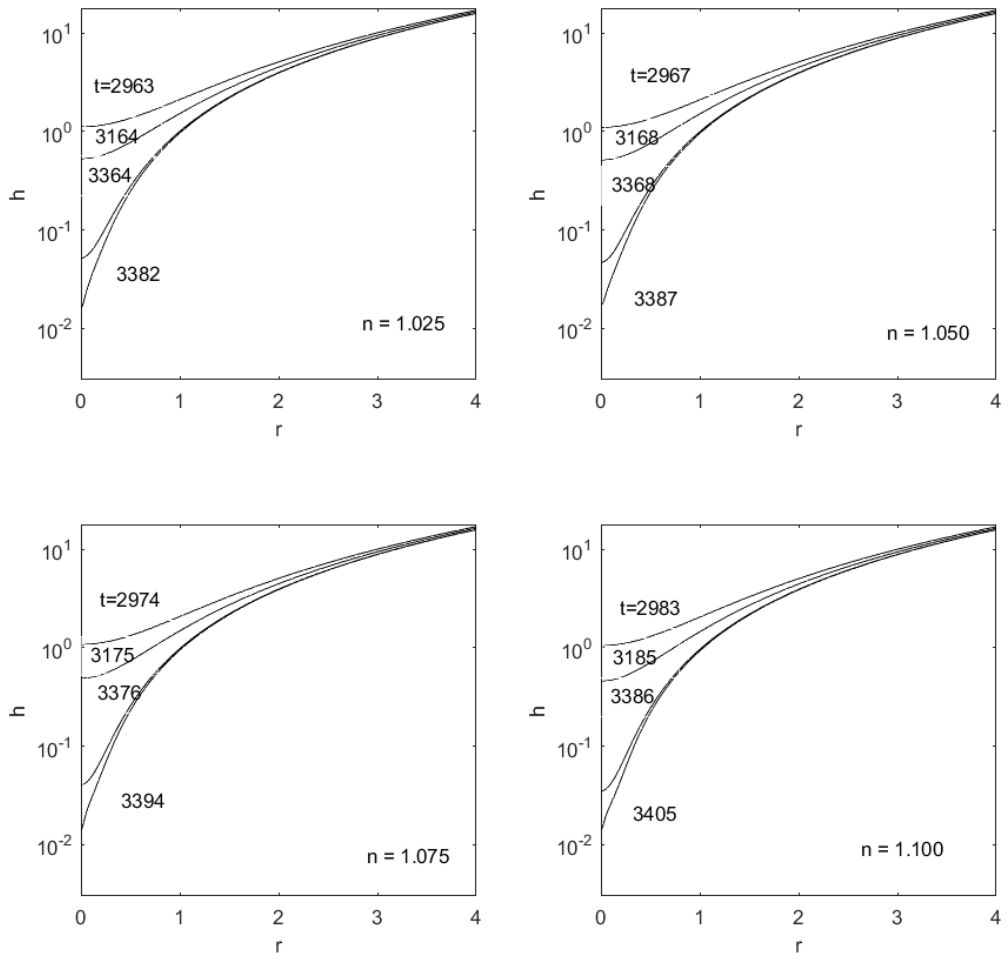

Figure 9: Time evolution of the film thickness of shear-thickening fluids ($n > 1$) and immobile interfaces, where $V_{app} = 0.003$, $A^* = 10^{-4}$, $h_{00} = 10$ and $r_\infty = 15$.

Figure 10 provides the time development of the film thickness at $V_{app} = 0.009$ for varying values of n analogous to shear-thinning fluid. As nose rupture is observed for all cases, drainage still occurs within the low-velocity regime. Note that compared to the previously presented cases, the velocity is increased three times ($V_{app} = 0.003$ to $V_{app} = 0.009$), and the coalescence time is reduced approximately three times. Thus, the coalescence time appears not to be influenced by interfacial deformation effects when the interfaces are immobile at $V_{app} = 0.009$, and the fluid is shear-thinning.

Figure 11 shows the time evolution of the film thickness for values of n which corresponds to shear-thickening fluid for $V_{app} = 0.009$. Here, a dimple can be observed in the last film thickness profile in all four presented cases. Hence, the dimpled drainage regime is entered. Also, notice that the dimple becomes slightly more apparent with increasing power index and the second last film thickness profile occurs closer and closer to the dimple. Furthermore, the coalescence time increases with 7% from $n = 0.9$ to $n = 1.1$. Therefore, the power index is determined to be of significant influence on the drainage behavior and the coalescence time for shear-thickening values of the power index at

$V_{app} = 0.009$ when the interfaces are immobile.

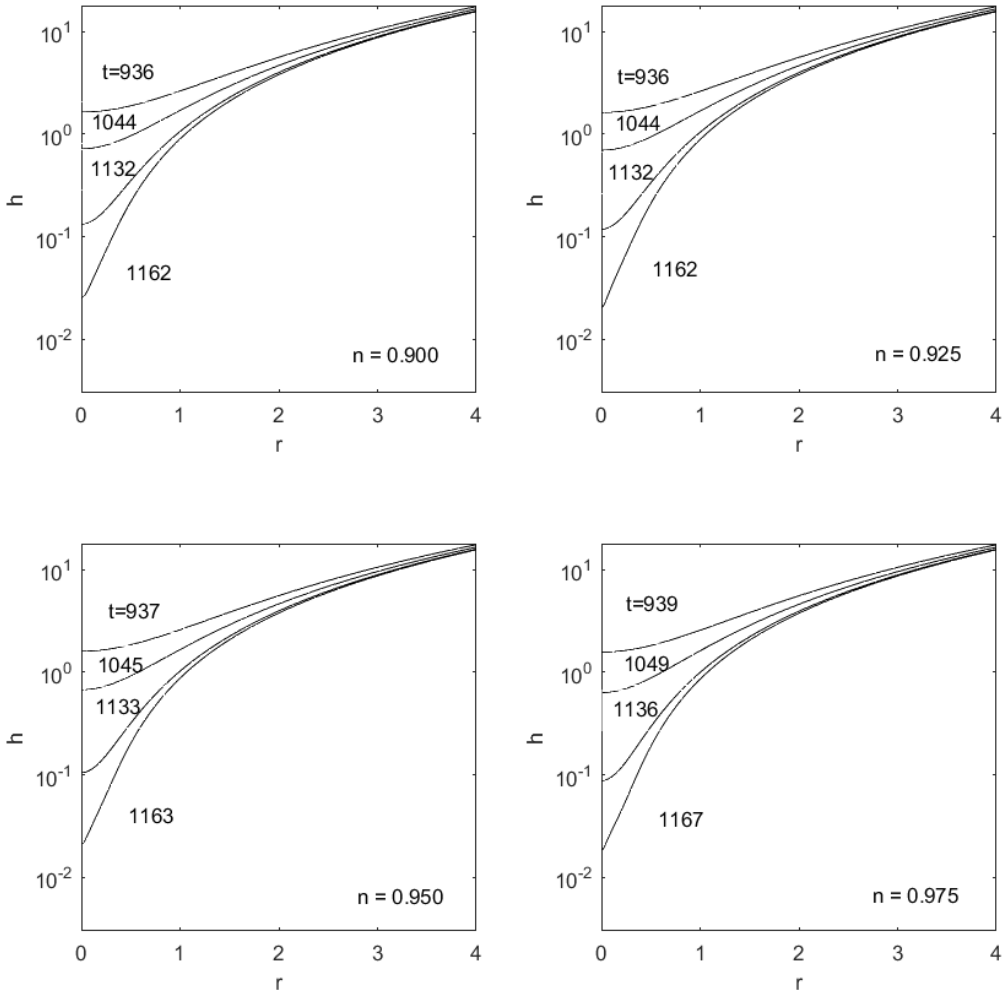

Figure 10: Time evolution of the film thickness for shear-thinning fluids ($n < 1$), where the interfaces are immobile and $V_{app} = 0.009$, $A^* = 10^{-4}$, $h_{00} = 10$ and $r_\infty = 15$.

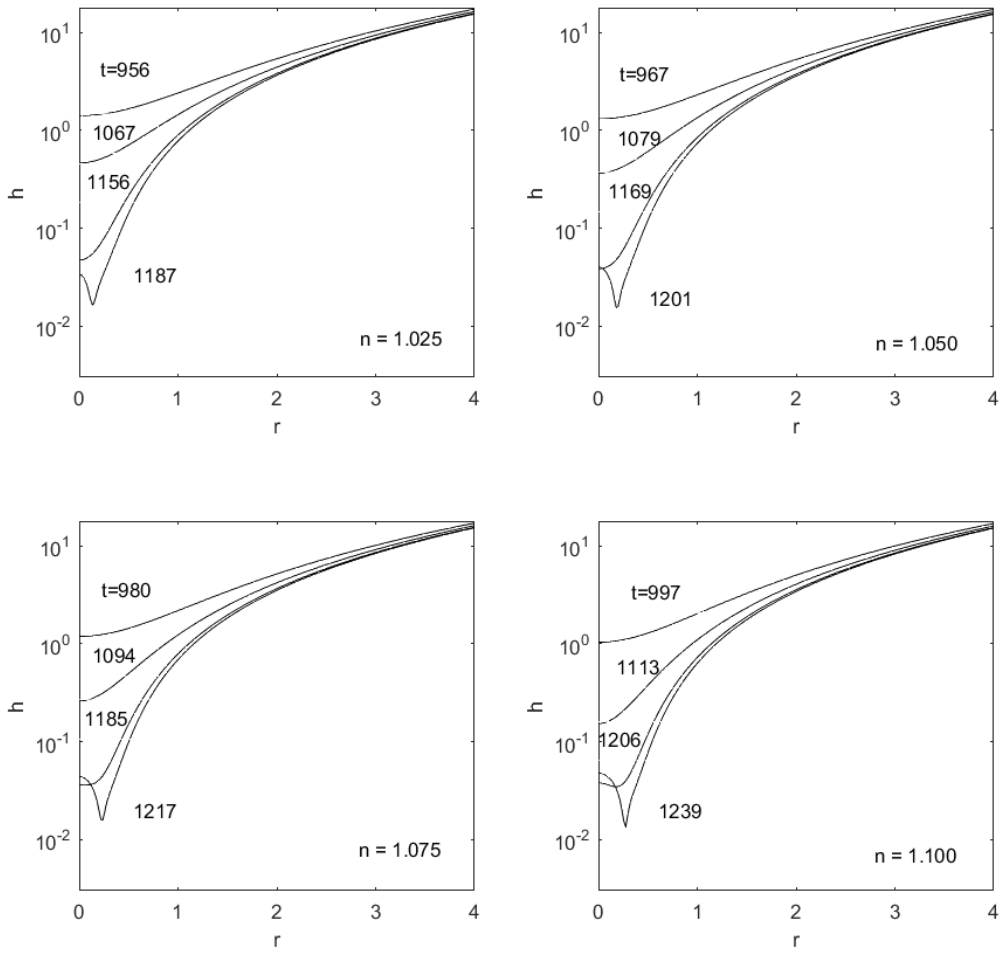

Figure 11: Time evolution of the film thickness for shear-thickening fluids ($n > 1$), where the interfaces are immobile and $V_{app} = 0.009$, $A^* = 10^{-4}$, $h_{00} = 10$ and $r_\infty = 15$.

The time evolution of the film thickness for n values implying shear-thinning fluid for fixed $V_{app} = 0.09$ is given in Fig. 12. For $n = 0.9$, a dimple is observed, indicating drainage within the dimpled drainage regime. Nevertheless, for $n = 0.975$, the formation of a secondary rim is visible. Thus, the multiple-rim regime is reached. Moreover, the coalescence time increases 29% from $n = 0.900$ to $n = 0.975$, indicating that the power index influences the film drainage considerably at $V_{app} = 0.09$ for even shear-thinning fluid. Also, the increase in velocity of ten times ($V_{app} = 0.009$ to $V_{app} = 0.09$) gives a decrease in coalescence time of only about six times (1162 to 206 for $n = 0.900$), which is a result of the dimple and multiple-rim formation slowing down the drainage of the film.

Figure 13 presents the time evolution of the film thickness with different values of the power index corresponding to shear-thickening fluid. Here, multiple rims are visible in each plot. It can be observed that the number of minima and maxima increase significantly with increasing power index. Moreover, there is a dramatic increase in the coalescence time with increasing n. This increase is explained by assuming the shear rate approximately constant for a fixed value of V_{app}. Then, from the power law

given in Eq. 123, it can be observed that an increase in the power index leads to increased viscosity. Furthermore, increased viscosity results in the film being more resistant to drainage, and the interfaces are then allowed to deform to a more considerable degree such that more rim-like structures emerge. Then the time needed to reach critical film thickness increases; i.e., it takes longer to get coalescence.

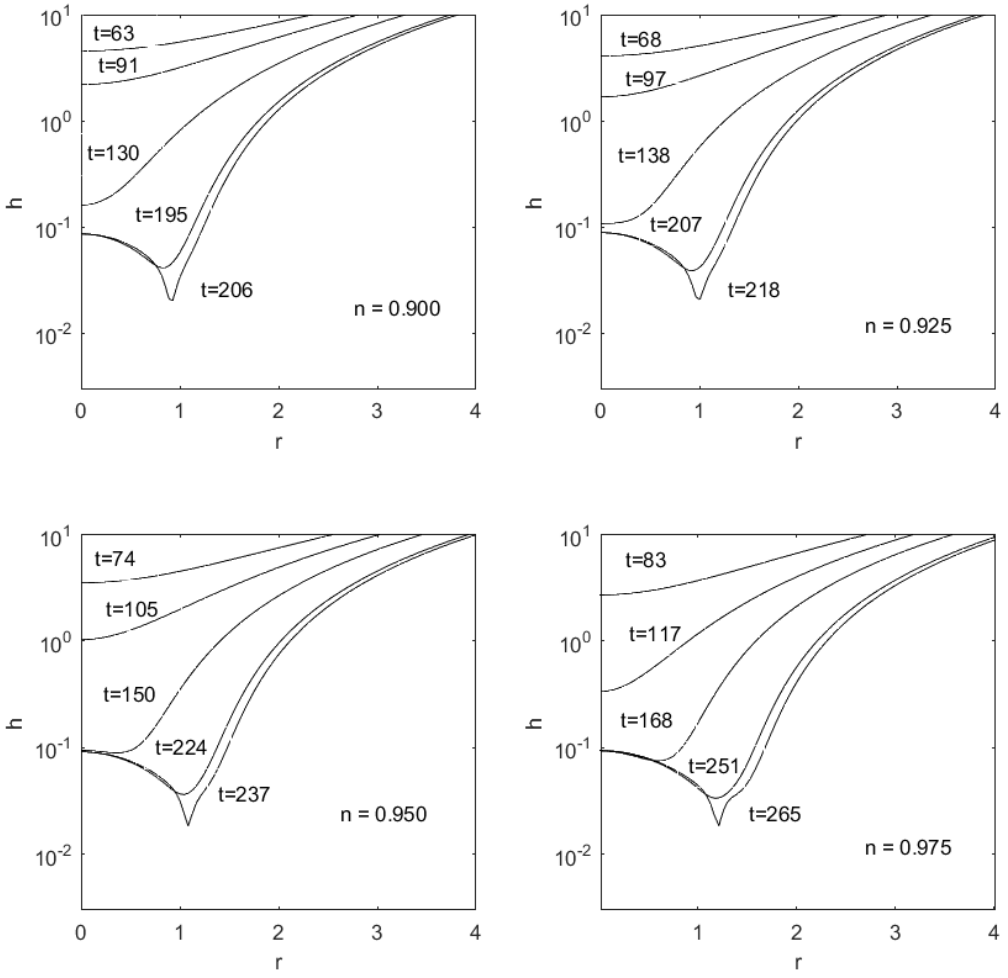

Figure 12: Time evolution of the thickness for shear-thinning fluids ($n < 1$) and immobile interfaces, where $V_{app} = 0.09$, $A^* = 10^{-4}$, $h_{00} = 10$ and $r_\infty = 15$.

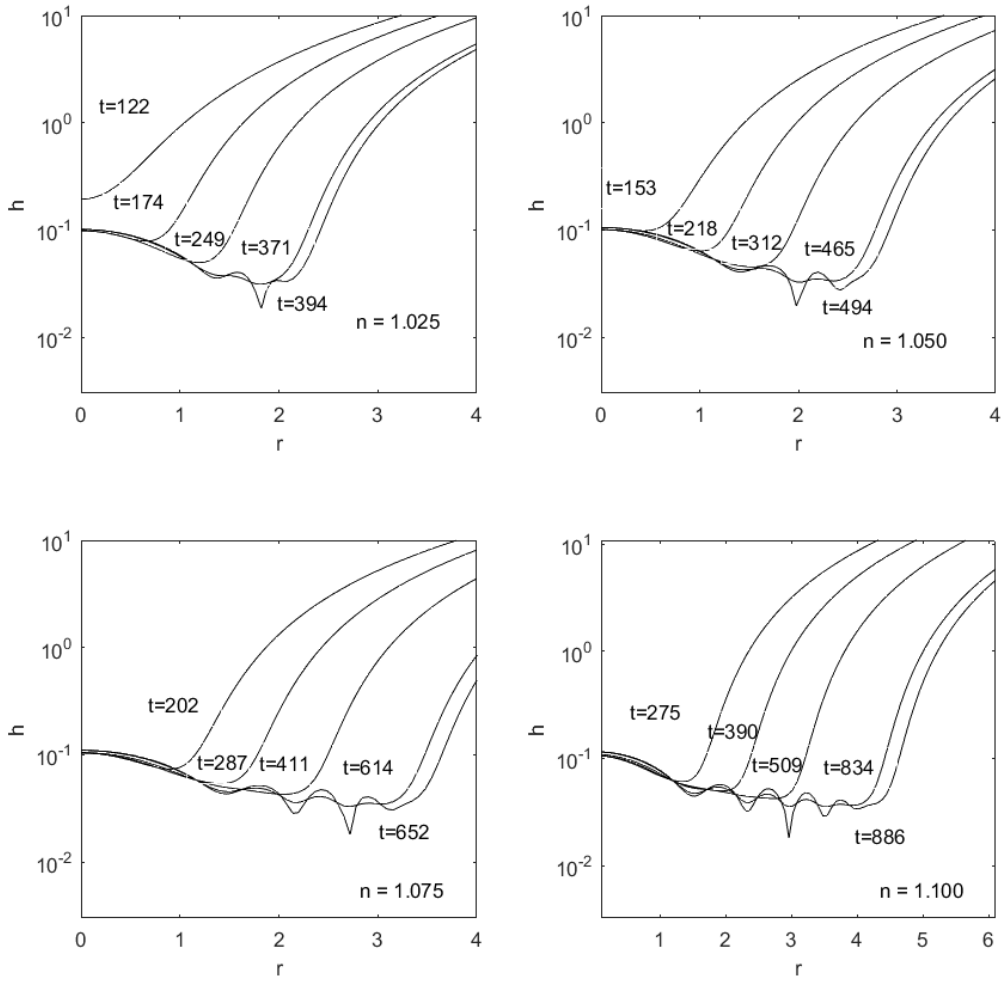

Figure 13: Time evolution of the thickness for shear-thickening fluids ($n > 1$), where $V_{app} = 0.09$, $A^* = 10^{-4}$, $h_{00} = 10$ and $r_\infty = 15$.

Figure 14 shows the time evolution of the film thickness for different values of the power index. All three drainage regimes can be detected here, and t_c increases more than three times from the smallest to the greatest value. Notice the similarities with Fig. 7 which reveals the drainage regime transitions regarding V_{app}. Thus, as also seen in Figs. 10 - 13, these transitions can stem from the value of n as well. In addition, it can be concluded that a large enough range of the power index can give drainage in all regimes for the set of parameters used here.

Figure 15 displays the time evolution of the excess pressure profiles in the film obtained for the same power index values as the film thickness profiles in Fig. 14. The excess pressure builds up in the film with time for all results, regardless of the n value or the interfacial deformation type. In case a), which corresponds to nose rupture, the maximum of each excess pressure profile is always at $r = 0$. As the film ruptures, the excess pressure profile here shows an asymptotic trend. For the other cases, the excess pressure profiles each form a maximum at the center at early stages, but with time, the

maxima appear further and further away from the center. Eventually, the locations of the maxima correspond to the rim locations observed in Fig. 14. At the final time step before the film ruptures, a sharp peak emerges for each case. These peaks represent the excess pressure at the rim locations, where the film is the thinnest, which allows the attractive molecular forces to act more severely than in any other location on the interface. Notice that in case d), a local maximum appears at the location of the secondary rim observed in Fig. 14.

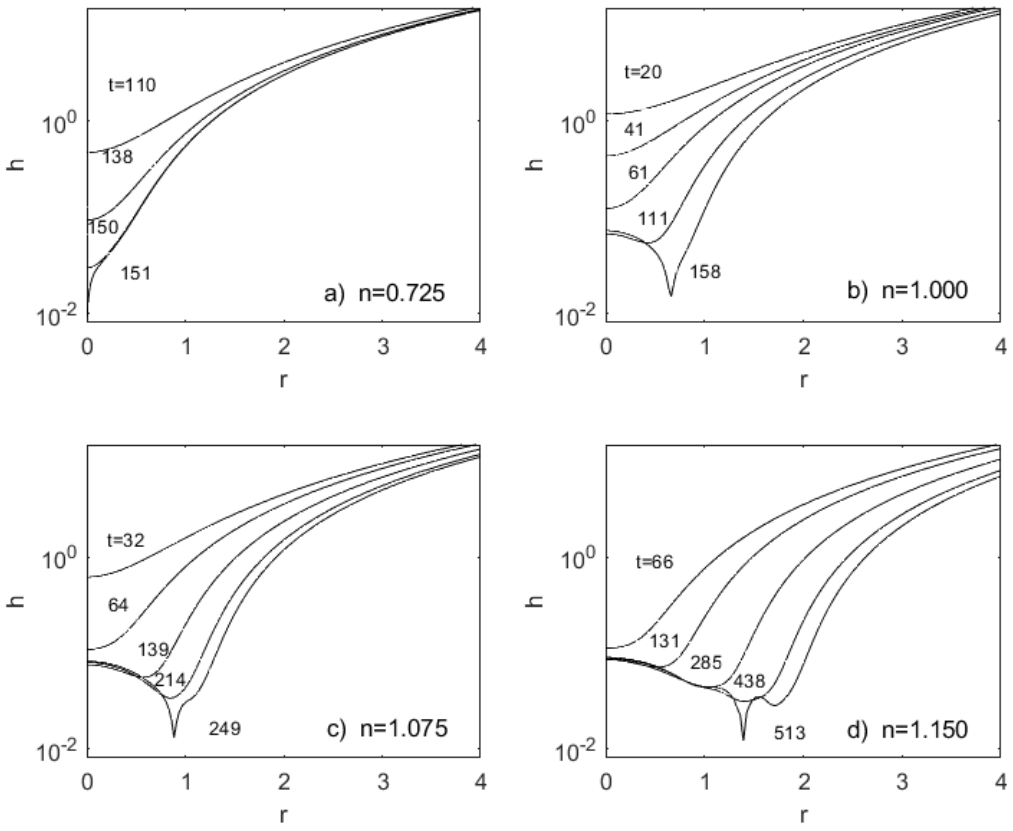

Figure 14: Time development of film thickness as a function of r for immobile interfaces obtained with $V_{app} = 0.05$, $A^* = 10^{-4}$, r_∞ = 30 and $h_{00} = 2$.

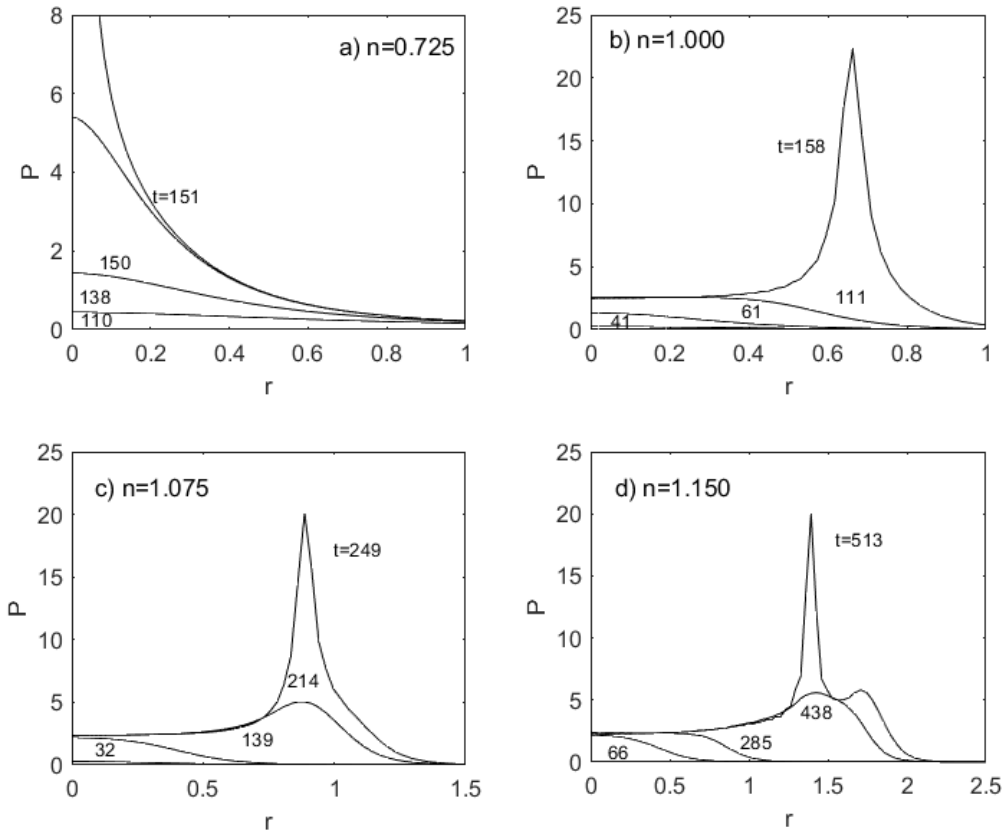

Figure 15: Time development of excess pressure as a function of r for immobile interfaces obtained with $V_{app} = 0.05$, $A^* = 10^{-4}$, $r_\infty = 30$ and $h_{00} = 2$.

Figure 16 provides the time development of the particle side tangential stress (Eq. 198) for a shear-thinning film ($n = 0.9$), and a shear-thickening one ($n = 1.1$). In Fig. 16 a), a maximum that increases with time arises in the tangential stress profiles. The corresponding viscosity profiles in Fig. 16b) forms a more and more apparent minimum with time in the same position as the tangential stress maximum. In Figs. 16 c) and d) which account for shear-thickening fluid, the opposite trend is detected. Also, here, the tangential stress profiles form a maximum, but so do the corresponding viscosity profiles. Notice the similarities between the tangential stress maximum build-up and the increasing excess pressure profile maximum (Fig. 15) with time. As for the increase in excess pressure, the tangential stress build-up also stems from the interfacial deformations. Furthermore, the tangential stress maxima closely follow the rim positions. As these positions correspond to the minimum and the maximum of η respectively for the shear-thinning and the shear-thickening film, the film drainage resistance around the rim is the lowest for shear-thinning fluids and largest for shear-thickening ones. Thus, when the film is shear-thinning, a rim can travel more easily in the positive r direction.

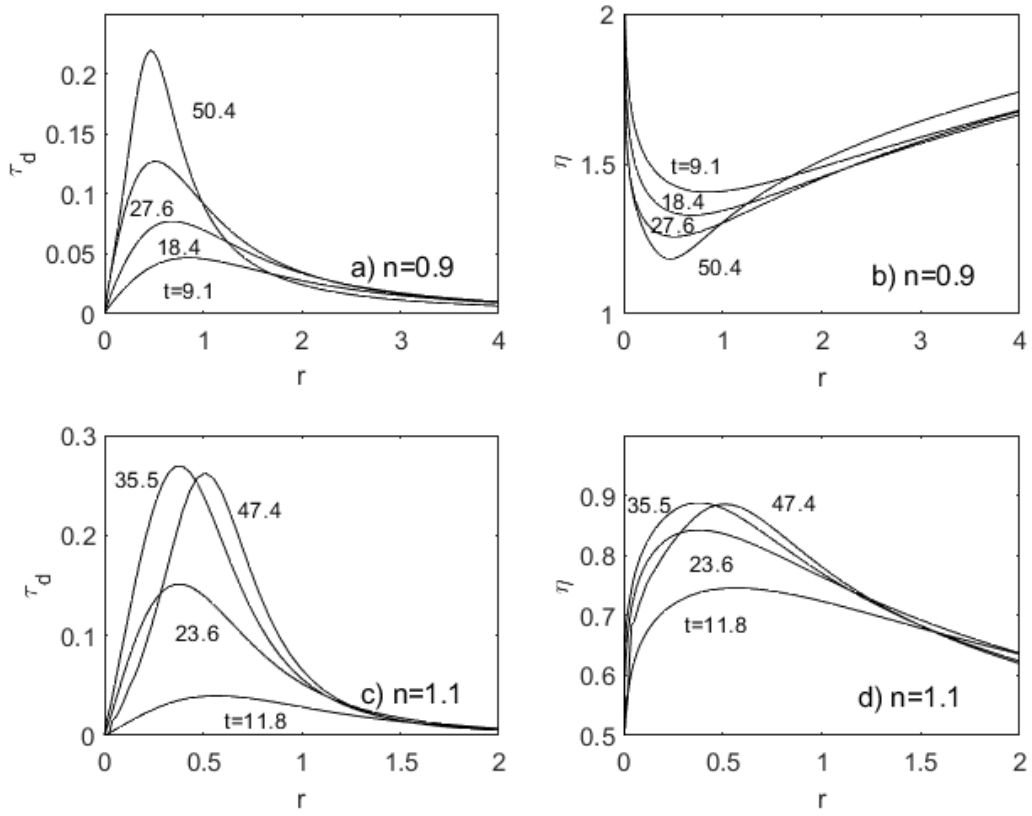

Figure 16: Time evolution of the particle side tangential stress and viscosity evaluated at the interface. The profiles are obtained with $\lambda^* = 10$, $V_{app} = 0.09$, $A^* = 10^{-4}$, r_∞ = 30 and $h_{00} = 2$.

In Fig. 17, the maximum value of the tangential velocity of the interface is shown as a function of the time for different power index values. The maximum tangential velocity can be regarded as an indicator of interface mobility, which is crucial in coalescence studies. For this particular set of parameters, in the early stages of drainage ($t = 0$ to $t \approx 25$), the maximum tangential velocity, i.e., the interface mobility, is more prominent for lower values of the power index. This result can be explained by the lower the n value is at a given shear rate, the less viscous the film is, and the interfaces are then allowed to move more quickly. After $t \approx 25$, the maximum tangential velocity curves overlap due to the difference in the interfacial deformations for the various values of n. In the end, an asymptotic slope, which indicates the film rupture, is detected for each curve. As this asymptotic trend is observed at earlier times for lower values of n, it can here be concluded that the lower the n value, the faster coalescence occurs.

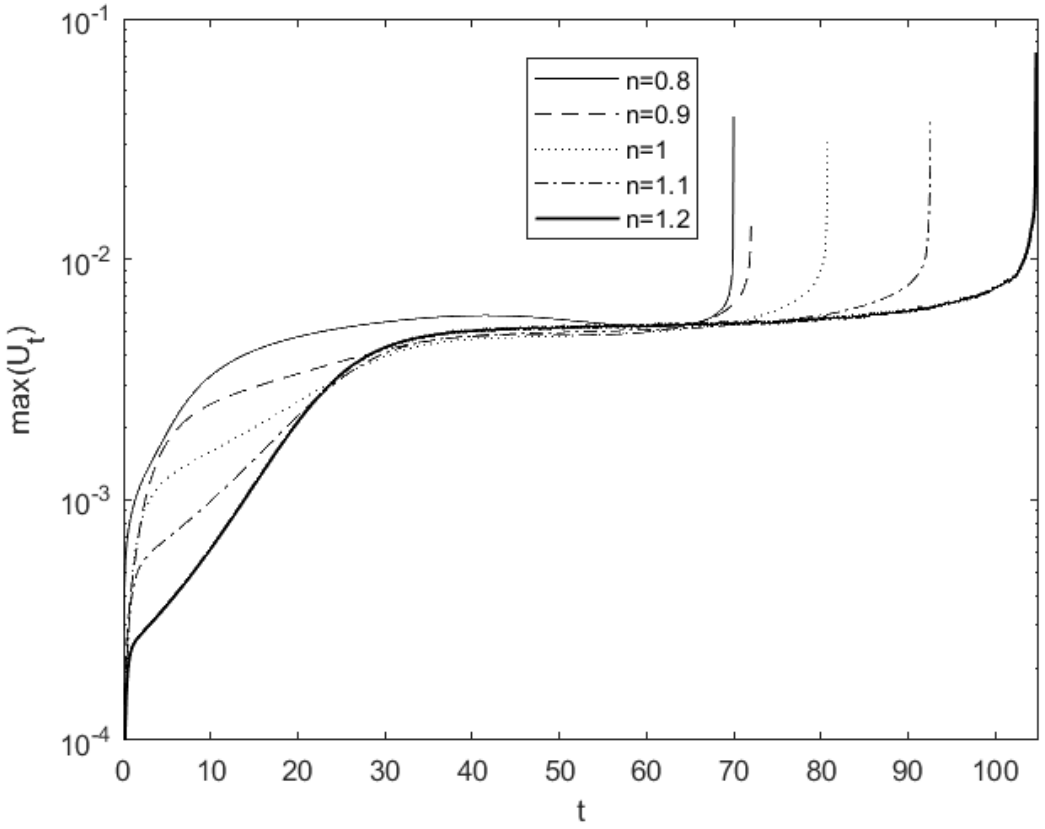

Figure 17: The maximum value of the tangential velocity of the interfaces as a function of time for different values of n. All results are obtained with λ^*=10, $A^* = 10^{-4}$, $h_{00} = 2$ and $r_\infty = 30$.

Figure 18 presents a normalized version of the coalescence time as a function of the power index for three different approach velocities resulting in curves representing each drainage regime. Here, it can be observed that the slope of the t_c curve for the low-velocity regime is very close to zero. Furthermore, for the dimpled drainage regime, a linear-like slight increasing trend is detected. Then for the multiple-rim t_c curve, a steeper linear-like trend is observed. Notice that even though these results are obtained for partially mobile interfaces, the observed effect of n on the coalescence time match well with the previously given results in Figs. 10 - 13 which show the film thickness profiles and are obtained for immobile interfaces. Together these results show that regardless of the mobility, the effect of the power index on the film drainage and the coalescence time is negligible in the low-velocity regime. Moreover, n becomes influential in the dimpled drainage regime and affects the drainage even more in the multiple-rim regime.

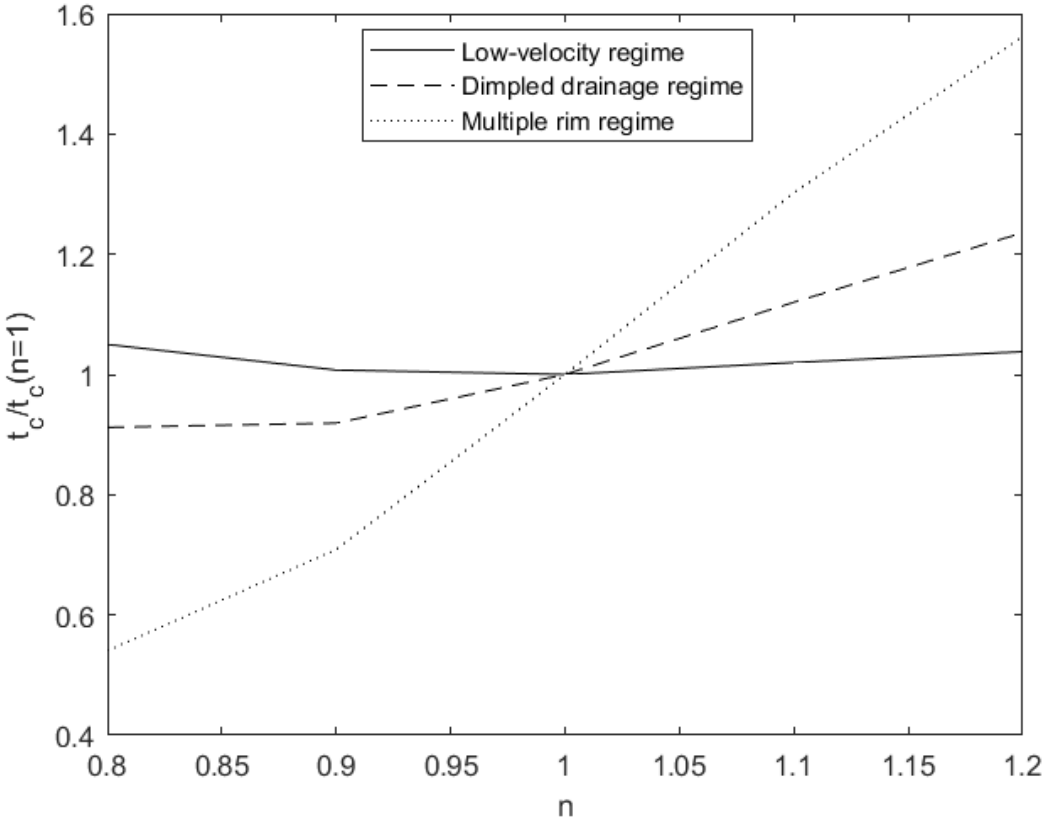

Figure 18: Coalescence time as a function of n, for $V_{app} = 0.01$ (low-velocity regime), $V_{app} = 0.06$ (dimpled drainage regime) and $V_{app} = 0.6$ (multiple-rim regime) with $\lambda^* = 10$, $A^* = 10^{-4}$, $h_{00} = 2$ and $r_\infty = 30$.

The coalescence time as a function of the relative approach velocity is provided in Figs. 19 and 20 for varying values of the power index accounting for shear-thinning, Newtonian and shear-thickening fluids. The results in Fig. 19 are obtained with the immobile solver, whereas in Fig. 20 the results are obtained by using the partially mobile solver with $\lambda^* = 10$. For low velocities, a linear decreasing relationship between $log(t_c)$ and $log(V_{app})$ is observed. Here, the t_c curves corresponding to the different values of n overlap almost completely, coinciding with the previously listed results for the low-velocity drainage regime. These results reveal that there seems to be no difference in the coalescence behavior of non-Newtonian fluids in the low-velocity regime, whether shear-thinning or shear-thickening, compared to Newtonian fluids. As V_{app} increases, the relationship between $log(t_c)$ and $log(V_{app})$ begins to deviate from the linear trend and the t_c curves start separate. Thus, the power index starts to become influential, which corresponds to the dimpled drainage regime. Notice that the higher the power index, the earlier the t_c curve deviates from the linear trend. As previously discussed, this is caused by larger n slowing down the film drainage and giving the capillary forces time to act and thus cause interface deformations. This trend also agrees with the experimental results obtained by Fan et al. (2020), which reveals that the coalescence efficiency increase with increasing CMC concentration. As it can be observed from Coulaloglou (1975)'s coalescence efficiency formula in Eq. 7, decreasing the film drainage time gives higher coalescence efficiency. Furthermore, with increasing CMC concentration, the fluid exhibits more shear-thinning behavior (Benchabane & Bekkour 2008).

Fan et al. (2020)'s results then coincide with lower n values reducing the coalescence time, or higher values of n increasing t_c. At larger V_{app}, the t_c curves pass through a minimum and start to increase, and the multiple-rim regime is reached. Here the t_c curves separate even more, which corresponds to the increasing effect of the non-Newtonian behavior on the coalescence time within this regime. As for the transition into the dimpled drainage regime, the multiple-rim regime transitions occur at lower velocities for higher power index values. By comparing the t_c curves in Figs. 19 (immobile interfaces) and 20 (partially mobile interfaces), it can be seen that the t_c curves in Fig. 19 separate to a much larger extent. Thus, the power index seems to be more influential when the interfaces are less mobile. However, Figs. 19 and 20 show the same trends overall; the effect of the non-Newtonian behavior on coalescence time amplify with increasing V_{app}.

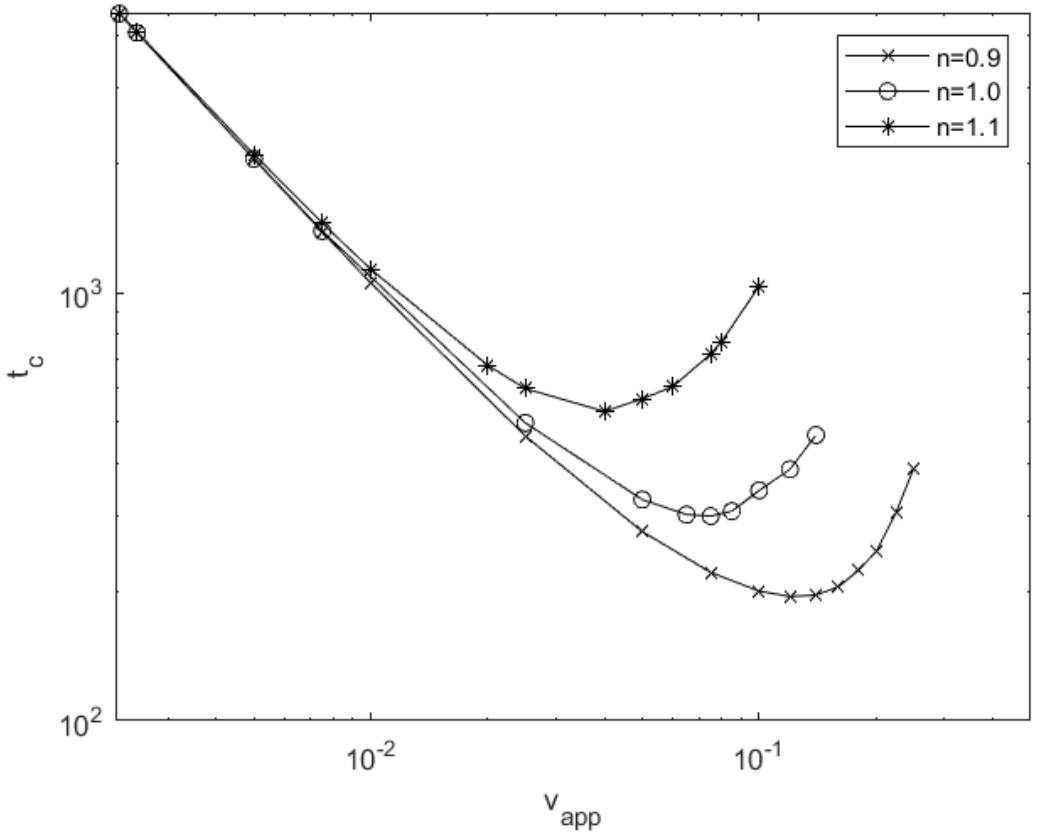

Figure 19: Coalescence time as a function of relative approach velocity for shear-thinning ($n < 1$), Newtonian ($n = 1$) and shear-thickening ($n > 1$) fluids with immobile interfaces, $A^* = 10^{-4}$, $h_{00} = 10$ and $r_\infty = 15$.

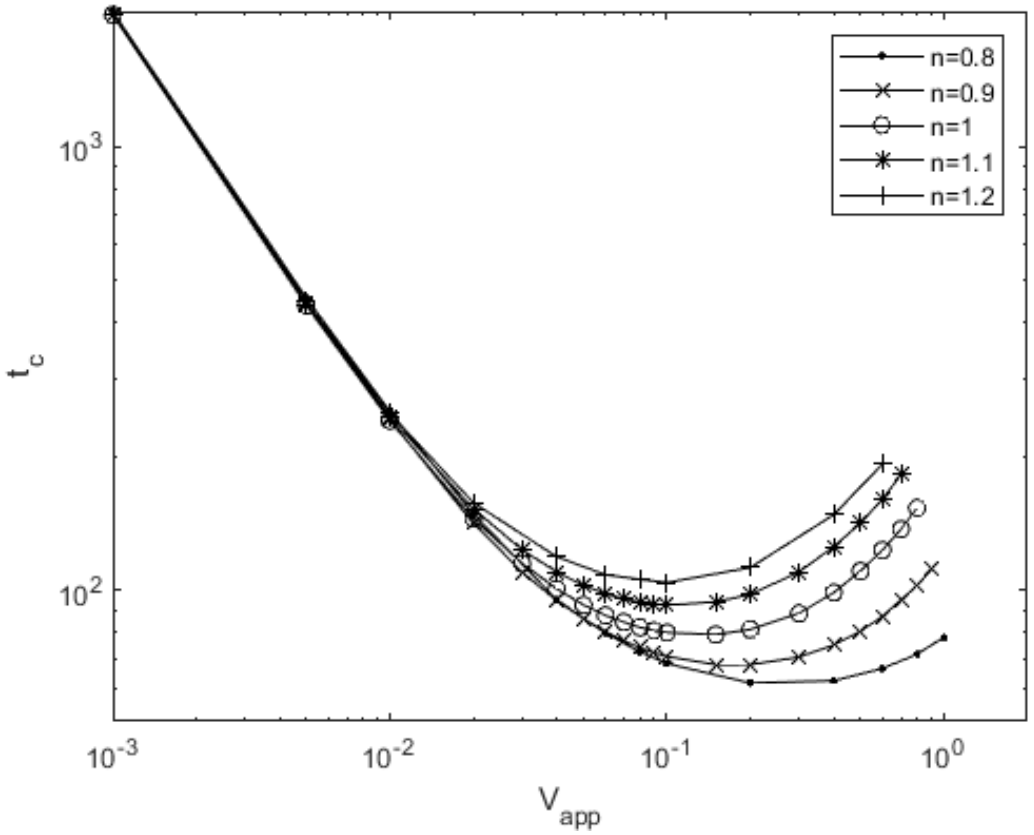

Figure 20: Coalescence time as a function of relative approach velocity for shear-thinning ($n < 1$), Newtonian ($n = 1$) and shear-thickening ($n > 1$) fluids with $\lambda^* = 10$, $A^* = 10^{-4}$, $h_{00} = 2$ and $r_\infty = 30$.

In Fig. 21, coalescence time as a function of the dispersed to continuous phase viscosity ratio for different values of the power index is presented. The results are here obtained by considering partially mobile interfaces, i.e., the thinning equation includes both the term which gives rise to a parabolic-like velocity profile and the term which yields a plug flow profile. The results are also obtained with the fully mobile and immobile solvers for the upper and lower presented values of λ^*, respectively. Here, it can be observed that the effect of n is very significant when the interfaces are considered immobile. Then, with increasing mobility, i.e., decreasing λ^*, the effect of n diminishes, and for fully mobile interfaces, n is no longer of any influence on the coalescence time. From Fig. 21, it can be observed that for λ^* values below 10^{-1}, the partially mobile solver results seem to match the fully mobile solver results. Hence, the interfaces can be regarded as fully mobile for $\lambda^* = 10^{-1}$ and below. The immobile solver results appear to match the result obtained with the partially mobile solver for $\lambda^* = 10^3$ for lower values of n, and then this limit seems to increase with increasing n. When $n = 1.1$, the interfaces appears to be completely immobilized at $\lambda^* = 10^5$.

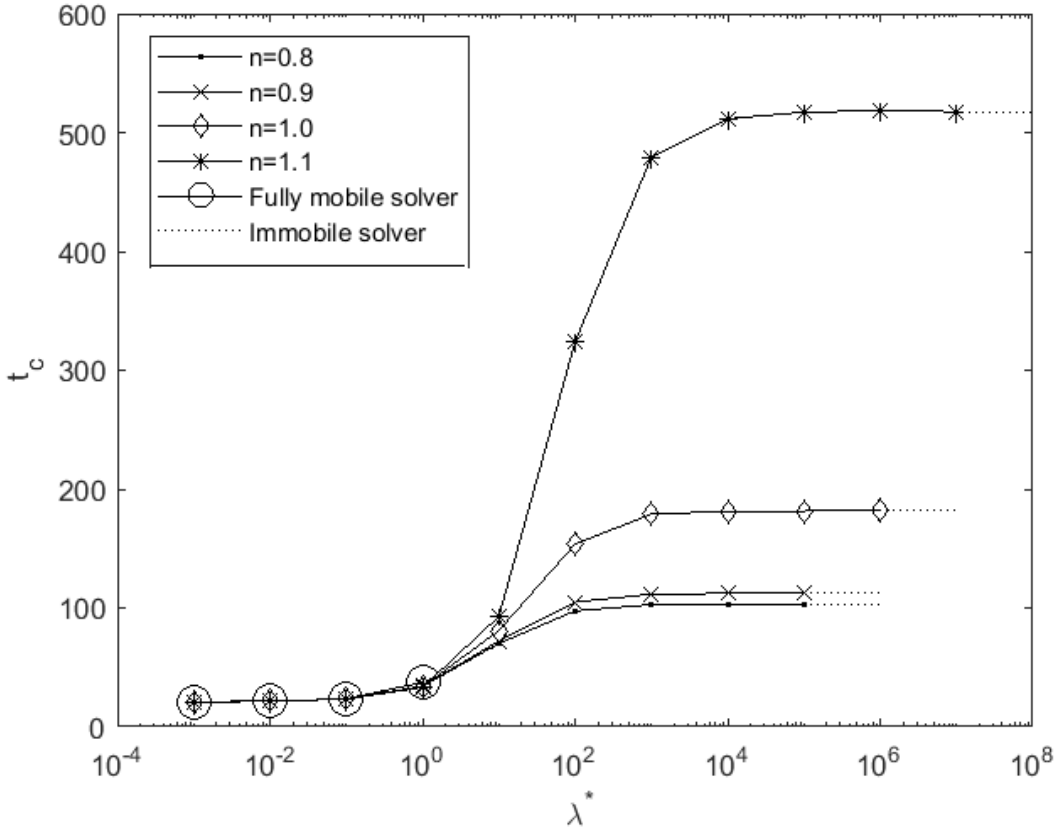

Figure 21: Coalescence time as a function of dispersed to continuous phase viscosity ratio for shear-thinning ($n = 0.8$), ($n = 0.9$), Newtonian ($n = 1.0$) and shear-thickening ($n = 1.1$) fluids with $A^* = 10^{-4}$, $h_{00} = 2$ and $r_\infty = 30$.

In Fig. 22, the coalescence time as function of V_{app} with varying λ^* values for power index values corresponding to shear-thinning ($n = 0.9$) and shear-thickening ($n = 1.1$) fluids is given. As for the last figure, the results are obtained with the partially mobile solver and matched with the fully mobile and immobile solvers for lower and upper limits of λ^*, respectively. Notice that the t_c trends coincide with those observed in Figs. 19 and 20. Hence, all three types of drainage regimes can be detected. When comparing Fig. 22a to Fig. 22b, it can be seen that the t_c curve corresponding to $\lambda^* = 100$ in Fig. 22a is closer to matching the immobile solver than in Fig. 22b. Thus, the transitions from partially mobile to immobile interfaces appear to occur for lower λ^* values for shear-thinning fluid than shear-thickening, which agrees with the results obtained in Fig. 21. Furthermore, note that the t_c curves show the same characteristic, i.e., drainage regimes, regardless of whether the fluid is shear-thinning or shear-thickening, and regardless of the extent of the interfacial mobility.

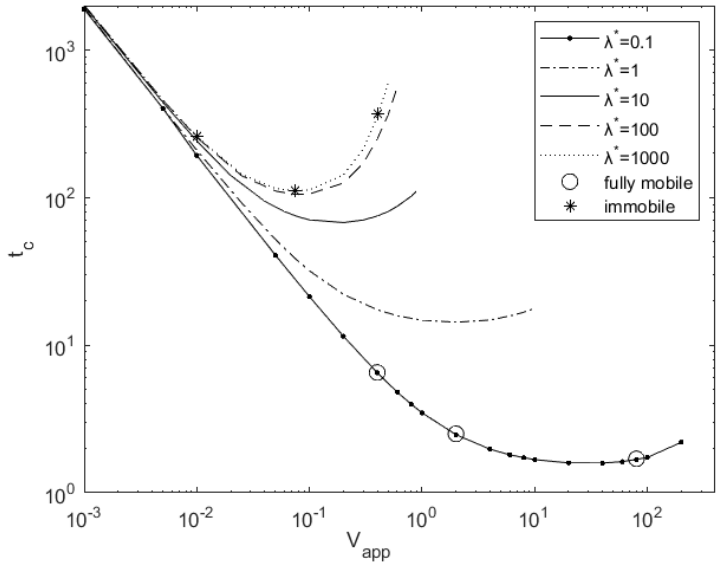

(a) $n = 0.9$

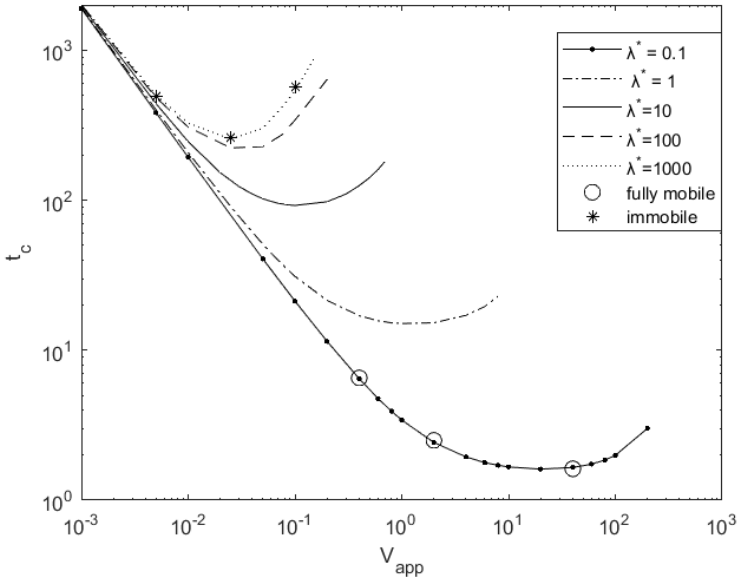

(b) $n = 1.1$

Figure 22: Coalescence time as a function of approach velocity for shear-thinning ($n = 0.9$) and shear-thickening ($n = 1.1$) fluids with $A^* = 10^{-4}$, $h_{00} = 2$ and $r_\infty = 30$.

5 Conclusions

In this thesis, the drainage of a thin non-Newtonian film entrapped between two fluid particles is investigated. The continuous phase is modeled as a generalized Newtonian fluid, and the use of the power law determines its non-Newtonian viscosity. The interfaces are considered deformable and are allowed to have any degree of tangential mobility. Through the power index, n, the effect of the non-Newtonian behavior on the film drainage and coalescence time is examined. For low approach velocities, V_{app}, there is no rim formation during the drainage, whereas increasing V_{app} results in dimple formation, i.e., formation of a single rim. Further increase of V_{app} eventually causes the emergence of multiple rims on the interfaces. It is found that the viscosity reaches its lowest value around the main rim for shear-thinning fluids, which means that the rims can travel further in the radial direction for smaller values of n. When no rims are visible at the interfaces, the non-Newtonian behavior shows no significant influence on the coalescence time, t_c. Then, with the increasing number of rims, the n value influences t_c more and more. For a fixed value of V_{app} in the dimpled or multiple-rim drainage regimes, the rate of film drainage reduces with increasing n, which results in higher t_c. This increase in t_c is found to amplify with increasing V_{app}. Lastly, the non-Newtonian behavior is most influential on the coalescence time when the interfaces are immobile. With increasing tangential mobility, n influences t_c less and less, and when the interfaces are fully mobile, the effect of n disappears completely.

As shear-thinning fluids are the most common in the industry, in most industrial multi-phase reactor models, it should be sufficient to describe the continuous phase as Newtonian if the tangential mobility of the interfaces is high and the approach velocity is low. However, for decreasing mobility and increasing V_{app}, coalescence starts to occur faster in shear-thinning fluid than in Newtonian fluid, and the non-Newtonian behavior should be taken into account.

5.1 Further work

In food processing or crop spraying, complex fluid dispersion regularly occurs, which often contains surfactants as additives or contaminants (Lu 2014). Further research might explore the effect of adding surfactants to the system. This will introduce an additional factor controlling the mobility of the interfaces.

References

Abid, S. & Chesters, A. (1994), 'The drainage and rupture of partially-mobile films between colliding drops at constant approach velocity', *International journal of multiphase flow* **20**(3), 613–629.

Acharya, A. & Ulbrecht, J. (1978), 'Note on the influence of viscoelasticity on the coalescence rate of bubbles and drops', *AIChE Journal* **24**(2), 348–351.

Al-Matroushi, E. & Borhan, A. (2009), 'Coalescence of drops and bubbles rising through a non-newtonian fluid in a tube', *Annals of the New York Academy of Sciences* **1161**(1), 225–233.

Barnes, H. A. (2000), *A handbook of elementary rheology*, Vol. 1, University of Wales, Institute of Non-Newtonian Fluid Mechanics Aberystwyth.

Bazhlekov, I., Chesters, A. & Van de Vosse, F. (2000), 'The effect of the dispersed to continuous-phase viscosity ratio on film drainage between interacting drops', *International Journal of Multiphase Flow* **26**(3), 445–466.

Benchabane, A. & Bekkour, K. (2008), 'Rheological properties of carboxymethyl cellulose (cmc) solutions', *Colloid and Polymer Science* **286**(10), 1173–1180.

Chesters, A. (1991), 'Modelling of coalescence processes in fluid-liquid dispersions: a review of current understanding', *Chemical engineering research and design* **69**(A4), 259–270.

Coulaloglou, C. (1975), Dispersed phase interactions in an agitated flow vessel. Illi-nois Institute of Technology, Chicago Ph. D, PhD thesis, thesis. Ph. D. Dissertation.

Davis, R. H., Schonberg, J. A. & Rallison, J. M. (1989), 'The lubrication force between two viscous drops', *Physics of Fluids A: Fluid Dynamics* **1**(1), 77–81.

de Waele, A. (1923), *Viscometry and plastometry*, Oil and Colour Chemists' Association.

Dekee, D., Carreau, P. & Mordarski, J. (1986), 'Bubble velocity and coalescence in viscoelastic liquids', *Chemical engineering science* **41**(9), 2273–2283.

Derjaguin, B. & Kussakov, M. (1939), 'Anomalous properties of thin polymolecular films', *Acta Physicochim. URSS* **10**(1), 25–44.

Doraiswamy, D. (2002), 'The origins of rheology: a short historical excursion', *Rheology Bulletin* **71**(1), 1–9.

Fan, W., Du, M., Sun, Y. & Chen, H. (2020), 'Coalescence characteristics of side-by-side growing bubbles in carboxymethyl cellulose solutions', *Chemical Engineering & Technology* **43**(2), 230–239.

Guo, W., Labrosse, G. & Narayanan, R. (2013), *The application of the Chebyshev-Spectral method in transport phenomena*, Springer Science & Business Media.

Johns, L. E. & Narayanan, R. (2007), *Interfacial instability*, Springer Science & Business Media.

Klaseboer, E., Chevaillier, J. P., Gourdon, C. & Masbernat, O. (2000), 'Film drainage between colliding drops at constant approach velocity: experiments and modeling', *Journal of colloid and interface science* **229**(1), 274–285.

Li, H., Mouline, Y., Choplin, L. & Midoux, N. (1997), 'Chaotic bubble coalescence in non-newtonian fluids', *International Journal of Multiphase Flow* **23**(4), 713–723.

Li, H. Z. (1999), 'Bubbles in non-newtonian fluids: Formation, interactions and coalescence', *Chemical Engineering Science* **54**(13-14), 2247–2254.

Li, H. Z., Frank, X., Funfschilling, D. & Mouline, Y. (2001), 'Towards the understanding of bubble interactions and coalescence in non-newtonian fluids: a cognitive approach', *Chemical Engineering Science* **56**(21-22), 6419–6425.

Liao, Y. & Lucas, D. (2010), 'A literature review on mechanisms and models for the coalescence process of fluid particles', *Chemical Engineering Science* **65**(10), 2851–2864.

Lin, T.-J. & Lin, G.-M. (2009), 'Mechanisms of in-line coalescence of two-unequal bubbles in a non-newtonian fluid', *Chemical Engineering Journal* **155**(3), 750–756.

Lu, J. (2014), 'Interfacial dynamics of drop coalescence and impinging liquid jets: Effect of viscous, marangoni and shear-thinning stresses'.

Ostwald, W. (1925), 'About the rate function of the viscosity of dispersed systems', *Kolloid Z* **36**, 99–117.

Ozan, S. C., Hosen, H. F. & Jakobsen, H. A. (2021), 'On the prediction of coalescence and rebound of fluid particles: A film drainage study', *International Journal of Multiphase Flow* **135**, 103521.

Ozan, S. C. & Jakobsen, H. A. (2019*a*), 'On the effect of the approach velocity on the coalescence of fluid particles', *International Journal of Multiphase Flow* **119**, 223–236.

Ozan, S. C. & Jakobsen, H. A. (2019*b*), 'On the role of the surface rheology in film drainage between fluid particles', *International Journal of Multiphase Flow* **120**, 103103.

Schowalter, W. R. (1978), *Mechanics of non-Newtonian fluids*, Pergamon.

Shinnar, R. & Church, J. M. (1960), 'Statistical theories of turbulence in predicting particle size in agitated dispersions', *Industrial & Engineering Chemistry* **52**(3), 253–256.

Sun, W., Zhu, C., Fu, T., Yang, H., Ma, Y. & Li, H. (2017), 'The minimum in-line coalescence height of bubbles in non-newtonian fluid', *International Journal of Multiphase Flow* **92**, 161–170.

Whittaker, E. (1904), 'A treatise on the analytical dynamics of particles and rigid bodies, cam'.

Worldwide, M. I. (2016), 'A basic introduction to rheology'.

Yiantsios, S. G. & Davis, R. H. (1991), 'Close approach and deformation of two viscous drops due to gravity and van der waals forces', *Journal of colloid and interface science* **144**(2), 412–433.

Zhu, C., Li, S., Fu, T. & Ma, Y. (2018), 'Velocity evolution for the coalescence of two in-line bubbles rising in non-newtonian fluids', *Theoretical Foundations of Chemical Engineering* **52**(3), 459–464.

A Tensor notation and calculus

The dot product of unit base vectors is defined by:

$$\mathbf{e}_i \cdot \mathbf{e}_j = \delta_{ij}, \tag{A.1}$$

Here, δ_{ij} is the Kronecker delta which is expressed as:

$$\delta_{ij} = \begin{cases} 1 & \text{if i = j} \\ 0 & \text{if i} \neq \text{j} \end{cases} \tag{A.2}$$

The dot product of two vectors is defined by:

$$\mathbf{v} \cdot \mathbf{w} = vw \cos \phi_{vw}, \tag{A.3}$$

where v and w is the magnitude of the two vectors $\mathbf{v}$ and $\mathbf{w}$, respectively. Furthermore, $\cos \phi_{vw}$ is the angle between the vectors.

The cross product of unit base vectors is defined by:

$$\mathbf{e}_i \times \mathbf{e}_j = \sum_{k=1}^{3} \varepsilon_{ijk} \mathbf{e}_k \tag{A.4}$$

in which ε_{ijk} is the permutation symbol given as:

$$\varepsilon_{ijk} = \begin{cases} +1 & \text{if ijk = 123 231 321} \\ -1 & \text{if ijk = 321 213 132} \\ 0 & \text{if any two indices alike} \end{cases} \tag{A.5}$$

For a cylindrical coordinate system, 1 is the radial direction, r, 2 is the angular direction θ, and 3 is the axial direction z.

The double dot product of unit base vectors is defined by:

$$\mathbf{e}_i \mathbf{e}_j : \mathbf{e}_k \mathbf{e}_l = \delta_{jk} \delta_{il}, \tag{A.6}$$

Taking the derivative of the cylindrical unit base vectors with respect to each coordinate direction yields the following results:

$$\frac{\partial \mathbf{e}_r}{\partial r} = 0, \quad \frac{\partial \mathbf{e}_r}{\partial \theta} = \mathbf{e}_\theta, \quad \frac{\partial \mathbf{e}_r}{\partial z} = 0, \quad \frac{\partial \mathbf{e}_\theta}{\partial r} = 0, \quad \frac{\partial \mathbf{e}_\theta}{\partial \theta} = -\mathbf{e}_r, \quad \frac{\partial \mathbf{e}_\theta}{\partial z} = 0, \quad \frac{\partial \mathbf{e}_z}{\partial r} = 0, \quad \frac{\partial \mathbf{e}_z}{\partial \theta} = 0, \quad \frac{\partial \mathbf{e}_z}{\partial z} = 0 \tag{A.7}$$

The nabla operator in cylindrical coordinates is defined by:

$$\nabla = \mathbf{e}_r \frac{\partial}{\partial r} + \frac{1}{r}\mathbf{e}_\theta \frac{\partial}{\partial \theta} + \mathbf{e}_z \frac{\partial}{\partial z} \tag{A.8}$$

In cylindrical coordinates the velocity vector is written as:

$$\mathbf{v} = v_r \mathbf{e}_r + v_\theta \mathbf{e}_\theta + v_z \mathbf{e}_z \tag{A.9}$$

Due to the axisymmetry in the system, the angular velocity component can be neglected. The velocity vector then reduces to:

$$\mathbf{v} = v_r \mathbf{e}_r + v_z \mathbf{e}_z \tag{A.10}$$

The dyadic product of the vector $\mathbf{v}$ with itself is given as:

$$\begin{aligned} \mathbf{vv} =& v_r v_r \mathbf{e}_r \mathbf{e}_r + v_r v_\theta \mathbf{e}_r \mathbf{e}_\theta + v_r v_z \mathbf{e}_r \mathbf{e}_z \\ & v_\theta v_r \mathbf{e}_\theta \mathbf{e}_r + v_\theta v_\theta \mathbf{e}_\theta \mathbf{e}_\theta + v_\theta v_z \mathbf{e}_\theta \mathbf{e}_z \\ & v_z v_r \mathbf{e}_z \mathbf{e}_r + v_z v_\theta \mathbf{e}_z \mathbf{e}_\theta + v_z v_z \mathbf{e}_z \mathbf{e}_z \end{aligned} \tag{A.11}$$

where all terms with v_θ cancel out due to the assumption of axisymmetry. The dyadic velocity product is then reduced to:

$$\begin{aligned} \mathbf{vv} =& v_r v_r \mathbf{e}_r \mathbf{e}_r + v_r v_z \mathbf{e}_r \mathbf{e}_z \\ & v_z v_r \mathbf{e}_z \mathbf{e}_r + v_z v_z \mathbf{e}_z \mathbf{e}_z \end{aligned} \tag{A.12}$$

A tensor in cylindrical coordinates is given as:

$$\begin{aligned} \sigma =& \sigma_{rr} \mathbf{e}_r \mathbf{e}_r + \sigma_{r\theta} \mathbf{e}_r \mathbf{e}_\theta + \sigma_{rz} \mathbf{e}_r \mathbf{e}_z \\ & \sigma_{\theta r} \mathbf{e}_\theta \mathbf{e}_r + \sigma_{\theta\theta} \mathbf{e}_\theta \mathbf{e}_\theta + \sigma_{\theta z} \mathbf{e}_\theta \mathbf{e}_z \\ & \sigma_{zr} \mathbf{e}_z \mathbf{e}_r + \sigma_{z\theta} \mathbf{e}_z \mathbf{e}_\theta + \sigma_{zz} \mathbf{e}_z \mathbf{e}_z \end{aligned} \tag{A.13}$$

The components of the viscous stress tensor that vanishes in this system assuming Assuming Newtonian continuous phase are defined as:

$$\tau_{r\theta} = \tau_{r\theta} = -\mu_c \left[r \frac{\partial}{\partial r} \left(\frac{v_\theta}{r} \right) + \frac{1}{r} \frac{\partial v_r}{\partial \theta} \right], \qquad \tau_{\theta z} = \tau_{z\theta} = -\mu_c \left[r \frac{\partial v_\theta}{\partial z} + \frac{1}{r} \frac{\partial v_z}{\partial \theta} \right] \tag{A.14}$$

The product rule of calculus is defined by:

$$(fg)' = f'g + fg' \tag{A.15}$$

in which f and g are arbitrary functions while $'$ indicates the derivative.

When a variable z depends on the variable y, which itself depends on the variable x, then z, via the intermediate variable of y, also depends on x. Thus, the chain rule of calculus gives:

$$\frac{dz}{dx} = \frac{dz}{dy}\frac{dy}{dx} \tag{A.16}$$

B Matlab code

B.1 Newtonian code

```
%Author: Maria Fanebust
%Purpose: Determine coalescence behavior for Newtonian flow
%Interface mobility: Immobile


%Step 1: Specify boundaries, number of grids, and time step

L = 0; R=15; N=60; dt = 0.005;

%Step 2: Get derivative matrix and spacing of grid points through
    Chebyshev polynomials (collocation method)

[Dc,zc] = cheb(N);

%Step 3: Linear mapping of the spacing of the grid points and the
    derivativematrix onto the domain of interest

[a,b,r] = mapping(L,R,zc);
D = a*Dc;

%Step 4: Specify physical parameters

vapp = 1;
A_star = 0;

%Step 5: Build A and RHS

h0 =10 + r.^2;              %Initial film thickness
P0 = zeros(N+1,1);          %Initial pressure

freq=1000;                  %Frequency chosen such that not every
    solution will be saved


hkm1 = h0; hk = h0;         %film thickness at step k-1 and k put
    equal to the initial film thickness before the iterations start


Pkm1 = P0; Pk = P0;         %Same procedure for pressure

hstore=[];Pstore=[];        %Lists to store thickness and pressure


for k=2:(42/dt)             %Here starts the iterations
```

```
41
42 A11 = -3/2/dt*eye(N+1,N+1);
43 A12 = 1/12*diag(1./r)*D*diag(r)*diag(hk.^3)*D;
44 A21 = -1/2*diag(1./r)*D*diag(r)*D;
45 A22 = -eye(N+1,N+1);
46
47 RHS1 = -2*hk/dt +hkm1/2/dt;
48 RHS2 = -2*ones(N+1,1) - A_star./(hk.^3);
49
50
51 A = [A11 A12; A21 A22]; RHS = [RHS1; RHS2];
52
53 %Step 6: Specify boundary conditions
54
55 A(1,:) = [ D(1,:) zeros(1,N+1)]; RHS(1) = 0;
56 A(N+1,:) = [zeros(1,N) 1 zeros(1,N+1)] ; RHS(N+1) = (-vapp + 2/dt*
       hk(N+1);
57 - 1/2/dt*hkm1(N+1))*(2*dt)/3;
58 A(N+2,:) = [zeros(1,N+1) D(1,:) ]; RHS(N+2) = 0;
59 A(2*(N+1), :) = [zeros(1,N+1) zeros(1,N) 1 ]; RHS(end) = 0;
60
61 %Step 7: Solve the numerical problem
62
63 sol=A\RHS;
64
65 hkp1 = sol(1:N+1);                          %Update film thickness and
       pressure at step k+1
66 Pkp1 = sol(N+2:end);
67
68 hkm1=hk; hk=hkp1; Pkm1=Pk; Pk=Pkp1;         %Update film thickness and
       pressure at steps k-1 and k
69
70
71
72
73 %Criterion to end the iterations once critical film thickness is
       reached
74
75 criterion = min(hkp1);
76
77  if criterion < 10^(-3)
78       break
79  end
80
81  %Save every k/freq solutions that give modulus of 2
82
83 if mod(k,freq)==2
84      min(hkp1)
```

```
85      k
86      hstore=[hstore hkp1];
87      Pstore=[Pstore Pkp1];
88  end
89
90
91  end
92
93  %Step 8: plot the solutions
94
95  semilogy(r,hstore,'k-')                %Film thickness profiles
96  xlabel("r")
97  ylabel("h")
98  figure
99  plot(r,Pstore,'k-')                    %Pressure profiles
100 xlabel("r")
101 ylabel("P")
```

B.2 Cheb function

```
1           %Generate grid points and differentiation matrix
2
3           function [D,x] = cheb(N)
4           if N==0, D=0; x=1; return, end
5
6           % Chebyshev points are given by
7           x=cos(pi*(0:N)/N)';
8
9           % Transform from [1,-1] to [-1,1]
10          x=-x;
11
12          % Differentiation matrix
13          c=[2; ones(N-1,1); 2].*(-1).^(0:N)';
14          X=repmat(x,1,N+1);
15          dX=X-X';
16          D=(c*(1./c)')./(dX+(eye(N+1)));     %off-diagonal entries
17          D=D-diag(sum(D'));                  %diagonal entrie
```

B.3 Mapping function

```
1  function [a,b,z] = mapping(L,R,zc)
2  a=2/(R-L);
3  b=1-(2*R/(R-L));
4  z=(zc-b)/a;
5
```

```
end
```

B.4 Non-Newtonian code, immobile interfaces

```
%Author: Maria Fanebust
%Purpose: Determine coalescence behavior for non-Newtonian flow
%Interface mobibility: Immobile

clc
close all
clear
warning off

%Step 1: Specify boundaries, number of grids, and time step
L = 0; R=30; N=600; dt = 0.01;

%Step 2: Get derivative matrix and spacing of grid points through Chebyshev polynomials (collocation method)
[Dc,zc] = cheb(N);

%Step 3: Linear mapping of the spacing of the grid points and the derivative matrix onto the domain of interest
[a,b,r] = mapping(L,R,zc);
D = a*Dc;
D2=D*D;



%Step 4: Specify physical parameters
vapp = 0.05;                        %Relative approach velocity
n=1;                                %Power index
A_star = 0.0001;                    %Hamaker constant


%Step 5: Build A and RHS
h0 =2 + r.^2;                     %Initial film thickness
P0 = 0.00000001*ones(N+1,1);      %Initial pressure

freq=10;                            %Frequency chosen such that not every solution will be saved


hkm1 = h0; hk = h0;                 %film thickness at step k-1 and k put equal to the initial film thickness before the iterations start

```

```
38
39 Pkm1 = P0; Pk = P0;                %Same procedure for pressure
40
41 hstore=[]; Pstore=[]; tstore=[];   %Lists to store thickness, pressure
       and time
42
43
44 t = 0;
45 tic
46 for k=2:1000000                    %Here starts the iterations
47
48 t= t +  dt;                        %Update the time step
49
50
51 A11=3/2/dt*eye(N+1,N+1);
52 A12 = n/((1+ 2*n)*(2^(1/n+1))) * diag(1./r)*D*diag(r)*diag((-D*Pk)
       .^(1/n-1))*diag(hk.^(2*n+1))*(-D);
53 A21 = 1/2*diag(1./r)*D*diag(r)*D;
54 A22 = eye(N+1,N+1);
55
56 RHS1 = 2*hk/dt -hkm1/2/dt;
57 RHS2 = 2*ones(N+1,1) + A_star./(hk.^3);
58
59
60 A = [A11 A12; A21 A22]; RHS = [RHS1; RHS2];
61
62 %Step 6: Specify boundary conditions
63 A(1,:) = [ D(1,:) zeros(1,N+1)]; RHS(1) = 0;
64 A(N+1,:) = [zeros(1,N) 1 zeros(1,N+1)] ; RHS(N+1) = (-vapp + 2/dt*
       hk(N+1)- 1/2/dt*hkm1(N+1))*(2*dt)/3;
65 A(N+2,:) = [zeros(1,N+1) D(1,:) ]; RHS(N+2) = 0;
66 A(2*(N+1), :) = [zeros(1,N+1) zeros(1,N) 1 ]; RHS(end) = 0;
67
68 %Step 7: Solve the numerical problem
69 sol=real(A\RHS);                    %Get the real solutions
70
71 hkp1 = sol(1:N+1);                  %Update film thickness
72 Pkp1 = sol(N+2:2*N+2);              %and pressure at step k+1
73
74
75 %Criterion to end the iterations once critical film thickness is
       reached
76 criterion = min(hkp1);
77
78
79 %Criterion use to obtain the last profile before the film rupture
       for when
80 %nose rupture occurs
```

```
81
82 % if criterion < 0.03
83 %     dt =0.00001;
84 % end
85
86  if criterion < 10^(-3)
87      break
88
89  end
90  hkm1=hk; hk=hkp1; Pkm1=Pk; Pk=Pkp1;      %Update film thickness and
        pressure at steps k-1 and k
91
92
93 %Save every k/freq solutions that give modulus of 2
94 if mod(k,freq)==2
95     k
96     min(hkp1)
97     t
98     hstore=[hstore hkp1];
99     Pstore=[Pstore Pkp1];
100    tstore = [tstore t];
101 end
102
103
104 end
105 toc
106 save('h02_R30_v005_n1_crit')       %Save file
107
108 %Step 8: plot the solutions
109
110 figure
111
112 %Film thickness profiles
113
114 %n=0.9, vapp =0.003
115 subplot(2,2,1)
116 semilogy(r,hstore(:,5925),'k-')
117 hold on
118 semilogy(r,hstore(:,6325),'k-')
119 hold on
120 semilogy(r,hstore(:,6725),'k-')
121 hold on
122 semilogy(r,hstore(:,end-1),'k-')
123 xlabel("r")
124 ylabel("h")
125 xlim([0 4])
126 ylim([3*10^(-3) 18])
127
```

```
128
129 %n=0.925, vapp =0.003
130 subplot(2,2,2)
131 semilogy(r,hstore(:,5920),'k-')
132 hold on
133 semilogy(r,hstore(:,6320),'k-')
134 hold on
135 semilogy(r,hstore(:,6720),'k-')
136 hold on
137 semilogy(r,hstore(:,end-1),'k-')
138 xlabel("r")
139 ylabel("h")
140 xlim([0 4])
141 ylim([3*10^(-3) 18])
142
143
144
145 %n=0.95, vapp =0.003
146 subplot(2,2,3)
147 semilogy(r,hstore(:,5918),'k-')
148 hold on
149 semilogy(r,hstore(:,6318),'k-')
150 hold on
151 semilogy(r,hstore(:,6718),'k-')
152 hold on
153 semilogy(r,hstore(:,end-1),'k-')
154 xlabel("r")
155 ylabel("h")
156 xlim([0 4])
157 ylim([3*10^(-3) 18])
158
159 %n=0.975, vapp =0.003
160 subplot(2,2,4)
161 semilogy(r,hstore(:,5918),'k-')
162 hold on
163 semilogy(r,hstore(:,6318),'k-')
164 hold on
165 semilogy(r,hstore(:,6718),'k-')
166 hold on
167 semilogy(r,hstore(:,end-1),'k-')
168 xlabel("r")
169 ylabel("h")
170 xlim([0 4])
171 ylim([3*10^(-3) 18])
172
173 %n=1.025, vapp=0.003
174 subplot(2,2,1)
175 semilogy(r,hstore(:,5927),'k-')
```

```
hold on
semilogy(r,hstore(:,6328),'k-')
hold on
semilogy(r,hstore(:,6728),'k-')
hold on
semilogy(r,hstore(:,end-1),'k-')
xlabel("r")
ylabel("h")
xlim([0 4])
ylim([3*10^(-3) 18])


%n=1.05, vapp=0.003
subplot(2,2,2)
semilogy(r,hstore(:,5935),'k-')
hold on
semilogy(r,hstore(:,6336),'k-')
hold on
semilogy(r,hstore(:,6737),'k-')
hold on
semilogy(r,hstore(:,end-1),'k-')
xlabel("r")
ylabel("h")
xlim([0 4])
ylim([3*10^(-3) 18])


%n=1.1, vapp=0.003
subplot(2,2,4)
semilogy(r,hstore(:,5967),'k-')
hold on
semilogy(r,hstore(:,6370),'k-')
hold on
semilogy(r,hstore(:,6772),'k-')
hold on
semilogy(r,hstore(:,end-1),'k-')
xlabel("r")
ylabel("h")
xlim([0 4])
ylim([3*10^(-3) 18])


%n=1.025, vapp = 0.009
subplot(2,2,1)
semilogy(r,hstore(:,1912),'k-')
hold on
semilogy(r,hstore(:,2135),'k-')
hold on
```

```
224 semilogy(r,hstore(:,2313),'k-')
225 hold on
226 semilogy(r,hstore(:,end-1),'k-')
227 xlabel("r")
228 ylabel("h")
229 xlim([0 4])
230 ylim([3*10^(-3) 18])
231
232 %n=1.05, vapp = 0.009
233 subplot(2,2,2)
234 semilogy(r,hstore(:,1934),'k-')
235 hold on
236 semilogy(r,hstore(:,2159),'k-')
237 hold on
238 semilogy(r,hstore(:,2339),'k-')
239 hold on
240 semilogy(r,hstore(:,end-1),'k-')
241 xlabel("r")
242 ylabel("h")
243 xlim([0 4])
244 ylim([3*10^(-3) 18])
245
246 %n=1.075, vapp = 0.009
247 subplot(2,2,3)
248 semilogy(r,hstore(:,1961),'k-')
249 hold on
250 semilogy(r,hstore(:,2188),'k-')
251 hold on
252 semilogy(r,hstore(:,2371),'k-')
253 hold on
254 semilogy(r,hstore(:,end-1),'k-')
255 xlabel("r")
256 ylabel("h")
257 xlim([0 4])
258 ylim([3*10^(-3) 18])
259
260 %n=1.1, vapp = 0.009
261 subplot(2,2,4)
262 semilogy(r,hstore(:,1995),'k-')
263 hold on
264 semilogy(r,hstore(:,2227),'k-')
265 hold on
266 semilogy(r,hstore(:,2413),'k-')
267 hold on
268 semilogy(r,hstore(:,end-1),'k-')
269 xlabel("r")
270 ylabel("h")
271 xlim([0 4])
```

```
ylim([3*10^(-3)  18])

%n=0.9,  vapp=0.09
subplot(2,2,1)
semilogy(r,hstore(:,127),'k-')
hold on
semilogy(r,hstore(:,183),'k-')
hold on
semilogy(r,hstore(:,261),'k-')
hold on
semilogy(r,hstore(:,390),'k-')
hold on
semilogy(r,hstore(:,end-1),'k-')
xlabel("r")
ylabel("h")
xlim([0  4])
ylim([3*10^(-3)  10])


%n=0.925,  vapp  =0.09
subplot(2,2,2)
semilogy(r,hstore(:,136),'k-')
hold on
semilogy(r,hstore(:,194),'k-')
hold on
semilogy(r,hstore(:,277),'k-')
hold on
semilogy(r,hstore(:,414),'k-')
hold on
semilogy(r,hstore(:,end-1),'k-')
xlabel("r")
ylabel("h")
xlim([0  4])
ylim([3*10^(-3)  10])

%n=0.95,  vapp=0.09
subplot(2,2,3)
semilogy(r,hstore(:,148),'k-')
hold on
semilogy(r,hstore(:,210),'k-')
hold on
semilogy(r,hstore(:,301),'k-')
hold on
semilogy(r,hstore(:,448),'k-')
hold on
semilogy(r,hstore(:,end-1),'k-')
xlabel("r")
ylabel("h")
```

```
320 xlim([0  4])
321 ylim([3*10^(-3)  10])
322
323 %n=0.975,  vapp  =0.09
324 subplot(2,2,4)
325 semilogy(r,hstore(:,166),'k-')
326 hold on
327 semilogy(r,hstore(:,235),'k-')
328 hold on
329 semilogy(r,hstore(:,336),'k-')
330 hold on
331 semilogy(r,hstore(:,502),'k-')
332 hold on
333 semilogy(r,hstore(:,end-1),'k-')
334 xlabel("r")
335 ylabel("h")
336 xlim([0  4])
337 ylim([3*10^(-3)  10])
338
339 %n=1.025,  vapp=0.09
340 subplot(2,2,1)
341 semilogy(r,hstore(:,245),'k-')
342 hold on
343 semilogy(r,hstore(:,348),'k-')
344 hold on
345 semilogy(r,hstore(:,498),'k-')
346 hold on
347 semilogy(r,hstore(:,743),'k-')
348 hold on
349 semilogy(r,hstore(:,end-1),'k-')
350 xlabel("r")
351 ylabel("h")
352 xlim([0  4])
353 ylim([3*10^(-3)  10])
354
355 %n=1.05,  vapp  =0.09
356 subplot(2,2,2)
357 semilogy(r,hstore(:,307),'k-')
358 hold on
359 semilogy(r,hstore(:,436),'k-')
360 hold on
361 semilogy(r,hstore(:,624),'k-')
362 hold on
363 semilogy(r,hstore(:,931),'k-')
364 hold on
365 semilogy(r,hstore(:,end-1),'k-')
366 xlabel("r")
367 ylabel("h")
```

```
368 xlim([0  4])
369 ylim([3*10^(-3)  10])
370
371 %n=1.075,  vapp  =0.09
372 subplot(2,2,3)
373 semilogy(r,hstore(:,405),'k-')
374 hold on
375 semilogy(r,hstore(:,575),'k-')
376 hold on
377 semilogy(r,hstore(:,823),'k-')
378 hold on
379 semilogy(r,hstore(:,1228),'k-')
380 hold on
381 semilogy(r,hstore(:,end-1),'k-')
382 xlabel("r")
383 ylabel("h")
384 xlim([0  4])
385 ylim([3*10^(-3)  10])
386
387 %n=1.1,  vapp=0.09
388 subplot(2,2,4)
389 semilogy(r,hstore(:,550),'k-')
390 hold on
391 semilogy(r,hstore(:,781),'k-')
392 hold on
393 semilogy(r,hstore(:,1118),'k-')
394 hold on
395 semilogy(r,hstore(:,1668),'k-')
396 hold on
397 semilogy(r,hstore(:,end-1),'k-')
398 xlabel("r")
399 ylabel("h")
400 xlim([0  6])
401 ylim([3*10^(-3)  10])
402
403 %Low-velocity  regime
404 subplot(2,2,1)
405 semilogy(r,hstore(:,round(0.2*(end-1))),'k-')
406 hold on
407 semilogy(r,hstore(:,round(0.25*(end-1))),'k-')
408 hold on
409 semilogy(r,hstore(:,round(0.3*(end-1))),'k-')
410 hold on
411 semilogy(r,hstore(:,end-1),'k-')
412 xlabel("r")
413 ylabel("h")
414 xlim([0  4])
415 ylim([8*10^(-3)  15])
```

```
416
417 %Pressure profiles
418 subplot(2,2,1)
419 plot(r,Pstore(:,round(0.2*(end-1))),'k-')
420 hold on
421 plot(r,Pstore(:,round(0.25*(end-1))),'k-')
422 hold on
423 plot(r,Pstore(:,round(0.3*(end-1))),'k-')
424 hold on
425 plot(r,Pstore(:,end-1),'k-')
426 xlabel("r")
427 ylabel("P")
428 xlim([0 1])
429 ylim([0 8])
430
431
432
433 %dimpled regime
434 subplot(2,2,2)
435 semilogy(r,hstore(:,round(0.128*(end-1))),'k-')
436 hold on
437 semilogy(r,hstore(:,round(0.256*(end-1))),'k-')
438 hold on
439 semilogy(r,hstore(:,round(0.554*(end-1))),'k-')
440 hold on
441 semilogy(r,hstore(:,round(0.7*(end-1))),'k-')
442 hold on
443 semilogy(r,hstore(:,end-1),'k-')
444 xlabel("r")
445 ylabel("h")
446 xlim([0 4])
447 ylim([8*10^(-3) 15])
448
449 %Pressure
450 subplot(2,2,2)
451 plot(r,Pstore(:,round(0.128*(end-1))),'k-')
452 hold on
453 plot(r,Pstore(:,round(0.256*(end-1))),'k-')
454 hold on
455 plot(r,Pstore(:,round(0.384*(end-1))),'k-')
456 hold on
457 plot(r,Pstore(:,round(0.7*(end-1))),'k-')
458 hold on
459 plot(r,Pstore(:,end-1),'k-')
460 xlabel("r")
461 ylabel("h")
462 xlim([0 1])
463 ylim([0 15])
```

```
464
465
466 %multiple-rim regime
467
468 semilogy(r,hstore(:,round(0.128*(end-1))),'k-')
469 hold on
470 semilogy(r,hstore(:,round(0.256*(end-1))),'k-')
471 hold on
472 semilogy(r,hstore(:,round(0.554*(end-1))),'k-')
473 hold on
474 semilogy(r,hstore(:,round(0.853*(end-1))),'k-')
475 hold on
476 semilogy(r,hstore(:,end-1),'k-')
477 xlabel("r")
478 ylabel("h")
479 xlim([0 4])
480 ylim([8*10^(-3) 15])
481
482
483 %tau eta plot
484
485 subplot(2,2,1)
486 plot(r,taud(:,round(0.128*(end-1))),'k-')
487 hold on
488 plot(r,taud(:,round(0.256*(end-1))),'k-')
489 hold on
490 plot(r,taud(:,round(0.384*(end-1))),'k-')
491 hold on
492 plot(r,taud(:,round(0.7*(end-1))),'k-')
493 hold on
494 plot(r,taud(:,end-1),'k-')
495 xlabel("r")
496 ylabel("_d ")
497 xlim([0 4])
498 ylim([0 0.25])
499
500 %Tau
501 subplot(2,2,3)
502 plot(r,taud3(:,round(0.128*(end-1))),'k-')
503 hold on
504 plot(r,taud3(:,round(0.256*(end-1))),'k-')
505 hold on
506 plot(r,taud3(:,round(0.384*(end-1))),'k-')
507 hold on
508 plot(r,taud3(:,round(0.512*(end-1))),'k-')
509 hold on
510 plot(r,taud3(:,end-1),'k-')
511 xlabel("r")
```

```
512 ylabel(" _d ")
513 xlim([0 2])
514 ylim([0 0.3])
515
516 subplot(2,2,4)
517 plot(r,eta2(:,round(0.128*(end-1))),'k-')
518 hold on
519 plot(r,eta2(:,round(0.256*(end-1))),'k-')
520 hold on
521 plot(r,eta2(:,round(0.384*(end-1))),'k-')
522 hold on
523 plot(r,eta2(:,round(0.7*(end-1))),'k-')
524 xlabel("r")
525 ylabel("\eta")
526 xlim([0 2])
527 ylim([0.5 1])
```

B.5 Non-Newtonian code, partially mobile interfaces

```
1 %Author: Maria Fanebust
2 %Purpose: Determine coalescence behavior for non-Newtonian flow
3 %Interface mobility: Partially mobile
4
5 clc
6 close all
7 clear
8 warning off
9
10 %Step 1: Specify boundaries, number of grids, and time step
11 L = 0; R=30; N=600; dt = 0.0001;
12
13 %Step 2: Get derivative matrix and spacing of grid points through
     Chebyshev polynomials (collocation method)
14 [Dc,zc] = cheb(N);
15
16 %Step 3: Linear mapping of the spacing of the grid points and the
     derivative matrix onto the domain of interest
17 [a,b,r] = mapping(L,R,zc);
18 D = a*Dc;
19 D2=D*D;
20
21 rlarge=R;
22
23 ep=10^-4.2;
24
25
```

```

%Step 4: Specify physical parameters
vapp = 200;                        %Relative approach velocity
n=1.1;                              %Power index
A_star = 0.0001;                    %Hamaker constant
lambda=0.01;

%Step 5: Build A and RHS



h0 =2 + r.^2;                     %Initial film thickness
P0 = 0.00000001*ones(N+1,1);     %Initial pressure

freq=10;                           %Frequency chosen such that not every solution will be saved

hkm1 = h0; hk = h0;                %film thickness at step k-1 and k put equal to the initial film thickness before the iterations start


Pkm1 = P0; Pk = P0;                %Same procedure for pressure

hstore=[];Pstore=[];tstore=[]; Ustore=[];crit_store=[]; %Lists to store thickness, pressure and time


t = 0;

%%%%%%%%%%%%%%%%%%%%%%%%%%%%%%%%%%%%%%%%%%%%%%%%%%%%%%%%%%%%%%%%%%%%%%%%%%%%%%%%%%%
% This is the part where the integration matrix is calculated
% It is called AA in the code
% AA is only a function of number grids
% This means we can run it once for N = some number of grid points
% Then store it and just load the stored file at the beginning of the code
% For example if we save the workspace as 'integration matrix'
% Just type load('integration matrix') in the beginning of the code and
% AA should appear there automatically

[Zcheb,rhoI] = newforBIMnonsing(r,ep);


cc = ones(N+1,1);

    cc(1)=2;
```

```

    cc(N+1)=2;

    for mm = 0:N

        for nn = 0:N

            invT(mm+1,nn+1) = 2*(-1)^mm*cos(mm*nn*pi/N)/(N*cc(mm+1)*cc(nn+1));

        end

    end

    weights=zeros(N+1,1);
for j=1:N+1
for i=1:2:length(invT)
weights(j)=weights(j)-2*invT(i,j)/((i-1)^2-1);
end
end
weights=weights/a;
W=repmat(weights,1,N+1)';
AA=Zcheb.*W/2/pi;
% end
%%%%%%%%%%%%%%%%%%%%%%%%%%%%%%%%%%%%%%%%%%%%%%%%%%%%%%%%%%%%%%%%%%%%%%%%%%%%%%%%%%
tic
for k=2:2000000                    %Here starts the iterations

t= t +  dt;                        %Update time step



A11 = 3/2/dt*eye(N+1,N+1);
A12 = n/((1+ 2*n)*(2^(1/n+1)))*diag(1./r)*D*diag(r)*diag((-D*Pk).^(1/n-1))*diag(hk.^(2*n+1))*(-D);
A13 = diag(1./r)*D*diag(r.*hk);
A21 = 1/2*diag(1./r)*D*diag(r)*D;
A22 = eye(N+1,N+1);
A23 = zeros(N+1,N+1);
A31 = zeros(N+1,N+1);
A32 = 1/lambda*AA*diag(hk/2)*D;
A33 = eye(N+1,N+1);


RHS1 = 2*hk/dt -hkm1/2/dt;
RHS2 = 2*ones(N+1,1) + A_star./(hk.^3);
RHS3 = zeros(N+1,1);

```

```
114
115 A = [A11 A12 A13; A21 A22 A23; A31 A32 A33]; RHS = [RHS1; RHS2;
      RHS3];
116
117 %Step 6: Specify boundary conditions
118 A(1,:)=[D(1,:) zeros(1,2*(N+1))];RHS(1)=0;
119 A(N+1,:)=[zeros(1,N) 1 zeros(1,2*(N+1))] ; RHS(N+1) = (-vapp + 2/dt
      *hk(N+1)- 1/2/dt*hkm1(N+1))*(2*dt)/3;
120 A(N+2,:)=[zeros(1,N+1) D(1,:) zeros(1,N+1)];RHS(N+2)=0;
121 A(2*N+3,:)=[zeros(1,2*(N+1)) 1 zeros(1,N)];RHS(2*N+3)=0;
122 A(2*N+2,:)=[zeros(1,2*N+1) 1 zeros(1,N+1)];RHS(2*N+2)=0;
123
124
125 %Step 7: Solve the numerical problem
126 sol=real(A\RHS);                    %Get the real solutions
127
128 hkp1 = sol(1:N+1);                  %Update film thickness
129 Pkp1 = sol(N+2:2*N+2);              %and pressure at step k+1
130 U_stark1 = sol(2*N+3:end);          %and also the tangential velocity
131
132 %Criterion to end the iterations once critical film thickness is
      reached
133 criterion = min(hkp1);
134
135  if criterion < 10^(-3)
136      break
137
138  end
139  hkm1=hk; hk=hkp1; Pkm1=Pk; Pk=Pkp1;      %Update film thickness and
       pressure at steps k-1 and k
140
141
142
143
144 if mod(k,freq)==2                        %Get every solution where
      the modulus of freq = 2
145      k
146      min(hkp1)
147      t
148      hstore=[hstore hkp1];
149      Pstore=[Pstore Pkp1];
150      tstore = [tstore t];
151      Ustore = [Ustore U_stark1];
152      crit_store=[crit_store criterion];
153 end
154
155 end
156
```

```
toc
save('partially_n11_lambda001_v200')                    %Save file

%Step 8: plot the solutions


%Plot film thickness
figure
semilogy(r,hstore(:,round(0.6*(end-1))),'k-')
hold on
semilogy(r,hstore(:,round(0.7*(end-1))),'k-')
hold on
semilogy(r,hstore(:,round(0.8*(end-1))),'k-')
hold on
semilogy(r,hstore(:,round(0.9*(end-1))),'k-')
hold on
semilogy(r,hstore(:,end-1),'k-')
xlabel("r")
ylabel("h")
xlim([0 4])
ylim([3*10^(-3) 15])

xlim([0 105])

for i=1:lenght(tstore)
    Umax(i)=max(Ustore(:,i))  %Get the maximum velocity
end

%Umax plot
semiylog(tstore,Umax(i) %for each power index
xlabel("t")
ylabel("max(U_t)")
```

B.6 Non-Newtonian code, fully mobile interfaces

```
%Author: Maria Fanebust
%Purpose: Determine coalescence behavior for non-Newtonian flow
%Interface mobility: Fully mobile

clc
close all
clear
warning off

%Step 1: Specify boundaries, number of grids, and time step
L = 0; R=30; N=300; dt = 0.001;
```

```
12
13 %Step 2: Get derivative matrix and spacing of grid points through
       Chebyshev polynomials (collocation method)
14 [Dc,zc] = cheb(N);
15
16 %Step 3: Linear mapping of the spacing of the grid points and the
       derivative matrix onto the domain of interest
17 [a,b,r] = mapping(L,R,zc);
18 D = a*Dc;
19 D2=D*D;
20
21 rlarge=R;
22
23 ep=10^-4.2;
24
25
26
27 %Step 4: Specify physical parameters
28 vapp_lambda = 1;                        %The relative approach
       velocity and lambda are given in the same Parameter
29
30 A_star = 0.0001;                       %Hamaker constant
31
32
33
34 %Step 5: Build A and RHS
35
36
37 h0 =2 + r.^2;                       %Initial film thickness
38 P0 = 0.00000001*ones(N+1,1);     %Initial pressure
39
40 freq=10;                            %Frequency chosen such that not
       every solution will be saved
41
42
43 hkm1 = h0; hk = h0;                 %film thickness at step k-1 and k
       put equal to the initial film thickness before the iterations
       start
44
45
46 Pkm1 = P0; Pk = P0;                 %Same procedure for pressure
47
48 hstore=[]; Pstore=[]; tstore=[]; Ustore=[]; %Lists to store thickness
       , pressure, time and tangential velocity
49
50
51
52 t = 0;                                        % Initial time
```

```

%%%%%%%%%%%%%%%%%%%%%%%%%%%%%%%%%%%%%%%%%%%%%%%%%%%%%%%%%%%%%%%%%%%%%%%%%%%%%%%%%%%%%%%%%%
% This is the part where the integration matrix is calculated
% It is called AA in the code
% AA is only a function of number grids
% This means we can run it once for N = some number of grid points
% Then store it and just load the stored file at the beginning of the code
% For example if we save the workspace as 'integration matrix'
% Just type load('integration matrix') in the beginning of the code and
% AA should appear there automatically

[Zcheb,rhoI] = newforBIMnonsing(r,ep);


cc = ones(N+1,1);

    cc(1)=2;

    cc(N+1)=2;

    for mm = 0:N

        for nn = 0:N

            invT(mm+1,nn+1) = 2*(-1)^mm*cos(mm*nn*pi/N)/(N*cc(mm+1)*cc(nn+1));

        end

    end

    weights=zeros(N+1,1);
for j=1:N+1
for i=1:2:length(invT)
weights(j)=weights(j)-2*invT(i,j)/((i-1)^2-1);
end
end
weights=weights/a;
W=repmat(weights,1,N+1)';
AA=Zcheb.*W/2/pi;
% end
%%%%%%%%%%%%%%%%%%%%%%%%%%%%%%%%%%%%%%%%%%%%%%%%%%%%%%%%%%%%%%%%%%%%%%%%%%%%%%%%%%%%%%%%%%
tic
for k=2:2000000                  %Here starts the iterations

t= t + dt;                       %Update time step
```

```
98
99
100 A11 = 3/2/dt*eye(N+1,N+1);
101 A12 = zeros(N+1,N+1);
102 A13 = diag(1./r)*D*diag(r.*hk);
103 A21 = 1/2*diag(1./r)*D*diag(r)*D;
104 A22 = eye(N+1,N+1);
105 A23 = zeros(N+1,N+1);
106 A31 = zeros(N+1,N+1);
107 A32 = AA*diag(hk/2)*D;
108 A33 = eye(N+1,N+1);
109
110
111 RHS1 = 2*hk/dt -hkm1/2/dt;
112 RHS2 = 2*ones(N+1,1) + A_star./(hk.^3);
113 RHS3 = zeros(N+1,1);
114
115
116 A = [A11 A12 A13; A21 A22 A23; A31 A32 A33]; RHS = [RHS1; RHS2;
      RHS3];
117
118 %Step 6: Specify boundary conditions
119 A(1,:)=[D(1,:) zeros(1,2*(N+1))];RHS(1)=0;
120 A(N+1,:)=[zeros(1,N) 1 zeros(1,2*(N+1))] ; RHS(N+1) = (-vapp_lambda
       + 2/dt*hk(N+1)- 1/2/dt*hkm1(N+1))*(2*dt)/3;
121 A(N+2,:)=[zeros(1,N+1) D(1,:) zeros(1,N+1)];RHS(N+2)=0;
122 A(2*N+3,:)=[zeros(1,2*(N+1)) 1 zeros(1,N)];RHS(2*N+3)=0;
123 A(2*N+2,:)=[zeros(1,2*N+1) 1 zeros(1,N+1)];RHS(2*N+2)=0;
124
125
126 %Step 7: Solve the numerical problem
127 sol=real(A\RHS);                    %Get the real solutions
128
129 hkp1 = sol(1:N+1);                  %Update film thickness, pressure
      and tangential velocity at step k+1
130 Pkp1 = sol(N+2:2*N+2);
131 U_stark1 = sol(2*N+3:end);
132
133 %Criterion to end the iterations once critical film thickness is
      reached
134 criterion = min(hkp1);
135
136  if criterion < 10^(-3)
137       break
138
139  end
140  hkm1=hk; hk=hkp1; Pkm1=Pk; Pk=Pkp1;      %Update film thickness and
       pressure at steps k-1 and k
```

```
141
142
143
144 %Save every k/freq solutions that give modulus of 2
145
146 if mod(k,freq)==2
147     k
148     min(hkp1)
149     t
150     hstore=[hstore hkp1];
151     Pstore=[Pstore Pkp1];
152     tstore = [tstore t];
153     Ustore = [Ustore U_stark1];
154 end
155
156 end
157
158
159 toc
160 save('mobile_lambdav1')                    %Save file
161
162 %Step 8: plot the solutions
```

C Additional derivations

C.1 Equivalent radius

The equivalent radius is derived in the work of Abid & Chesters (1994). The pressure equation can be written for two particles of different size as:

$$P = \frac{2\sigma}{R_1} - \sigma\left(\frac{\partial^2 h_1}{\partial r^2} + \frac{1}{r}\frac{\partial h_1}{\partial r}\right) \tag{C.17}$$

and

$$P = \frac{2\sigma}{R_2} + \sigma\left(\frac{\partial^2 h_2}{\partial r^2} + \frac{1}{r}\frac{\partial h_2}{\partial r}\right). \tag{C.18}$$

Here, h_1 and h_2 are the positions of the interfaces. Notice that the excess pressure, P, is independent of the axial coordinate, z as can be observed in Eq. 111. Thus, the excess pressure in both Eq. C.17 and C.18 are the same, and the equations can be summed to give:

$$2P = 2\sigma\left(\frac{1}{R_1} + \frac{1}{R_2}\right) - \sigma\left(\frac{\partial^2}{\partial r^2}(h_1 - h_2) + \frac{1}{r}\frac{\partial}{\partial r}(h_1 - h_2)\right). \tag{C.19}$$

Dividing Eq. C.19 by 2 yields:

$$P = \sigma\left(\frac{1}{R_1} + \frac{1}{R_2}\right) - + \frac{\sigma}{2}\left(\frac{\partial^2}{\partial r^2}(h_1 - h_2) + \frac{1}{r}\frac{\partial}{\partial r}(h_1 - h_2)\right) \tag{C.20}$$

Hence, a single pressure equation can be used to describe both particles of different sizes, and the equivalent radius can be defined as:

$$\frac{1}{R_p} = \frac{1}{2}\left(\frac{1}{R_1} + \frac{1}{R_2}\right), \tag{C.21}$$

C.2 Gravitational term

To check the validity of neglecting the gravitation term in the equation of motion in Eq. 14, its magnitude is compared with the pressure term in the z-component of the equation of motion, which is the only remaining term in the dimensionless version of this equation as can be seen in Eq. 111. The pressure and gravitational terms is first written as:

$$\rho g_z = \frac{\partial P}{\partial z} \tag{C.22}$$

Inserting the derived characteristic pressure and thickness scales in Eq. 80 yields:

$$\rho g_z = \frac{\sigma}{\varepsilon^2 R_p^2}\frac{\partial \tilde{P}}{\partial \tilde{z}} \tag{C.23}$$

Then appropriate values for all the constants in Eq. C.23 are inserted. The surface tension value for air and water is chosen together with density for water and a particle size of 10^{-3}. In addition, the gravitational acceleration is inserted and and ε is decided to equal 0.1. This results in:

$$1\text{kg/m}^3 9.81\text{m/s}^2 = \frac{7.2\cdot 10^{-2}\text{kgm/s}^2}{0.1^2(10^{-3}\text{m})^2}\frac{\partial \tilde{P}}{\partial \tilde{z}}, \tag{C.24}$$

which simplifies to:

$$9.81\text{kg/m}^2\text{s}^2 = 7.2\cdot 10^6 \frac{\partial \tilde{P}}{\partial \tilde{z}}. \tag{C.25}$$

Thus, it can be concluded that compared to the pressure term, the gravitational term is negligible.

C.3 Derivation of the curvature term, 2H

The curvature is defined as:

$$2H = -\nabla \cdot \mathbf{n} \tag{C.26}$$

Inserting the nabla operator given in Eq. A.8 and the normal vector in Eq. 46 gives:

$$2H = -\left(\mathbf{e}_r\frac{\partial}{\partial r} + \frac{1}{r}\mathbf{e}_\theta\frac{\partial}{\partial \theta} + \mathbf{e}_z\frac{\partial}{\partial z}\right)\cdot\left(\frac{\mathbf{e}_z - \frac{1}{2}\frac{\partial h}{\partial r}\mathbf{e}_r}{\sqrt{1+\frac{1}{4}\left(\frac{\partial h}{\partial r}\right)^2}}\right) \tag{C.27}$$

By utilizing the definition of derivatives and dot product between unit base vectors, Eq. C.27 can be simplified to:

$$2H = \frac{1}{2}\frac{\partial^2 h}{\partial r^2} + \frac{1}{2r}\frac{\partial h}{\partial r} \tag{C.28}$$

Furthermore, the product rule in reverse can be employed, which yields:

$$2H = \frac{1}{2r}\frac{\partial}{\partial r}\left(r\frac{\partial h}{\partial r}\right) \tag{C.29}$$

Maria Fanebust

Coalescence of fluid particles in non-Newtonian media

NTNU
Norwegian University of
Science and Technology